Fabrication of $NiBi_3$ nanostructures and studies of quantum transport in the resistive state of $NiBi_3$ nanowires

By

Laxmipriya Nanda

PHYS11201704003

National Institute of Science Education and Research, Bhubaneswar

A thesis submitted to the

Board of Studies in Physical Sciences

In partial fulfillment of requirements

for the Degree of

DOCTOR OF PHILOSOPHY

of

HOMI BHABHA NATIONAL INSTITUTE

December, 2023

Homi Bhaba National Institute

Recommendations of the Viva Voce Committee

As members of the Viva Voce Committee, we certify that we have read the dissertation prepared by **Laxmipriya Nanda** entitled **"Fabrication of $NiBi_3$ nanostructures and studies of quantum transport in the resistive state of $NiBi_3$ nanowires "** and recommend that it may be accepted as fulfilling the thesis requirement for the award of Degree of Doctor of Philosophy.

Chairman - Dr. Sanjay Swain	9/4/24
Guide / Convener - Dr. Kartik Senapati	09/04/2024
Examiner - Dr. Neeraj Khare	9/4/24
Member 1 - Dr. Pratap Ku Sahoo	09/04/2024
Member 2 - Dr. Satyaprakash Sahoo	09/04/2024

Final approval and acceptance of this thesis is contingent upon the candidate's submission of the final copies of the thesis to HBNI.
I/We hereby certify that I/we have read this thesis prepared under my/our direction and recommend that it may be accepted as fulfilling the thesis requirement.

Date : 9th March 2024

Place : NISER, Bhubaneswar

Signature

Guide: Dr. Kartikeswar Senapati

STATEMENT BY AUTHOR

This dissertation has been submitted in partial fulfillment of requirements for an advanced degree at Homi Bhabha National Institute (HBNI) and is deposited in the Library to be made available to borrowers under rules of the HBNI.

Brief quotations from this dissertation are allowable without special permission, provided that accurate acknowledgement of source is made. Requests for permission for extended quotation from or reproduction of this manuscript in whole or in part may be granted by the Competent Authority of HBNI when in his or her judgment the proposed use of the material is in the interests of scholarship. In all other instances, however, permission must be obtained from the author.

Laxmipriya Nanda

DECLARATION

I hereby declare that I am the sole author of this thesis in partial fulfillment of the requirements for a postgraduate degree from National Institute of Science Education and Research (NISER). I authorize NISER to lend this thesis to other institutions or individuals for the purpose of scholarly research.

Laxmipriya Nanda

List of Publications arising from the thesis

Journal

1. " Bismuth Phase Dependent Growth of Superconducting $NiBi_3$ Nanorods ", **Laxmipriya Nanda**, Bidyadhar Das, Subhashree Sahoo, Pratap K. Sahoo, Kartik Senapati, Journal of Alloys and Compounds, **2023**, 960, 170948.

2. " Fabrication of Ni-$NiBi_3$ ferromagnet-superconductor nanoparticles ",**Laxmipriya Nanda**, Subhashree Sahoo, Pratap K. Sahoo, Kartik Senapati Journal of Nanoparticle Research, 25, 251 **2023**.

3. "Josephson coupling driven magnetoresistance in superconducting $NiBi_3$ nanowires", **Laxmipriya Nanda**, B. Das, S. Sahoo, P.K. Sahoo, K. Senapati, arXiv preprint, arXiv:2305.00958 (2023).

4. " Fabrication of planar nano Josephson junction using focused Ga-ion poisoning in $NiBi_3$ thin film " (Under Preparation)

Conferences

1. " Resistive states in narrow stripes of Superconductor-Ferromagnet bilayers " - **Laxmipriya Nanda**, Kartik Senapati, 'Quantum Matter Heterostructures', Toshali Sands, Puri, India, from 17-19, February 2020 (Poster presentation).

2. " Signature of coexistent Ferromagnetism and Superconductivity in Bi coated Ni nanoparticles " - **Laxmipriya Nanda**, Pratap K Sahoo, Kartik Senapati, 'Magnetism 2022', University of York, York, UK, from 28-29, March 2022 (Poster presentation).

3. " Quantum and Thermal phase slip in Superconducting $NiBi_3$ Nanowires: toward photon detection application " - **Laxmipriya Nanda**, Kartik Senapati, '66th DAE Solid State Physics Symposium', BIT Mesra, Ranchi, Jharkhand, India, from 18-22, December 2022 (ORAL and Poster Presentation).

Others

1. " Au-Implanted $TiSe_2$ Nanocrystals with Defect-Controlled Ferromagnetic Ordering: Implications for Spintronic Devices ", Utkalika P. Sahoo, Spandan Anupam, Bidyadhar Das, Mrinal K. Sikdar, **Laxmipriya Nanda**, and Pratap K. Sahoo, ACS Appl. Nano Mater., **2022**, 5, 4072-4081.

2. " Optimization of the superconducting properties of NbTiN thin films by variation of the N_2 partial pressure during sputter deposition ", Pratiksha Pratap, **Laxmipriya Nanda**, Kartik Senapati, R P Aloysius and Venugopal Achanta, Superconductor Science and Technology, **2023**, 36, 8.

List of Conferences and Workshops participated

1. " High Resolution TEM Methods", Pre-Conference Workshop EMSI 2018 Jointly organised by EMSI & NISER

2. " Fundamental Sciences and Quantum Technologies using Atomic systems(FSQT 2020)", jointly organised by Physical Research Laboratory(PRL), Gujarat and SciRox (Science club), Guru Nanak Dev University, Punjab & sponsored by TCG Centers for Research and Education in Science and Technology (TCG CREST), Kolkata, 28th September 2020- 1st October 2020.

3. " Technical Education Quality Improvement Programme - III " sponsored Webinar series on Recent Advances in Physics held on September 14-18, 2020.

Laxmipriya Nanda

ACKNOWLEDGEMENT

I extend my sincere gratitude to all those who have contributed to the completion of this Ph.D. thesis. This journey has been challenging, yet immensely rewarding, and I am deeply thankful for the support and guidance I have received along the way.

First and foremost, I express my heartfelt appreciation to my advisor, Dr. Kartik Senapati, for his unwavering support, invaluable mentorship, and continuous encouragement throughout this research endeavor. His expertise, constructive feedback, and commitment to academic excellence has been instrumental in shaping the outcome of this thesis.

I extend my thanks to the members of my doctoral committee, Dr. Sanjay Ku Swain, Dr. Ritwick Das, Dr. Pratap Ku. Sahoo, and Dr. Satyaprakash Sahoo, for their insightful feedback and valuable contributions to the refinement of this work. Their diverse perspectives and expertise have significantly enriched the quality of this research.

My heartfelt thanks go to the School of Physical Sciences and Centre of Interdisciplinary Science for providing a conducive research environment and access to resources that were essential for the successful completion of this thesis. I am also grateful to the Department of Atomic Energy (DAE) for their financial support, which enabled me to focus on my research without undue distractions.

I owe a debt of gratitude to my colleagues and fellow researchers from Superconductivity Lab and Ion Beam Nanomaterial Lab who shared their insights and engaged in stimulating discussions, enriching the overall research experience.

Special thanks to my family for their unwavering support and encouragement during this demanding journey. Their patience, understanding, and belief in my abilities have been a constant source of motivation.

ABSTRACT

A small quantity of magnetic impurity exerts a substantial influence on the suppression of superconducting order in the majority of superconducting materials. Contrary to this norm, a subset of superconducting materials, notably those incorporating robust ferromagnetic elements such as Fe, Ni, and Co, exhibit intriguing behavior. $NiBi_3$ serves as a noteworthy example within this category, manifesting superconductivity below 4.2 K while retaining distinct signatures of ferromagnetism. A distinctive characteristic of this compound is the spontaneous formation of an interface between Ni and Bi layers, a phenomenon observed even at room temperature. Despite ongoing debates in the literature regarding the coexistence of ferromagnetism and superconductivity in $NiBi_3$, its self-forming nature and remarkable resilience to the presence of significant Ni impurities render it a compelling system for study.

This thesis comprises two major components. The first section focuses on the fabrication of $NiBi_3$ nanostructures, including nanoparticles and nanorods. Exploiting the negative formation energy of $NiBi_3$," spontaneous formation occurs at the Ni/Bi interface, enabling the creation of isolated $NiBi_3$-coated Ni nanoparticles. The inherent spontaneity in the formation of $NiBi_3$ has also facilitated the production of superconducting nanorods comprising single-crystal $NiBi_3$ by optimizing the co-evaporation of Ni and Bi. In the second section, our attention shifts to magnetotransport studies conducted on $NiBi_3$ nanowires, which were lithographically patterned from co-evaporated $NiBi_3$ films. These measurements were conducted in the resistive state of the nanowires below the superconducting transition temperature. Our findings reveal that the concentration of Ni impurities significantly influences the phase slip behavior and inter-grain Josephson coupling of the nanowires, even down to widths of 70 nm. Notably, a high concentration of Ni in the inter-grain region induces periodic oscillations in magnetoresistance, likely attributable to the formation of quantization loops via random “zero” and “pi”- Josephson couplings at the granular level. Additionally, we demonstrate that irradiating 200 nm wide $NiBi_3$ nanowires with 5 kV Ga ions enables the realization of a macroscopic Josephson effect, even in the highly resistive state of the nanowires.

Contents

Summary

Currently, superconductor(S)-ferromagnet(F) hybrid systems represent a compelling area of research owing to their intricate interplay of physics, offering valuable insights and opportunities for exploration. Experimental evidence of oscillating order parameters and long-range spin triplet supercurrents within a ferromagnetic layer proximal to a superconductor exemplify ongoing research endeavors. Thin films of superconductor-ferromagnet hybrid structures, including bilayers and multilayers, as well as the fabrication of Josephson junctions, have been investigated within this S-F hybrid framework. In such direction we have chosen Ni-Bi system which is interesting to study due to the presence of a strong ferromagnet Ni in it as well as all the aspects of this Ni-Bi system is still under progress. The primary focus of this thesis is exploration of structural and physical properties within the nanoscale framework of the a very well known S-F binary alloy Ni-Bi system, where Ni is the intrinsic ferromagnetic components present in it. We have attempted to explore some of the physical properties in nanoscale geometry. Employing a comprehensive physical methodology, the synthesis of $NiBi_3$ nanowires and Ni-$NiBi_3$ nanoparticles was executed, with a dedicated investigation into their structural characteristics. These Ni-$NiBi_3$ nanoparticles show superconductivity around 3K as evidenced from magnetization measurement and the single crystalline $NiBi_3$ nanowire show superconductivity around 4.25K. We have also explored transport studies on $NiBi_3$ nanowires fabricated from thin $NiBi_3$ film to delve into the intricacies of phase slip and assess the impact of magnetic Ni impurities on magnetoresistance measurements. Furthermore, an examination of transport properties on Ga-implanted $NiBi_3$ nanowires (200nm) revealed distinctive Josephson junction characteristics as evidenced from standard magnetic field dependent voltage measurement.

List of Figures

Chapter 1

Introduction

1.1 Background

Superconductivity in binary metallic alloys have been traditionally interesting since the discovery of Superconductivity in Mercury by Kamerlingh Onnes [1]. A wide variety of binary alloys have been synthesized and studied since then, not only to find superconductors with enhanced critical parameters but also to understand the very phenomenon of superconductivity in multi-element systems. Superconducting binary systems consisting of elements with no apparent superconducting transitions down to very low temperatures are particularly interesting. This thesis deals with one such binary superconducting alloy, $NiBi_3$, which becomes superconducting below ~ 4.2 K. While one of the constituent (Ni) is a transition metal itinerant ferromagnet, the other constituent (Bi) is a semi metal. None of the two elements show superconducting properties down to milli Kelvin temperatures. Recently, however, pure Bi crystals have been shown [2] to superconduct below 0.5 K at ambient pressures, even though it has a very low carrier concentration, which precludes pair condensation as per the standard Bardeen-Cooper-Schrieffer (BCS) model [3]. On the other hand, many alloys of Bi are known [4, 5, 6, 7, 8] to superconduct at several Kelvin temperatures. More interestingly, all three transition metal ferromagnetic elements, Fe, Co, and Ni form superconducting alloys with Bi. While superconductivity in $NiBi_3$ at 4.2 K and in $CoBi_3$ at 0.4 K [9] have been demonstrated experimentally, theoretical calculations [10] suggest that $FeBi_2$ may also superconduct above 1 K at higher pressure. This group of three Bi alloys is particularly interesting due to the fact that superconductivity appears even in

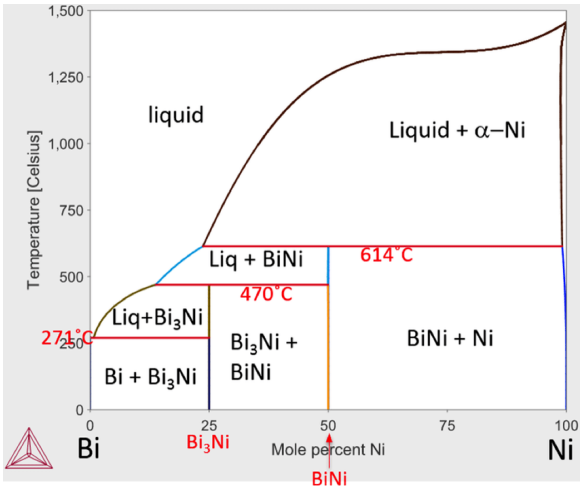

Figure 1.1: Phase diagram of Bismuth-Nickel binary system. Image adapted from Reference [11]

the presence of the strong ferromagnetic elements. Even though the superconducting transition temperatures are low in these compounds, there is plenty of scope for research in these materials from fundamental understanding of point of view as well as from the perspective of fabricating interesting hybrid superconductor-ferromagnet devices from thin films of $NiBi_3$. Among the superconducting, binary Bismuth alloys containing ferromagnetic elements, $NiBi_3$ has the highest transition temperature at ambient pressures and hence the most convenient system to study. In this chapter we introduce the $NiBi_3$ system and present a thorough literature survey on the earlier studies of physical properties of superconducting $NiBi_3$, especially in the thin film form. We then present the organization of the thesis.

1.2 Phase diagram of binary Bi-Ni system and the crystal structure of $NiBi_3$

The typical phase diagram of this Bi-Ni binary alloy is shown in the Figure 1.1 adapted from reference [11] . Bi has a melting point of $\sim$271 ^{o}C whereas Ni has a melting point close to 1700 ^{o}C. Therefore, a large fraction of the Ni-Bi phase diagram is in the liquid state.

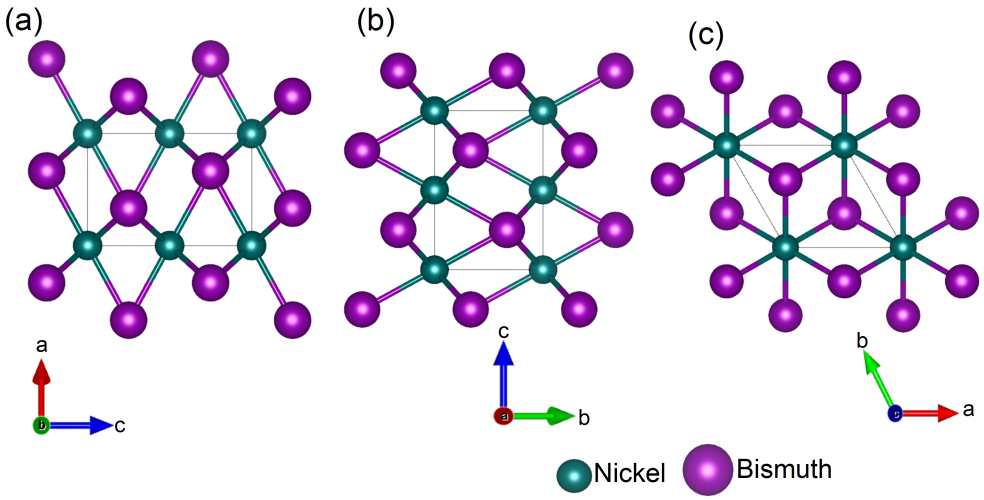

Figure 1.2: Hexagonal Crystal structure of binary compound NiBi. The arrangement of Nickel atoms are linear along the edges of unit cell. The 2D view of crystal structure in (a) ac-plane, (b) bc-plane and (c) ab-plane.

From this phase diagram, it is clear that Bi and Ni do not form a solid solution but gives rise to inter-metallic compounds NiBi and $NiBi_3$. Apart from the $NiBi_3$ phase, a NiBi phase also stabilizes at higher Ni concentrations and at relatively higher temperatures. The phase diagram also shows that $NiBi_3$ phase can coexist with Bi and NiBi phases at Ni concentrations of around 25 percent. This region of the phase diagram is particularly important in the context of growth of $NiBi_3$ thin films and at the interface between Bi-Ni bilayer films. During growth of thin films in the physical vapor deposition process, the effective temperature corresponding to the actual mobility of the elements arriving at the substrate surface may be well above the melting point of Bi. In such situations, considering the thin phase boundaries in the low Ni part of the phase diagram, a variety of phases may coexist including Bi, NiBi, $NiBi_3$ and Ni. This intermetallic alloys NiBi and $NiBi_3$ are known to be superconductors with similar transition temperatures of 4.1K and 4.2K,respectively [12, 13, 14, 15, 16]. Apart from superconductivity and magnetism, $NiBi_3$ has also been shown to exhibit thermoelectric properties [17]. Before we discuss superconductivity in $NiBi_3$, we discuss the

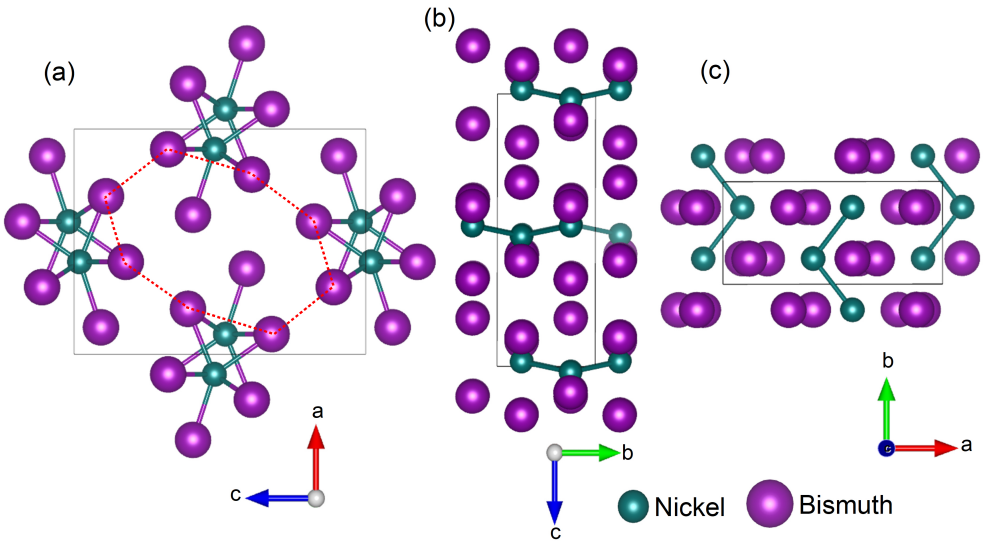

Figure 1.3: Orthorhombic Crystal structure of binary alloy compound $NiBi_3$. The arrangement of bismuth atoms give rise to octahedral structure RED dotted sides (inside the unit cell) in (a) view from ac-plane whereas arrangement of Nickel atoms are in zigzag chains along the b-axis as shown in (b) from bc-plane, (c) from ab-plane.

basic crystal structure of NiBi and $NiBi_3$ phases.

Figure 1.2 and 1.3 show the crystal structure of two Bi-Ni binary alloy compounds NiBi and $NiBi_3$, respectively. The crystal structure of NiBi is hexagonal with space group P63/mmc (194), point group 6/mmm and that of $NiBi_3$ is orthorhombic with space group Pnma(62), point group mmm. Figure 1.2(a), (b), (c) represent the 2D views of the NiBi crystal with arrangement of Ni and Bi atoms in the ac-plane, bc-plane, and ab-plane, respectively. It is clear that the arrangement of Ni atoms is along the sides or edges of the unit cell whereas the Bi atoms are located diagonal inside the unit cell. This is a symmetric crystal structure with lattice parameters a = b = 4.173 Å, c = 5.296 Å and $\alpha = \beta = 90.000°$, $\gamma = 120.000°$ [18]. Similarly Figure 1.3 represents the orthorhombic crystal structure of $NiBi_3$ where Fig 1.3(a), (b), and (c) show the 2D views of arrangement of Bi and Ni atoms in the ac-plane, bc-plane, and ab-plane, respectively. Figure 1.3(c) shows that Ni atoms are arranged in a zigzag linear chain along the b-axis with an angle of 108.71°. The inter-atomic

distance between Ni atoms in this chain is 2.53Å[13]. The highly anisotropic crystal structure leads to the anisotropic physical properties in the superconducting and normal state.

1.3 Superconductivity in Ni-Bi system

1.3.1 $NiBi_3$ single crystals

Generally the normal state variation of resistance R with temperature is expressed by the relation [19] :

$$R = R_0 + AT^n + C \exp\left(-T_0/T\right) \tag{1.1}$$

where exponential term arises from phonon-assisted scattering used to describe the resistance above 100K. The exponent n is related to the conduction-electron scattering mechanism. For the Ni-Bi system, the resistance curve is seen to be T^2 type which is a characteristic feature of electron-electron interaction [20, 21, 22]. However, Jayaram et al. [23] have shown that spin-density fluctuation can also explain the T^2 dependencies of resistance after including the s-d scattering effect. Although the mechanism of Cooper pairing is not very well established,$NiBi_3$ compound has been reported to show superconductivity below 4.2K, especially from electrical resistivity measurements [12, 13] and also through a tunnelling experiment by Dumoulin et al., [24]. Dumoulin et al. have reported that $NiBi_3$ is a strong coupling superconductor. The same authors also reported a high residual resistivity at low temperatures (below superconducting T_c) and saturation resistivity at high temperatures. In general, when the mean free path of electrons become comparable to the inter-atomic distance in any material scattering rate rises [25]. To explain the unusual behaviour of resistivity $\rho(T)$ at high temperatures, Ioffe and Regal [25] argued the short mean free path of electrons could be a possible reason. Later Fujimori et al. [13] investigated detailed physical properties such as electrical resistivity, specific heat, magnetic susceptibility, and superconducting properties including temperature and angle dependence of upper critical

field of $NiBi_3$. They also showed that the resistivity of needle-like crystal was 2 to 3 times smaller than that of polycrystalline samples at any particular temperatures. Here they have also evaluated the electron-phonon coupling parameter (λ_{e-p}) as 1.1 using the McMillan equation [26] and verified the $NiBi_3$ system to be strongly coupled superconductor, although $NiBi_3$ has a T_c of only 4.2K. PdTe is another such example of strongly coupled superconductor [27] with a relatively lower T_c of 4.5 K.

1.3.2 Multilayer Ni-Bi thin film systems

In the thin film form, $NiBi_3$ was first prepared using electron gun co-evaporation at room temperature [28]. The thin film samples were irradiated with the α particles and implanted with the Hydrogen atoms on which the resistivity measurements suggested that the superconducting T_c was unaffected by the local deformations in Bi_3Ni which reflects a shorter coherence length. Later on Siva et al. [29] have experimentally showed the spontaneous formation of phase $NiBi_3$ in bi-layer Ni/Bi thin films where thin films were prepared using sequential, in-situ thermal evaporation of high purity Ni and Bi. The multilayers were then mixed further using the high energy 100MeV Au ion implantation. Due to the low melting point of Bi (270°C) compared to the Nickel (1400°C), the diffusion of Bi into the Ni matrix gives rise to the $NiBi_3$ phase formation. The authors concluded this by performing angular dependence of glancing angle X-ray diffraction intensity, which effectively resulted in a depth profiling. Similar to earlier studies Siva et al. [29] also confirmed that the superconducting critical temperature of $NiBi_3$ remains unaltered by ion irradiation. However, the normal state resistivity shows some impact from varying ion fluences compared to the pristine sample, which is expected due to the formation of more defects with increasing ion fluences. Superconducting phases of Bi induced by deposition on a Ni sub-layer was studied by Moodera et al. [30], where they varied the thickness of Bi and Ni. In the case of thicker films they noted metallic characteristics of resistance from room temperature down

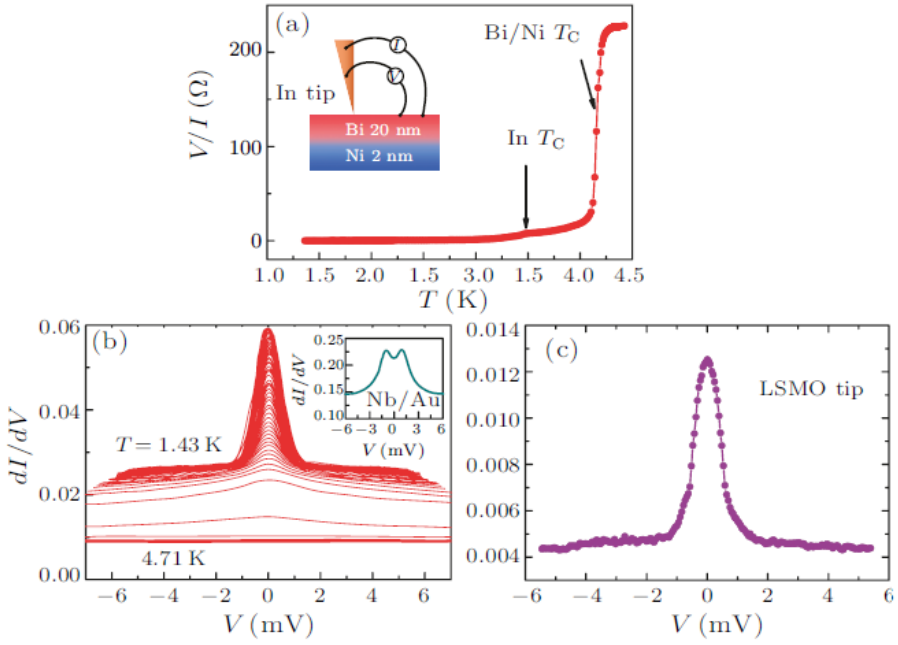

Figure 1.4: Possible p-wave superconductivity results for Ni/Bi sample[31]. (a) Inset: schematic of the measurement setup. Resistance vs temperature plot. (b) dI/dV at various temperatures for Bi/Ni sample. Inset: dI/dV vs V for Nb/Au sample. (c) dI/dV vs V for Bi/Ni sample using LSMO tip.

to 4.2 K, contrary to the thinner films, where the resistance remained unaffected by temperature variations. They also pointed out that Bi_3Ni or BiNi compounds possess a non-cubic crystal structure, whereas Ni/Bi films exhibit a cubic structure. This distinction led them to conclude that the formation of $NiBi_3$ or NiBi alloy is not evident in this system. Later on, however, several groups have confirmed the formation of $NiBi_3$ at the interface of Ni and Bi.

In another work on $NiBi_3$, Gong et al. [31] suggested a possible p-wave superconductivity in epitaxial Bi/Ni bilayer. For studying an extensive proximity effect, these authors fixed the thickness of Bi and varied the thickness of Ni from which it was confirmed that a small increase in Ni thickness substantially suppresses superconductivity. In the alternate scenario, wherein the thickness of Bi was increased while maintaining Ni at a constant

4nm, the revival of superconductivity occurred. To delve deeper into the pairing mechanism within the Bi/Ni bilayer, the authors employed a point contact technique using an indium tip. The critical temperature for the Bi/Ni bilayer was confirmed to be 4.1K, and the T_c for the Indium tip was determined as 3.5K from the double transition as shown in figure 1.4(a). Unexpectedly, the dI/dV curve of the Bi/Ni bilayer samples, when probed with both Au and LSMO tips, did not exhibit a double peak as observed in the 100nm Nb film(figure-1.4(b) and (c)). Gong et al. estimated a zero bias conductance of more than 2, indicating a potential signature of p-wave triplet pairing in the B/Ni bilayer system. Siva et al. [32] explored the superconducting proximity effect in the trilayer $NiBi_3$ - Ni- $NiBi_3$ thin film geometry. They emphasized that the proximity effect is significantly influenced by the S-F interface, and in the case of $NiBi_3$ - Ni, the interface is anticipated to be atomically sharp due to the self-diffusion of Bi into Ni. Another work by Siva et al. [33] presented evidence of enhanced surface and interface diffusion in Ni–Bi bilayers by swift heavy ion irradiation. The as-deposited bilayer Ni-Bi bilayer samples were irradiated with 100MeV Au ions in order to understand the Ion beam Mixing to form $NiBi_3$ alloy and subsequently ion induced surface modifications. From the Scanning electron microscope images, they found in increase in the size distribution of particles on the surface, which was attributed to ion beam induced local melting. The authors explained that the top layer of the thin film is a combination of $NiBi_3$ and partially elemental Bi. They emphasized that ion-induced athermal and ballistic effects drive Ni and Bi atoms toward the interface, thereby strengthening the reaction–diffusion mechanism and enhancing mixing in the irradiated films. Siva et al [34] also provided a comparable confirmation in their earlier results [33], by employing a series of 5 bilayers with varying thicknesses of Ni and Bi and irradiating with 100MeV Au ions. In the pristine sample, the X-ray diffraction peaks revealed the existence of two alloy phases, $NiBi_3$ and NiBi, attributed to the reaction-diffusion mechanism. A swift rise in mixing of Ni and Bi to form $NiBi_3$ was reported in this work, as a function of ion fluence.

Through the use of calculations based on the inelastic thermal spike model [35, 36], they ascribe the intensified mixing to the piling of thermal energy at the Ni-Bi interface due to difference in the thermal conductivity of the two layers. This is influenced by the stable phases present at the interfaces, the rapid temperature evolution induced by swift heavy ions, and the ballistic effects resulting from nuclear energy deposition.

Gong et al. [37] reported time-reversal symmetry breaking superconductivity in Bi/Ni bilayers using magneto-optical Kerr effect measurements. They showed that the superconducting critical temperature of the Bi/Ni bilayer exhibits a a non-monotonic dependence on the thickness of the Bi layer, with an initial increase followed by a drop. To circumvent the Kerr effect arising from the Ni underlayer, they used a Bi thickness of 20nm. The unique combination of robust spin-orbit coupling and non-centrosymmetry sets apart this 2D interfacial system from bulk TRSB superconductors [38]. The authors proposed that magnetic fluctuations in Ni trigger superconducting pairing in Bi in this case. The $NiBi_3$ system stands out as a unique case, as neither the rhombohedral Bi nor the face-centered cubic (fcc) Ni exhibits individual superconductivity down to very low temperatures. The onset of superconductivity in this system is thought to be possibly triggered by magnetic fluctuations at the interface, suggesting an unconventional nature of this material. In a study on the $NiBi_3$ system conducted by Wang et al. [39], the authors discussed this unconventional superconductivity extensively, presenting anomalous magnetic moments as evidence of chiral superconductivity in a Bi/Ni bilayer. If the superconductivity in the Bi/Ni bilayer is indeed unconventional, featuring chiral superconducting domains due to broken time-reversal symmetry (TRS) [37], an out-of-plane magnetic moments should develop at the edges. In the work of Wang et al. [39], a SQUID structure was engineered with one arm containing a Ni (2nm)/Bi (30nm) bilayer and the other arm formed by a superconducting Pb film measuring 50 nm in thickness and 1.4μm in width. The differential resistance, dV/dI_b, of the devices was measured as a function of bias current (I_b), revealing oscillation patterns

in two sweep cycles. Anomalous hysteretic behavior, unrelated to the ferromagnetism of the Bi/Ni bilayer, was observed in this scenario. This peculiar hysteresis was attributed to the motion of chiral superconducting domains within the bilayer.

In a report on Ni/Bi/Ni/Bi multilayers, Bhatia et al. [40] showed a gradual diffusion of Bi into the Ni to form $NiBi_3$. The magnetoresistance (MR) assessment performed on a 50μm wide track of these multilayer samples exhibited hysteric behavior at temperatures below 100K. This phenomenon was attributed to the existence of nanoscale Ni particle in the sample. Isothermal magnetization measurements revealed a declining pattern in saturation magnetization and a decrease in coercive field with an increase in the volume of $NiBi_3$. This observation provided additional confirmation of the existence of Ni as atomic or nanoscale impurities within $NiBi_3$. Magnetic force microscopy revealed a subtle magnetic contrast uniformly distributed across the samples, suggesting the absence of Ni clustering. Interestingly, images from the magnetic force microscope exhibited the emergence of Turing-like self organized patterns over time, which is a signature of the reaction diffusion process. Liu et al. [41] reported superconductivity in pulsed laser deposited Bi/Ni bilayer thin films consistent with other groups. In fact, a two step transition was reported by the authors which they atributed to the NiBi and $NiBi_3$ phases in the sample. High-Resolution Transmission Electron Microscopy (HRTEM) images and Convergent Beam Electron Diffraction (CBED) patterns of the cross-sectional samples showed that the Ni atoms deposited onto the Bi film react with Bi, giving rise to $NiBi_3$ and NiBi phases. The variation of T_c with an external magnetic field, in this report, indicated that the high-temperature (corresponds to one phase of Ni/Bi bilayer) transition decreases at a slower rate than the low-temperature transition (corresponds to another phase of Ni/Bi bilayer). Notably, in contrast to the Bi/Ni systems explored in the literature, CBED patterns, in this work, revealed that NiBi forms near the Bi layer while $NiBi_3$ forms near the Ni layer. An interesting question is how does the ferromagnetic layer influence the superconductivity in Bi/Ni. Does the exchange in-

teraction or the stray field effect dominate the MR around T_c? Zhou et al. [42] reported a study on the Stray field effects and vortex controlled magnetoresistance in superconducting Bi/Ni bilayers. The authors argued that in the Bi/Ni bilayer samples, domain walls are formed during the switching of Ni magnetization. Consequently, the critical temperature was suppressed by the stray field emanating from these domain walls, which was inferred from the peak in magnetoresistance (MR) occurring around the switching field and within the superconducting transition temperature range. Chauhan et al. [43] used time-domain THz spectroscopy (TDTS) to systematically examine the temperature and magnetic field dependence of superconducting gap in $NiBi_3$. The temperature-dependent zero-field complex conductance exhibited a Drude-like feature in this work. Through an examination of the magnetic field response utilizing a pair-breaking parameter, Chauhan et al. [43] argued in favor of a potential p-wave-like characteristics of unconventional superconductivity in $NiBi_3$.

Chao et al. [44] theoretically established the superconductivity in Bi/Ni bilayer motivated by the published literature on possible p-wave superconductivity in $NiBi_3$ system [31]. They argued that the observed superconductivity in Bi/Ni bilayer system was possibly the conventional phonon-mediated type within the bulk of Bi thin films. By leveraging the strong spin-orbit coupling inherent in Bi and the effective doping resulting from alloy formation in the Bi/Ni bilayer, the study proposes the potential existence of proximity-induced time-reversal broken $p \pm ip$ superconductivity on the Bi surface, particularly away from the Bi/Ni interface. This $p \pm ip$ scenario aligns well with recent experimental observations [45, 37]. However, it is essential to consider alternative possibilities, including bulk p-wave superconductivity induced by nanostructured Bi_3Ni [46], multiple Andreev reflections, or a point contact in the diffusive regime. Shang et al. [47] also conducted theoretical calculations on Andreev spectroscopy in the triplet-superconductor state within the Bi/Ni bilayer system and found consistency with the experimental results of Zhao et al. [48] only

when a small s-wave component was incorporated. However, when the S-wave component was significant, the conductance deviated from the point-contact results [48]. He et al. [49] theoretically established the evidence of triplet superconductivity in Bi/Ni bilayers. Their theoretical endeavors complement experimental investigations of point contact Andreev reflection (PCAR) in Bi/Ni bilayers indicating a possible Anderson-Brinkman-Morel type [50, 51] triplet superconductivity.

Liu et al. [52] experimentally investigated the Magnetic properties of superconducting phases NiBi and $NiBi_3$ formed during pulsed laser deposition of Ni-Bi films. In a previous work [53], the same authors had reported a two-step resistive transition in the PLD grown bilayer Ni/Bi system attributed to the presence of NiBi and $NiBi_3$ phases. In the current study [52], they discussed the voltage-current (VI) characteristics for the Ni/Bi bilayer samples and observe a singular superconducting transition at low temperatures. The data at low temperatures did not exhibit a vortex glass transition, as typically observed in superconductor/ferromagnet nanocomposites, thereby eliminating the possibility that the transition is due to a granular system or spontaneous vortices induced by the magnetic layer in the sample. Doria et al. [54], experimentally showed the T_c dependence on film thickness of Ni/Bi systems. In this work the Ni/Bi bilayer system was fabricated through sputtering, where the deposition sequence involved Bi as the first layer followed by Ni as the second layer. This deposition scheme followed the patterns of Ni_3Bi_x (3 nm of Ni on x nm of Bi) and $NiyBi_6y$ (y nm of Ni on 6y nm of Bi). The experimentally observed critical superconducting temperatures closely matched with the bulk T_c of $NiBi_3$. In the Ni_3Bi_x series, T_c values consistently surpassed those of bulk $NiBi_3$ and exhibited weak variations with film thickness. Upon comparing the theoretical findings with the experimentally observed thickness dependence of T_c in the two sets of Ni/Bi thin-film systems,Doria et al. [54] proposed a shape resonances in the superconducting state of the Ni/Bi systems arising from the discrete transverse electronic modes and a reduced collision rate in the transverse direction.

Das et al. [55] conducted a study on the phase evolution in thermally annealed Ni/Bi multilayers using X-ray absorption spectroscopy. The X-ray Absorption Spectroscopy conducted at the Ni K-edge showed a blue shift of the Ni K-edge in the near-edge portion of the spectrum. They also showed from the near-edge spectrum that the NiBi phase resulting from the decomposition of the $NiBi_3$ phase remains relatively unchanged with annealing up to 500°C. In fact, in the thin films of Ni/Bi system, synthesized from Ni and Bi by spontaneous diffusion reaction, keeps evolving slowly until all the Ni and Bi are consumed in forming $NiBi_3$ or NiBi. Recently, Das et al. [56] fabricated uniform films of $NiBi_3$ using co-evaporation of Ni and Bi. The resulting thin films exhibited a grainy, flake-like surface morphology, which was almost independent of the evaporation rate of Bi. They also showed the presence of elemental Bi in the $NiBi_3$ films from XRD measurements. This is consistent with the phase diagram of $NiBi_3$ shown in the Fig 1.1 in chapter 1. An increase in the superconducting transition temperature was noted with a higher Bi deposition rate, and this is ascribed to the more facile formation of the $NiBi_3$ phase compared to a lower Bi deposition rate. The elevated coercive field observed for a lower Bi deposition rate was attributed to the coexistence of both $NiBi_3$ (soft ferromagnet) and Ni (hard ferromagnet). Conversely, the decrease in metallic Ni and the rise in $NiBi_3$ at a higher Bi deposition rate contribute to a reduction in the coercive field, rendering $NiBi_3$ a softer ferromagnet.

1.3.3 Co-existence of Superconductivity and ferromagnetism

Coexistence of superconductivity and ferromagnetism in $NiBi_3$ is a debatable topic. LeClair et al. [57], by employing spin polarized tunneling spectroscopy methods (SPT), along with magnetometry and transport assessments, claimed simultaneous presence of a superconducting energy gap and conduction electron spin polarization (P) in a specific range of Ni thicknesses within the Ni side of Ni/Bi bilayers. In such a case, a novel and unique system is $NiBi_3$ for studying the interplay of magnetic and superconducting ordering. The authors

also performed tunneling measurements on $Co/Al/Al_2O_3/Ni/Bi$ junctions where the superconducting energy gap was found to depend on the thickness of Ni layer. The extensive experimental studies on these junctions conclude that both ferromagnetism and superconductivity are established at the same location which is at the Ni interface. In a subsequent study, Pineiro et al., [58]) demonstrated the potential simultaneous presence of superconductivity and magnetism in $NiBi_3$ prepared through a solid-state preparation method. Their investigation involved magnetic measurements aimed at identifying these properties, with the susceptibility versus temperature revealing a superconducting critical temperature of approximately 4.05K. Below T_c, isothermal magnetization measurements exhibited superconducting behavior, and an anomalous curve emerged just above T_c, which they attributed to the existence of ferromagnetism. Additionally, their X-ray photoelectron spectroscopy (XPS) analysis indicated the absence of any nickel impurities in their samples, suggesting that the magnetic properties observed in the $NiBi_3$ alloy were not due to the presence of magnetic nickel. Consequently, they concluded that both superconducting and ferromagnetic properties coexisted in the $NiBi_3$ alloys. However, despite these findings, the explanation for the simultaneous presence of these properties in $NiBi_3$ remains a subject of ongoing debate due to the insufficient evidence provided by these observations. Herrmannsdorfer et al. [46] also claimed the co-existence of superconductivity and ferromagnetism in structure-induced single phase $NiBi_3$ nanostructures. Here the bulk Bi_3Ni powder samples showed a T_c around 4.06K, while the magnetization measurements at 5 K (above T_c) showed the presence of ferromagnetism. The authors attributed the magnetism to the reduced dimension of the crystallites which impacts the electronic band structure due to the enhanced surface area. Extensive magnetization measurements at a significantly low temperature of 1.8K, much below T_c were carried out by the authors. These measurements revealed alterations in the ferromagnetic hysteresis curve, displaying diamagnetic screening and a broadening effect in the curve. Furthermore, it was observed that the nanostructures of Bi_3Ni exhibited

a higher magnetic moment and saturation magnetic field, reaching up to 14T, in contrast to the microstructured Bi_3Ni, which showed a saturation magnetic field of 1T. Sarli et al. [59] have performed theoretical studies on the co-existence of ferromagnetism and superconductivity in the Ni-Bi binary alloy. Using an effective field theory model, they derived the temperature and magnetic field dependence of magnetization for individual components Ni, Bi1, and Bi2, as well as for the NiBi-binary alloy. This investigation revealed that these components underwent two types of phase transitions: one of first order and the other of second order. The theoretical calculations agreed with the experimental reports of the co-existence of superconductivity and ferromagnetism in the NiBi system [60, 61, 62]. There are some conflicting reports on the coexistence of superconductivity and ferromagnetism in the $NiBi_3$ system. Silva et al. [16] demonstrated the occurrence of superconductivity at 4 K on flux grown single crystals of $NiBi_3$. They indicated that the ferromagnetic properties arise from amorphous Ni impurities rather than from $NiBi_3$ itself, as noted in their study. Another investigation conducted by Kumar et al. [14] unveiled that the $NiBi_3$ phase exhibits a superconducting transition at 4.1 K, without any indication of ferromagnetism. The incongruent outcomes observed in studies of the $NiBi_3$ compound underscore the imperative for additional scrutiny. A more comprehensive investigation is warranted to definitively ascertain the presence or absence of coexistence phenomena in this compound.

1.4 Motivation behind the thesis

As evident for the above discussion, $NiBi_3$ is a curious intermetallic compound which encompasses both supercoductivity and ferromagnetism (at least in some form). Both these orderings are known to work against each other when looked at from the perspective of the superconducting Cooper pairs. Therefore, the system is a natural test bed for the study of inhomogeneous superconductivity [63, 64]. It has also been discussed that a variety of

parameters can affect the way $NiBi_3$ is formed in a physical vapour deposition method. Previously, significant research has been conducted in the bulk and in the thin films of of Ni-Bi binary system, including Ni/Bi multilayers and $NiBi_3$ single layers. Exploring the superconducting properties in the nanoscale geometry of this interesting material $NiBi_3$ is still an open avenue for investigation. As discussed earlier, fabricating a $NiBi_3$ thin film poses greater challenges compared to usual metallic thin film superconductor like Nb or Pb. This is particularly because of the fact that Ni and Bi has extremely different melting points, which makes it very sensitive to deposition parameters. For example, the films have been found to be extremely granular which may have a significant impact on the quantum transport in the superconducting state. Devices formed out of this granular superconducting material also containing certain degree of ferromagnetism, irrespective of the origin of ferromagnetsm, could show fluctuation dominated transport. Nanoscale confinement may enhance these effects significantly in the $NiBi_3$ material. Therefore, our primary motivation behind the thesis is to explore the potential of this material as a quantum material in the nanoscale form. In the following section, we discuss the work on Ni-Bi nanoscale systems, so far reported in the literature.

1.4.1 Nanostructured Ni-Bi system studied so far

While a significant number of reports exists in the literature on $NiBi_3$ in the bulk and thin film forms, reports on nanostructures are quite limited. Park et al. conducted a study on the synthesis and characterization of Bi nanorods and superconducting NiBi particles [65]. The nanostructured NiBi samples were crafted using the well-established hydrothermal process. The XRD patterns unveiled the distinctive Ni, Bi, and NiBi products formed post-synthesis. Examination of the TEM bright-field plan-view image revealed Bi nanorods with diameters around 50 nm, alongside nanoparticles ranging from 10 to 200 nm in diameter. In a low-magnification TEM image of NiBi, the presence of aggregates of polycrystalline particles

was observed. An HRTEM image of a large single crystalline particle of NiBi depicted its attachment to numerous small Ni nanoparticles. EDS measurements indicated an atomic ratio of Ni and Bi close to 1. The Fast Fourier Transform (FFT) diffraction pattern highlighted the presence of hexagonal BiNi. While the authors noted that NiBi particles exhibit superconductivity with a transition temperature (T_c) of 4.25 K, no experimental data supporting this claim was presented. Ould-Ely et al. [66] synthesized Nickel-Bismuth bimetallic nanoparticles and nanowires using a wet chemistry method. Transmission electron microscopy (TEM) revealed the presence of medium-sized nanoparticles with a diameter ranging from 8 to 10 nm, exhibiting almost hexagonal shape. Selected Area Diffraction Pattern demonstrated the crystalline nature of some nanoparticles. The Zero Field Cooled magnetization curve indicates a maximum corresponding to the blocking temperature (T_B) of 45 K, while the susceptibility in the field-cooled magnetization measurement shows a smooth increase with decreasing temperature. This is a typical characteristics of the super-paramagnetic behaviour of magnetic nanoparticle aggregates. This implies that the small NiBi nanoparticles synthesized by Ould-Ely et al. [66] were magnetic. Considering the size of 8-10 nm, these nanoparticles are expected to be almost single domain type. The observed weak in magnetization agrees with the reported formation of the alloy phase, as documented by Yoshida et al [67]. Following this, William et al. [68, 69] utilized electron beam-induced fragmentation (EBIF) to generate arrays of non-overlapping bimetallic Bi-Ni nanoparticles. The particle sizes observed ranged from 50 nm to several microns in diameter. SEM images depicted the Ni-Bi product as clusters of particles forming large, irregularly shaped aggregates or wire-like meshes, with most particles displaying features of both morphologies. Micrometer-sized Bi-Ni particles synthesized through hydrothermal methods serve as precursors for electron-beam-induced fragmentation events. These events resulted in the generation of micrometer-sized, reproducible arrays of nonoverlapping bimetallic nanoparticles with diverse compositions and sizes. They proposed that the parent particles, under

conditions that limit the dissipation of thermal energy and electrical charge, melt incongruently to produce a Ni-rich solid and a Bi-rich liquid. For an EBIF event to occur, a parent particle must be relatively large with a diameter of at least a few micrometers and have a dense consolidated morphology. Crystallization upon deposition may be so rapid as to preclude ordered line compound formation, resulting in a random or weakly correlated atomic distribution in the nanoparticles. Apart from the above reports on the nanostructures of $NiBi_3$ system, there are no such reports on individual $NiBi_3$ nanostructure from a nanoscale device perspective.

1.5 Organization of thesis

We have structured the thesis in two major parts. The first part, consisting of chapter-2 and chapter-3, is about the fabrication of nanostructures whereas the second part, consisting of chapter-4 and chapter-5, is about the quantum transport in the resistive state of $NiBi_3$ nanowires.

- Chapter 1 is an introduction to the basic concept of Bismuth compounds or alloys with general ideas of the phase diagram of the Ni-Bi alloy system. This chapter also includes the extensive literature survey on the Ni-Bi binary system in bulk, thin film, and nanostructures so far.

- Chapter 2 deals with the fabrication of $NiBi_3$ nanorods using physical vapour deposition technique. The growth of nanorods on thin films of $NiBi_3$ was scrutinized under various deposition conditions, and the ensuing samples were characterized employing X-ray diffraction, scanning electron microscopy, and transmission electron microscopy techniques. Additionally, we have confirmed superconductivity in an individual nano rod of $NiBi_3$.

- Chapter 3 is about the study of the fabrication of ferromagnet (Ni)-superconductor ($NiBi_3$) hybrid nanoparticles. Using thermal dewetting method, isolated Ni nanoparticles were prepared, on which a superconducting $NiBi_3$ sheath was grown. This was done by evaporating a thin layer of Bi on the Ni nanoparticles, which diffused into Ni to form $NiBi_3$, by self diffusion process. Transmission electron microscopy revealed the formation of a superconducting shell on the core ferromagnet nanoparticles. Magnetization measurements were performed to obtain the signatures of superconductivity in the aggregate of isolated nanoparticles.

- Chapter 4 consists of two parts. The initial part investigates superconducting phase slip in the resistive state of $NiBi_3$ nanowires, while the latter part delves into examining the impact of Ni impurity on magnetoresistance in superconducting nanowires. We describe the fabrication of the nanowires from thin films of $NiBi_3$ by using focused ion beam patterning technique and report electrical transport measurements. We have also reported some experiments on the photosensitivity of a nanowire meander pattern of $NiBi_3$.

- Chapter 5 presents our attempt to create a planar Josephson nano-junction device utilizing focused Ga-ion irradiation on $NiBi_3$ thin film. We verified Josephson coupling by using magnetic field dependence of critical voltage across the junction, which mimics the Fraunhofer pattern of critical current across the junction.

- Chapter 6 provides a concise summary of the thesis along with an outline of the prospective areas for future exploration in this materials and related devices.

Chapter 2

Study of congruent growth of nanorods on the thin $NiBi_3$ films

2.1 Introduction

The formation of the $NiBi_3$ compound at the interface of Ni and Bi, when prepared in thin film form at room temperature, has been documented in several studies [29, 32, 40, 34, 41, 52, 70, 71]. However, it's important to note that the $NiBi_3$ layer generated through this process is confined to the interface. There are few reports [56] on uniform thin $NiBi_3$ films. Within the category of intermetallic compounds containing ferromagnetic elements such as Ni, Co has been observed to exhibit superconductivity [41, 72, 73]. However, it is also recognized that the presence of even a small amount of ferromagnetic elements can potentially negate superconductivity. $NiBi_3$ stands out as an example of an intermetallic alloy compound that maintains its superconductivity in the presence of Ni. Various techniques have been employed by researchers to produce the bimetallic superconducting compound $NiBi_3$, aiming to investigate its multifaceted properties. The acknowledgment is widespread that $NiBi_3$ demonstrates a low formation energy, attributed to the high diffusivity of Ni and Bi. This characteristic leads to the formation of microstructures in thin films during deposition through physical processes. The robust reactivity of Ni and Bi not only facilitates $NiBi_3$ formation but also contributes to the generation of diverse surface textures and topographical features on thin films within specific parameter ranges. These parameters can be precisely controlled through the co-evaporation process. As a result, the primary focus of this chapter is to elucidate the substantial influence of these parameters on the growth of

microstructures.

In the field of microstructural evolution, very few pieces of literature in the $NiBi_3$ system were published, such as Park et al. [65], had studied the synthesis and characterization of Bi nanorods and superconducting NiBi particles [65] using completely chemical methods. In another literature by Herrmannsdorfer et al. [46], the coexistence of ferromagnetism and superconductivity has been established via magnetization resistivity measurements on single phase Bi_3Ni nanostructures. Despite this, the nanoscale system of $NiBi_3$ alloy compound is poorly understood. This chapter aims to study the growth of nanorods and nanowires under different deposition conditions. Although there are some reports on the microstructural growth by Liying Liu et al. [53], by altering the layers of deposition Ni/Bi or Bi/Ni where the density of these microstructures found to be higher in Ni/Bi compared to the other. Mtshali et al. [74] have also studied micro-structure evolution in bilayer Ni/Bi systems by varying the deposition rate and thermal annealing. They have ensured the structural transformation of the films from amorphous (as-deposited) to polycrystalline hexagonal β-NiBi crystal structure when annealed from 60 °C to 200 °C. A similar effect was observed in our study when Ni and Bi were co-deposited at elevated surface temperatures. However, in this instance, exceptionally long crystalline nanowires of $NiBi_3$ were detected on the surface of the $NiBi_3$ films. The growth of these crystalline nanowires was explained in the context of the well-known vapor-liquid-solid (VLS) method. It was further identified that the presence of Bi with a hexagonal primitive cell promotes such anisotropic vertical growth of $NiBi_3$ in the form of both polycrystalline and single-crystalline nanowires.

2.2 Experimental details

2.2.1 Thin film growth

In this study, we employed a co-evaporation technique to deposit a uniform thin film of $NiBi_3$. Commercially acquired silicon substrates measuring 10 mm by 5 mm were used for the thin film deposition process. Prior to loading into the deposition chamber, the silicon substrates underwent thorough cleaning with acetone and isopropyl alcohol (IPA). High-purity bismuth ingots (99.99%pure) and Ni wire (99.99% pure) served as the target materials for thermal evaporation and electron beam evaporation, respectively.

Maintaining a chamber pressure of 1×10^{-7} bar, we adjusted various parameters to investigate the morphology of the $NiBi_3$ thin film. These adjustments included varying the bismuth evaporation rate (0.2 Å/s, 0.4 Å/s, 0.8 Å/s) and the temperature of the substrate holder (150°C, 250°C). For the co-deposition process, the Ni filament was initially activated to achieve a stable deposition rate of 0.1 Å/s by setting the filament current to 1.11 Amp and HV power to 127 Watt. Noting that filament current and HV power might vary for a fixed deposition rate, these values were recorded, and the filament was subsequently switched off and allowed to cool.

Subsequently, the DC current to the thermal boat (Bi target) was turned on. The DC current (68.1 Amp) and voltage (1.934 volt) were adjusted to keep the rate consistent. The deposition rate was monitored in a quartz crystal monitor (QCM) attached near to the substrate holder. The co-evaporation was performed by switching on the Ni pot simultaneously with the DC current to the thermal boat containing Bismuth. For each Bi rate of the evaporation of Bi, the evaporation rate of Ni was constant during the co-evaporation process.

To observe the effect of substrate temperature on the morphology of thin films, another set of samples was prepared by varying the substrate temperature to 150°C and 250°C by keeping other parameters fixed. Figure-2.1 depicts the schematic representation of the co-

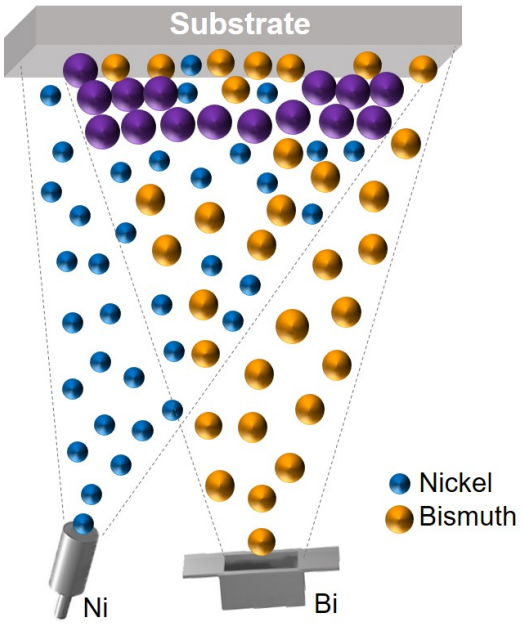

Figure 2.1: Schematic of the co-evaporation process for uniform $NiBi_3$ thin film deposition.

evaporation technique employed for thin film growth. In this process, Bismuth and Ni atoms reach the substrate randomly. However, the reaction between Ni (depicted as blue balls) and Bi (depicted as yellow balls) occurs in the atmosphere itself, specifically in the middle crossover region as shown in Figure-2.1, before reaching the substrate. Throughout the deposition process, $NiBi_3$ atoms reach the substrate and arrange randomly, as illustrated by the purple balls in Figure-2.1. Additionally, free Ni and Bi atoms also become incorporated into the thin film.

2.2.2 Characterization of thin $NiBi_3$ films using X-ray diffraction

The X-ray diffraction technique is used to study crystallographic structure of a material. When X-rays fall on the sample it gets diffracted by the atoms of crystal planes. The diffracted beam undergoes multiple interference and resultant intensity provides the information of crystal structure. The XRD works on the principle of Bragg's law:

$$n\lambda = 2d \sin\theta \tag{2.1}$$

Where n is the diffraction order, d is the inter-planar spacing and θ is the incident angle. The incident X-ray beams scattered from lattice planes separated by the distance d between the successive layers of atoms. XRD generally use conventional methods of θ - 2θ (Figure-2.2(a)) reflection geometry, which ensures a high intensity of beam diffracted from any particular set of crystalline planes of the sample. While scanning in this mode, the X-ray beam penetrates deeper into the sample (upto a few hundred micrometres). In this process, the signal from the surface or the few nm of the layer is become smaller as a very strong signal come from the substrate. In contrast, the Grazing incidence X-ray diffraction (GIXRD) (Figure-2.2(b)) technique uses a fixed small angle($< 1°$) of incident beam so that the diffraction can be made surface sensitive. Thus Grazing incidence configurations have been developed to overcome some limitations, e.g., to render the XRD measurement more sensitive to the near-surface region of the sample and minimize the substrate contribution to the diffraction response. Here the penetration depth is only up to orders of nanometers and the depth can be calculated using the following relation [29, 75]:

$$d = \sin\theta/\mu \tag{2.2}$$

where d is the depth of penetration, μ is the absorption coefficient, θ is the incidence angle.

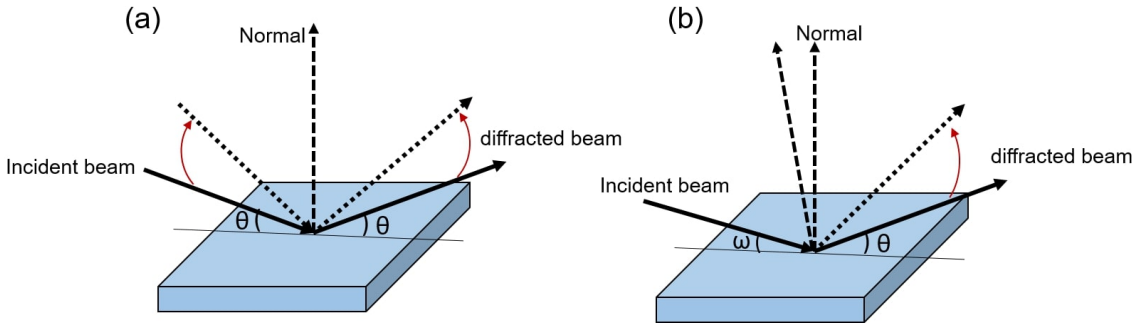

Figure 2.2: Schematic diagrams of (a) symmetric θ - 2θ and (b) asymmetric glancing angle XRD geometry.

In this thesis, we have used Bruker D8 advance diffractometer for the GIXRD measure-

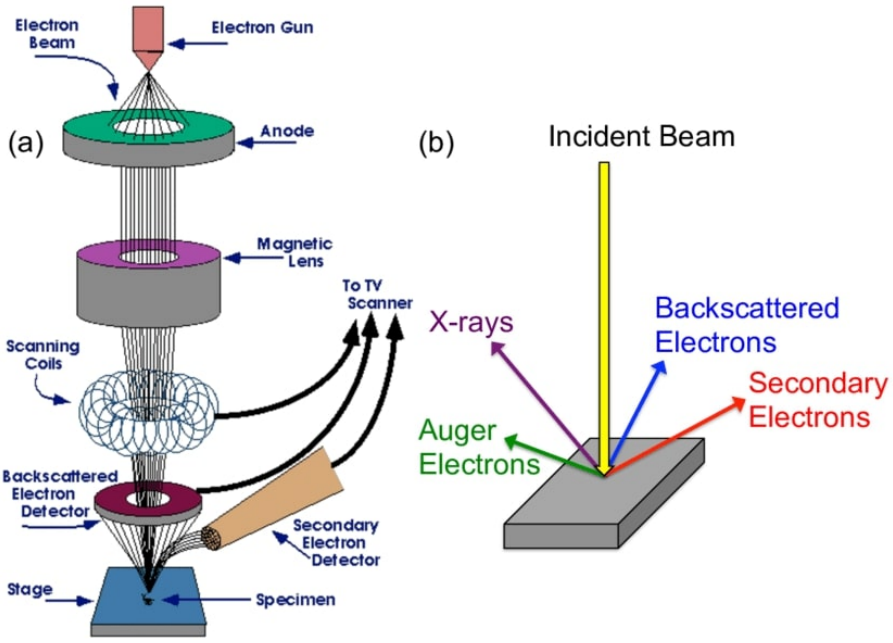

Figure 2.3: Schematic of FESEM adapted from Reference [76]. (a) Showing the different stages of passage of electron beam from the source to the specimen. (b) types of electron coming out of the specimen sample exposed to the electron beam.

ments for the detection of maximum number of $NiBi_3$ planes formed in the co-evaporation technique as the depth of diffusion varies of Ni and Bi varies in such process which will be discussed in our results section.

2.2.3 Morphological characterization using Field Emission Scanning electron Microscope (FESEM)

The term "field emission" is defined as follows: When a solid surface is subjected to a powerful electric field, the potential barrier containing the electrons within the solid diminishes, allowing the electrons to be released into a vacuum through the tunneling effect. In the field-emission electron gun (FEG), a single crystal of tungsten (W) serves as the cathode (emitter), featuring a tip with a curvature radius of approximately 100 nm. A robust electric field is created around the emitter tip, prompting the emission of electrons from the solid surface. Operating within an ultra-high vacuum of 10^{-8} Pa is essential to prevent tip con-

tamination from residual gases. This type of emitter, functioning at room temperature, is termed a cold-cathode emitter. The diameter of the virtual source is as small as 5 to 10 nm. Another characteristic of the Field Emission Gun (FEG) is the minimal energy spread (approximately 0.3 eV) of electrons emitted from the cathode. This energy spread is roughly one order of magnitude smaller than that of the thermionic-emission gun and approximately half the size of the Schottky-emission electron gun. Consequently, the FEG facilitates the capture of high-resolution images at a low accelerating voltage, particularly in situations where the chromatic-aberration effect of the objective lens becomes pronounced.

Figure-2.3 [76] shows the schematic of the working principle of FESEM. The upper parts are composed of different components such as electron gun, electromagnetic lenses, scanning coils etc. Electron beam passes through the electromagnetic lenses and converge into a specific spot size depending on the aperture size(30μm, 50μm, 120μm etc) and falls onto the specimen. The secondary electrons coming out of the sample typically gives the information of the surface morphology. The secondary detectors are also two types such as in-lens and secondary (SE). Out of which in-lens detector used for visualizing the depth of the surface morphology and SE detector is used for topological characterization only. As shown in Figure-2.3(b), the X-rays which coming out of the sample gives the information of elemental constituents of the respective sample. To stimulate the emission of characteristic X-rays from a specimen a beam of electrons or X-ray is focused into the sample being studied. While in a state of rest, an atom within the sample harbors ground-state (or unexcited) electrons situated in discrete energy levels or electron shells, bound to the nucleus. The incoming beam has the potential to excite an electron in an inner shell, causing it to be ejected from the shell and leaving behind an electron hole. Subsequently, an electron from an outer, higher-energy shell fills the void, and the energy difference between the higher-energy and lower-energy shells may be released in the form of an X-ray. An energy-dispersive spectrometer can then be employed to measure the number and energy

of the X-rays emitted from the specimen. In general, for standard imaging, the In-lens and SE detectors have been used. We have also used these two detectors for imaging on $NiBi_3$ films. Using energy dispersive X-ray spectroscopy (EDXS), material constituents inside the $NiBi_3$ samples were detected.

2.2.4 Imaging detection of crystalline nature of nanorods using Transmission Electron Microscope (TEM)

Electrons possess a shorter wavelength compared to light, with light having a longer wavelength. In a light microscope, improved resolution is associated with decreasing the wavelength of light. Conversely, in transmission electron microscopy (TEM), the resolution power increases as the wavelength of electron transmission increases.

In TEM, an electron source positioned at the top of the microscope emits highly energetic electrons (mostly 200 keV) that traverse a vacuum within the microscope column. Electromagnetic lenses are employed to concentrate these electrons into a thin beam, which is then directed through the specimen of interest. As the electrons pass through the specimen, they transmit. The transmitted electron beam then passes through different apertures (objective, Selected area) to reach the projector lenses from where the sample's signal has been detected using several detectors, as shown in the figure.

In traditional bright-field imaging, incident electrons scatter and disappear from the beam based on the compositional density and crystal orientation of the sample. The intensity of unscattered electrons generates a "shadow image" of the specimen, depicting different parts with varying darkness according to density. By rotating the sample and capturing multiple images at each rotation, a three-dimensional representation of the specimen (tomography) can also be constructed.

Figure-2.4 shows a schematic diagram of the transmission electron microscope system [77], where the top part is the electron source (cathode) typically made up of tungsten

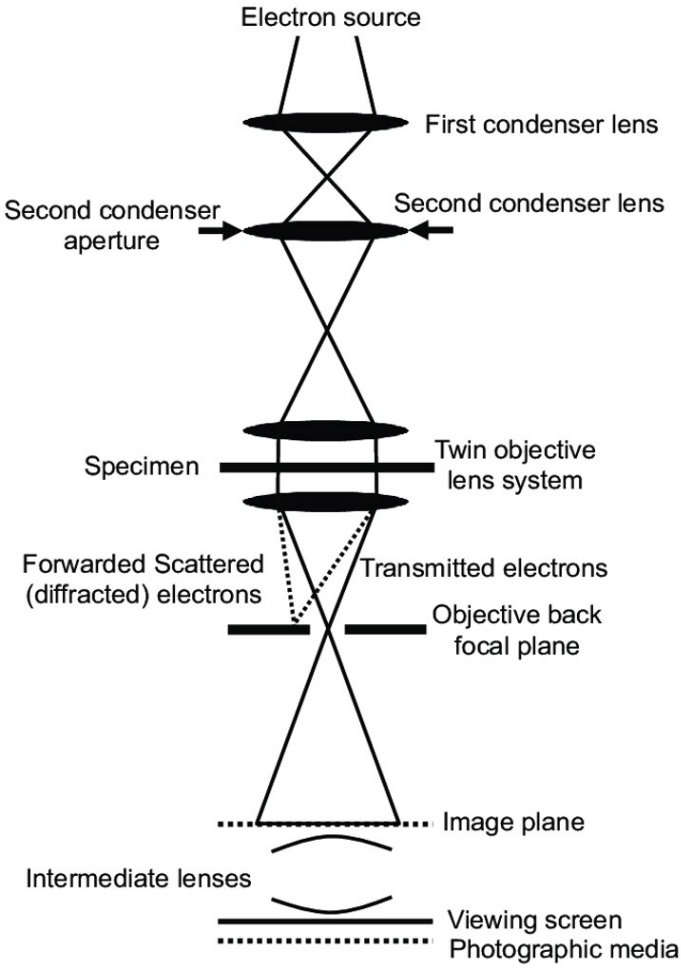

Figure 2.4: Schematic diagram of transmission electron microscope adapted from the reference [77].

filament or needle, or a Lanthanum hexaboride (LaB_6) single crystal source [78]. The negatively charged electrons attracted towards the anode and collimated further. In a TEM system, the flexibility to get the image down to atomic scale is possible because of lenses. These lenses are typically solenoids surrounded by ferromagnetic materials, which provide a magnetic field to the incoming beam of electrons. Following Fleming's left-hand rule, the path of the electron is spiralled inside these lenses, which helps to focus it to the desired size. Magnetic lenses play a crucial role in concentrating the electron beam onto the specimen. The condenser lens within the column tube aids in directing the electron beam into a vacuum, facilitating the creation of a sharp image. The vacuum environment prevents electron collisions with air molecules, ensuring a clear image without any deflection. A denser specimen results in increased electron scattering, forming a darker image on the screen as fewer electrons reach it for visualization. Conversely, thinner and more transparent specimens appear brighter in the image.

While reaching the sample, some X-rays also come out from the sample, which gives the information of elemental mapping of the same.

2.2.5 Lithography for single nanowire measurement

The single nanowire transport measurement follows several steps including photolithography, electron beam lithography, deposition of gold contact pads using DC sputtering. A flow chart is shown in Figure-2.5 describing the sequential steps.

2.2.5.1 Patterning of alignment marks using photo-lithography process

Photolithography is a well-known process that uses UV light for micro-size patterning on substrates. Here we have followed this lithography process to realize alignment marks on the substrate. Before the lithography process, the substrate was spin-coated with the positive photoresist with a rotation speed of 4000RPM for 30sec. The substrate with coated

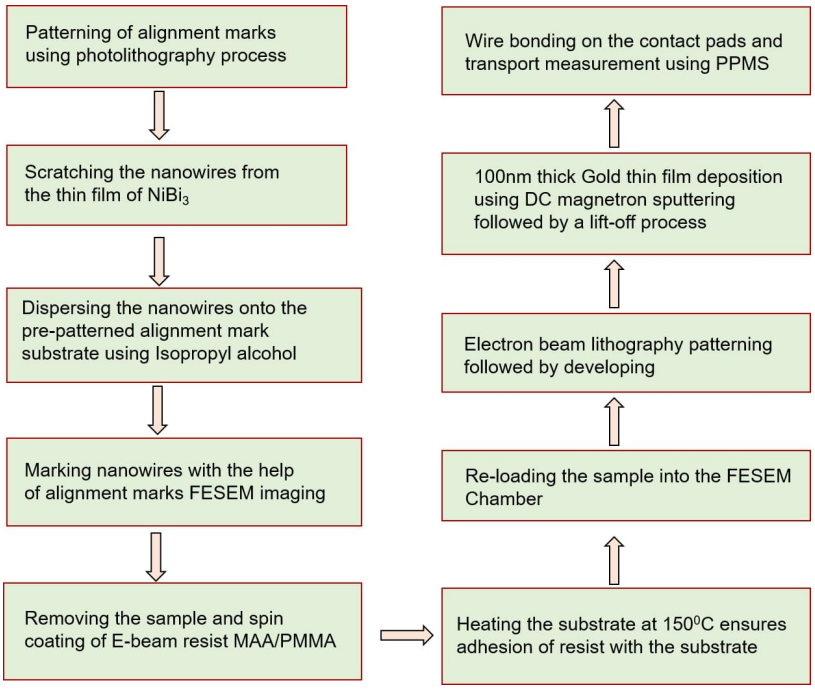

Figure 2.5: Flow chart for sequential steps followed for single nanowire measurement

photoresist was placed on the hot plate with a temperature of 75°C for 1min. In this spin coating process, the thickness of the photoresist stays within 1μm, which ensures the freedom for depositing a thin film within 400nm-600nm. A photomask was used with designed alignment mark patterns for UV exposure. Figure-2.6 (a)-(d) shows the schematic diagram of the photolithography process followed to get alignment marks on the substrate. Here photo-mask is designed in such a way that, the desired pattern is transparent through which the UV light penetrates and reach the photoresist. The chemical bonding of photoresist breaks under UV exposure which turns the resist to dissolve in the NaOH developer. Figure-2.6(e) shows the AutoCAD design of the alignment marks which we have used in the photolithography process. So in this process, we obtained the desired alignment mark pattern on photoresist coated alignment mark developed patterned substrate above which we have deposited 50nm thick Nb. After the thin film deposition, the sample was washed in acetone for lift-off to obtain the alignment marks on the substrate.

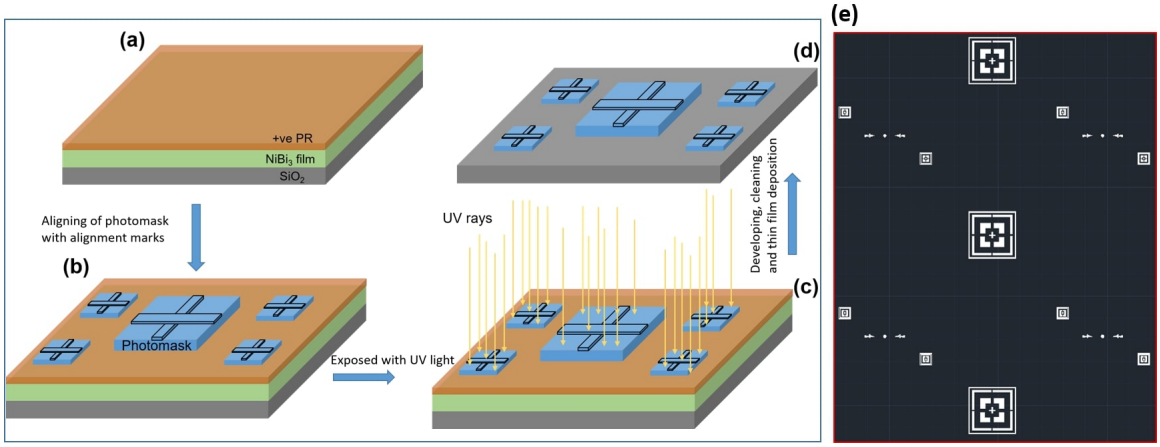

Figure 2.6: (a)-(d) A schematic of UV lithography process using a positive photoresist and negative photo mask of alignment marks. (e) The design of alignment mark pattern drawn using AutoCad software which is being used to expose on the Si/SiO_2 substrate.

2.2.5.2 Electron beam lithography patterning

Commonly referred to as e-beam lithography, this process involves using an electron beam to selectively remove either the exposed or non-exposed areas of a resist by immersing it in a solvent, thereby altering the resist's solubility. Similar to photolithography, the primary objective of electron beam lithography is to generate extremely small structures in the resist, which are subsequently transferred to the substrate material, often through etching. One significant advantage of this maskless lithography is its capability to create customized shapes (direct-write) with a resolution below 10 nm. Despite its high resolution, it is worth noting that this type of lithography comes with a trade-off of low throughput. In this process, the resolution of the pattern can be up to 100nm by choosing the correct dose of the electron beam. In our case, we have used Area dose 70μC/cm^2, beam current 0.181419nA. A lower electron beam dose ensures a controlled pattern area. The individual nanowires that developed on the thin $NiBi_3$ films underwent careful scratching using a surgical blade. Subsequently, isopropyl alcohol (IPA) was employed to transfer these nanowires from the thin film samples onto the substrate, which featured pre-patterned alignment marks. Utiliz-

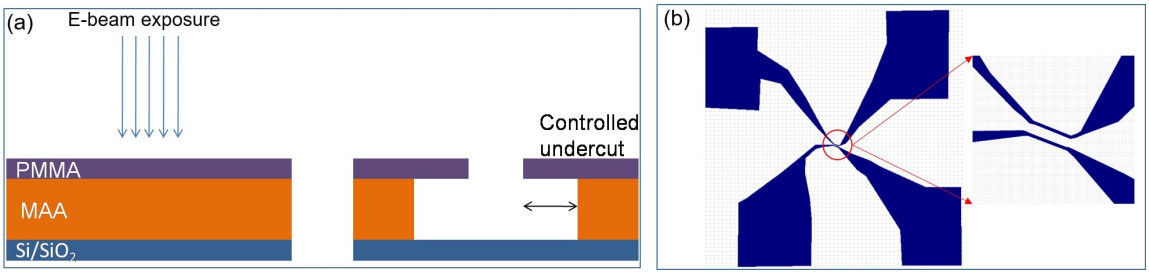

Figure 2.7: (a) A schematic process of undercut using bi-layer of Electron beam resists MAA/PMMA. (b) Design of the actual pattern drawn using RAITH software for Electron beam lithography.

ing the FESEM imaging, the wires were identified, and their positions were marked with respect to the alignment marks. After nanowire positions were delineated, the sample was removed from the FESEM chamber for the application of electron beam sensitive resist via spin coating. A bilayer resist comprising PMMA and MAA was employed, facilitating the formation of an undercut pattern, illustrated in Figure-2.7(a). Generally, MAA, as the initial layer, demonstrates heightened responsiveness to the electron beam in contrast to PMMA. This variance leads to a wider exposed region in the MAA layer than in the intended pattern. This disparity facilitates controlled undercutting by adjusting the electron beam exposure dosage accordingly.

The undercut serves as a valuable technique that enhances the efficiency of the liftoff process following thin film deposition. The design pattern, created using the RAITH software, is illustrated in Figure-2.7(b). We used this pattern to make electrical contacts to the single nanowire for transport measurement.

2.3 Results and discussion

2.3.1 Effect of evaporation rate of bismuth

2.3.1.1 FESEM images

Figure-2.8 shows the FESEM images of the 3 samples co-evaporated at 3 different rates of bismuth (a) 0.2Å/s (named Sample-A), (b) 0.4Å/s (named Sample-B), (c) 0.8Å/s (named Sample-C) respectively. These FESEM images were generated at the tilt angle of 54° from the surface of the sample. Here it is observed that, with increasing evaporation rate of bismuth the roughness of the sample surface is increasing which is consistent with the previous literature [53, 74]. In the Figure-2.8(c), a considerable number of outgrowth nanorods appeared of different size distributed randomly in the sample-C. The average length of these nanorods is around 1-2 μm which is apparent from the SEM images shown in fig-2.8(c). The nanorod like vertical growth may be due to the well-known vapour-liquid-solid (VLS) growth of nanowire growth in chemical vapour deposition [79, 80]. In the co-evaporation process, flux of Bi and Ni reaching the substrate are typically in the vapour phase. It is very well known that bismuth has a low melting point of $\sim$ 271°C, the Bi vapour approaching to the substrate at higher rate (0.8Å/s) must be very mobile which in turn implies that Bi reaching the surface mimicking the liquid phase of VLS process for making nanorods.

2.3.1.2 Glancing angle X-ray diffraction(GIXRD) measurements

Figure-2.9(a) shows the GIXRD plot for the samples deposited at various evaporation rate of Bi. From this XRD plot, it can be observed that plenty of $NiBi_3$ planes are present in all samples. The orange circle and the Blue triangle are notation for Bismuth peaks, Red rectangle box is notation for Ni and Grey star is the notation for $NiBi_3$ peaks. Out of all $NiBi_3$ peaks, the peak corresponds to (0 1 3) plane is strongest in all samples. Some of the $NiBi_3$ peaks corresponds to the hkl planes (1 1 2), (0 0 4), (2 1 2), (2 1 4), (0 2 0)

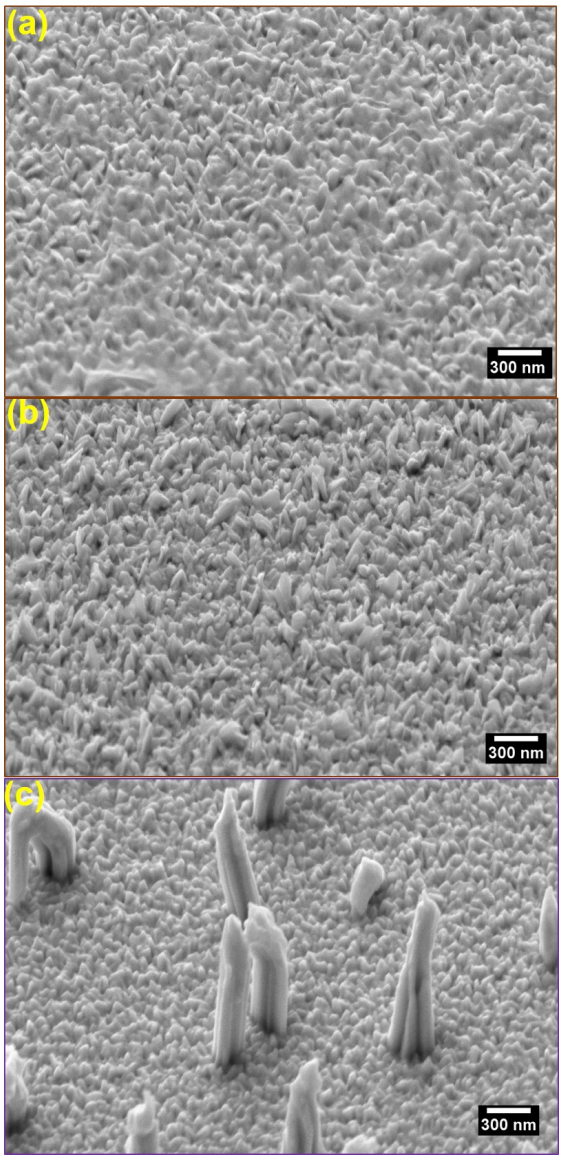

Figure 2.8: FESEM images of samples evaporated at various rate of Bismuth (a) 0.2Å/s (b) 0.4Å/s (c) 0.8Å/s.

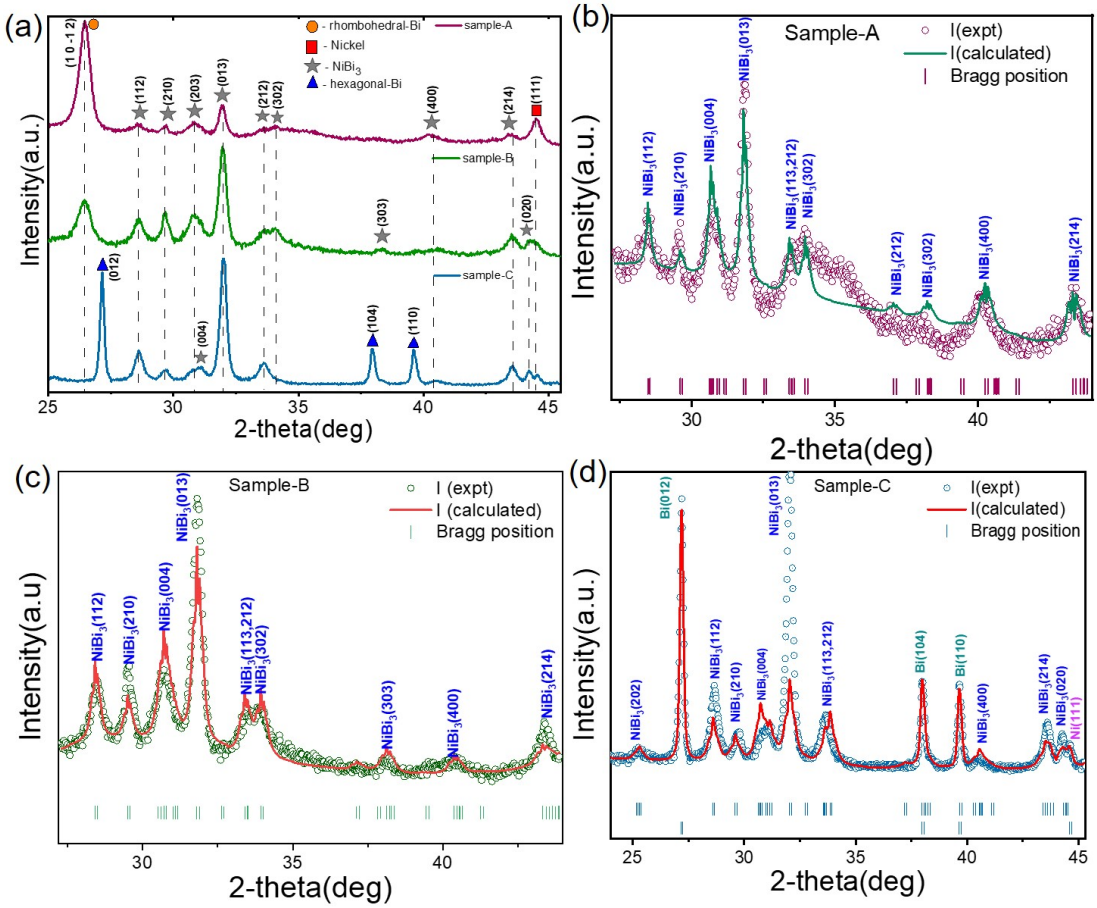

Figure 2.9: (a) X-ray diffraction plot of the corresponding samples deposited at various evaporation rate of Bi, Notation for different elements: Orange circle - rhombohedral-Bismuth, Blue triangle- hexagonal-Bi, Red rectangle - Ni, Grey star - $NiBi_3$. (b), (c) and (d) Rietveld Refinement fitting graph on the experimental plot for sample-A, sample-B, sample-C.

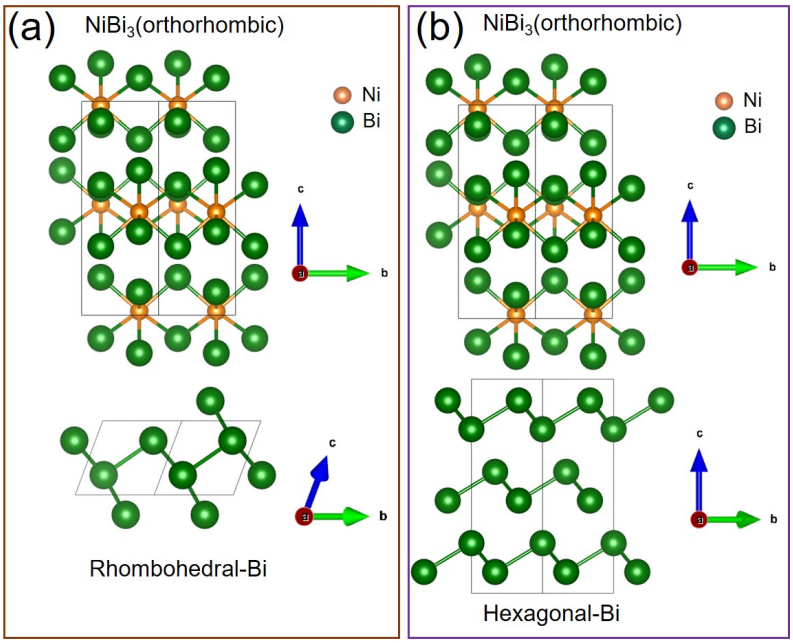

Figure 2.10: The comparison of 2D atomic representation of (a) $NiBi_3$ orthorhombic system (a=8.884 Å, b=4.15882 Å, c=11.485 Åand α=β=γ=90°) over the rhombohedral-Bi where lattice parameters are a=b=c=4.798 Å, α=β=γ=57.423°. (b) 2D atomic representation of $NiBi_3$ orthorhombic system over the hexagonal-Bi where lattice parameters are a=b=4.546 Å, c=11.862 Åand α=β=90°, γ=120°.

becomes prominent in sample-C and corresponding FWHM is also decreasing compared to other two samples. Another notable finding from this XRD plot is that, the $NiBi_3$ peak corresponding to the hkl plane (0 2 0) close to Ni peak (corresponding to hkl plane (1 1 1)) is decreasing with increasing rate of bismuth from 0.2Å/s to 0.8Å/s. Here it is also observed that with increasing rate of Bi from 0.2Å/s to 0.4Å/s, the relative strength all the $NiBi_3$ peaks increases while simultaneously the Bi peak decreases. This can be explained by the fact that more Bi is being used in the diffusion process and gives rise to $NiBi_3$. Interestingly, the Bismuth peak appears in the sample-A and sample-B corresponds to rhombohedral-Bi crystal system [81, 56] whereas in sample-C, the Bismuth peak corresponds to hexagonal-Bi crystal system with the space group R3m(166) (JCPDS file no:85-1329).

So here from XRD analysis, it is understood that the hexagonal-Bismuth may be pro-

moting the growth of nanorods as the nanorods are only appears in the sample-C. So now it is essential to realize the relation between the hexagonal crystal system with the growth of nanorods. The identification of the peaks in our GIXRD data, we presented in Fig-2.9(b),(c) and (d) the Rietveld structure refinement simulated using Full Proof software. It is common in the literature to report Rietveld refinements for powder diffraction data. However, since thin films (even polycrystalline thin films) always have some preferred orientations, the Rietveld refinement does not usually converge to a low value of Chi-sqr, especially due to the differences in the relative intensities compared to the powder diffraction data of the same material. As evident from the figures below, our fittings also showed the expected differences. However, the peak indices of $NiBi_3$ and Bi were possible to identify without ambiguity which we have used in Fig-2.9(b),(c) and (d).

To understand this, we have given an illustration of 2D crystal structure in the Figure-2.10(a) and (b). This 2D crystal structure modelling was done using the well known VESTA program [82]. The bottom Bismuth crystal structure is different for sample-A,B and C as seen in XRD. For sample-A and B, the crystal structure of Bismuth is rhombohedral-Bi with lattice parameter a=b=c=4.798Å, $\alpha=\beta=\gamma=57.423^{\circ}$ as shown in Figure-2.9(b) whereas for sample-C the crystal structure of Bismuth is hexagonal-Bi with lattice parameter a=b=4.546Å, c=11.862Åand $\alpha=\beta=90^{\circ},\gamma=120^{\circ}$ as shown in Figure-2.9(c). In both the cases the $NiBi_3$ crystal structure is Orthorhombic with lattice parameter a=8.884Å, b=4.15882Å,c=11.485Åand $\alpha=\beta=\gamma=90^{\circ}$. Looking at the lattice parameter values, it can been understood that there is a lower lattice mismatch between Bismuth hexagonal phase an $NiBi_3$ orthorhombic than the Bismuth trigonal. This lower lattice mismatch may promotes the growth of nanorods in case of sample-C whereas in sample-A,B the higher lattice mismatch may not become helpful to make any outgrowth nanorods.

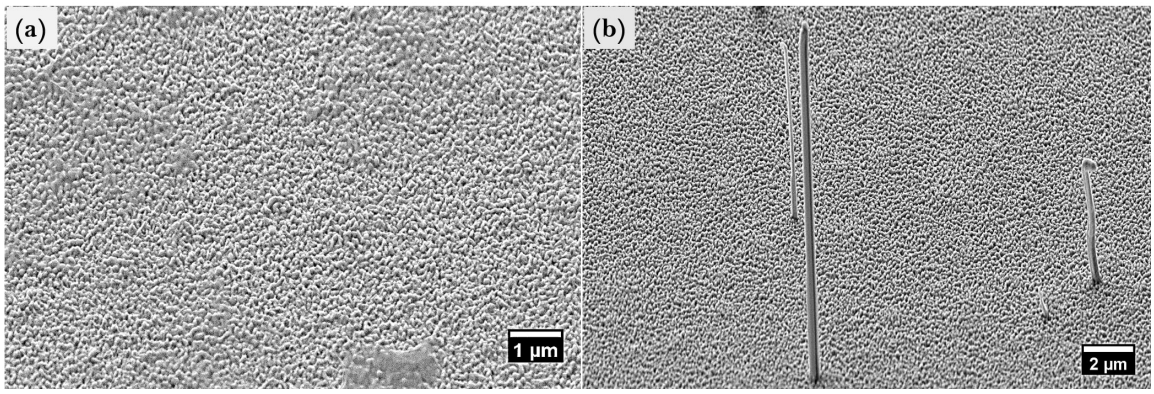

Figure 2.11: FESEM images of the sample deposited at different substrate temperatures (a) 150°C (b) 250°C. With increasing temperature, outgrown rods are found to appear significantly although in less density but higher in length than the earlier shown in Fig. 2.8(c).

2.3.2 Effect of substrate temperature

For further understanding of the growth of nanorods and nanowires, we have prepared another set of samples at different substrate temperatures 150°C (sample-D), 250°C (sample-E). Figure-2.11(a) and (b) show the FESEM images of 2 samples, D and E. In sample D, the roughness of the thin film is palpable, but no outgrowth nanorods. In contrast, in the case of sample-E, few nanowires appeared, which are longer than the earlier nanorods observed in sample-C. The length of nanowires is between 10 to 25μm, whereas the average width is around 300nm, which is an entirely new study on the $NiBi_3$ system as there are no reports on such long nanowires till now. Some reports on the temperature-dependent microstructural evolution in $NiBi_3$ system evidenced a few nm of the length of those rods [74]. But in such cases also Since the sample-E is deposited at 250°C which is close to the melting point of Bismuth (271°C), it is expected to be the activation of crystallization of $NiBi_3$ nanowires due to high thermal energy. Figure-2.11(a) represents the XRD plot for three samples deposited at different conditions such as ambient temperature, 150°C, 250°C. Here it can be observed that there are plenty of $NiBi_3$ peaks in all three samples. In the case of the sample deposited at ambient temperature, the $NiBi_3$ peaks corresponding to hkl values (1 1 2), (2 1

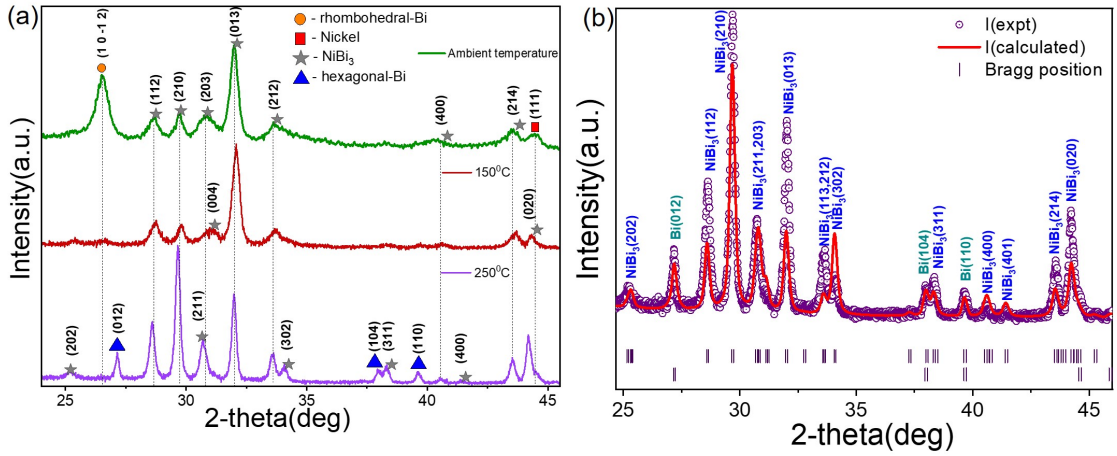

Figure 2.12: (a) GIXRD plot for the 2 samples deposited at 150°C and 250°C compared with the as-deposited sample. (b) Rietveld refinement graph with the experimental GIXRD plot for the sample deposited at 250°C.

0), (2 0 3), (2 1 4) are more comprehensive compared to the other two samples. The FWHM of the highest intense $NiBi_3$ peak corresponds to the hkl value (0 1 3) decreases with increasing substrate temperature 250°C. In the case of sample-E (deposited at 250°C), all the $NiBi_3$ peaks seem to have lower FWHM values leading to a re-crystallization process [83]. Other than this, in sample-E, the intensity of $NiBi_3$ peak corresponds to hkl value (2 1 0) is much higher than the (0 1 3) plane which is typically highest in the other two samples. This $NiBi_3$ plane (2 1 0) is the highest intensity peak according to the crystal structure database file. So in case of sample-E it is becoming apparent that the re-crystallization process enhanced the strength of $NiBi_3$ peaks. The GIXRD plot in fig-2.10(c) also shows that Bismuth peaks corresponds to sample-E is hexagonal symmetry whereas in other 2 samples rhombohedral symmetry axis. Similar to the previous section, we have observed the congruent growth of nanowires where underlying Bismuth corresponds to hexagonal axis symmetry. For further investigation, we presented a Rietveld refinement simulated plot over the experimental data for sample-E (deposited at 250°C) in Figure-2.12(b). Here the Refinement plot is showing a very good fit except the fact that intensity of some of the peaks of $NiBi_3$ correspond to

hkl plane (1 1 2), (0 1 3), (1 1 3), (3 0 2), (2 1 4), (0 1 2) are not exactly matching, but the positions are not shifting. The mismatch between the intensity of $NiBi_3$ peak and simulated refinement plot may be because of the reasons explained in previous section. But after re-crystallization process, the thin film become more crystallized than the films deposited at ambient temperature.

Hence in the latter sections, we will discuss regarding the elemental composition in these nanorods and nanowires.

2.3.3 FESEM and EDAX characterization of nanorods and nanowires

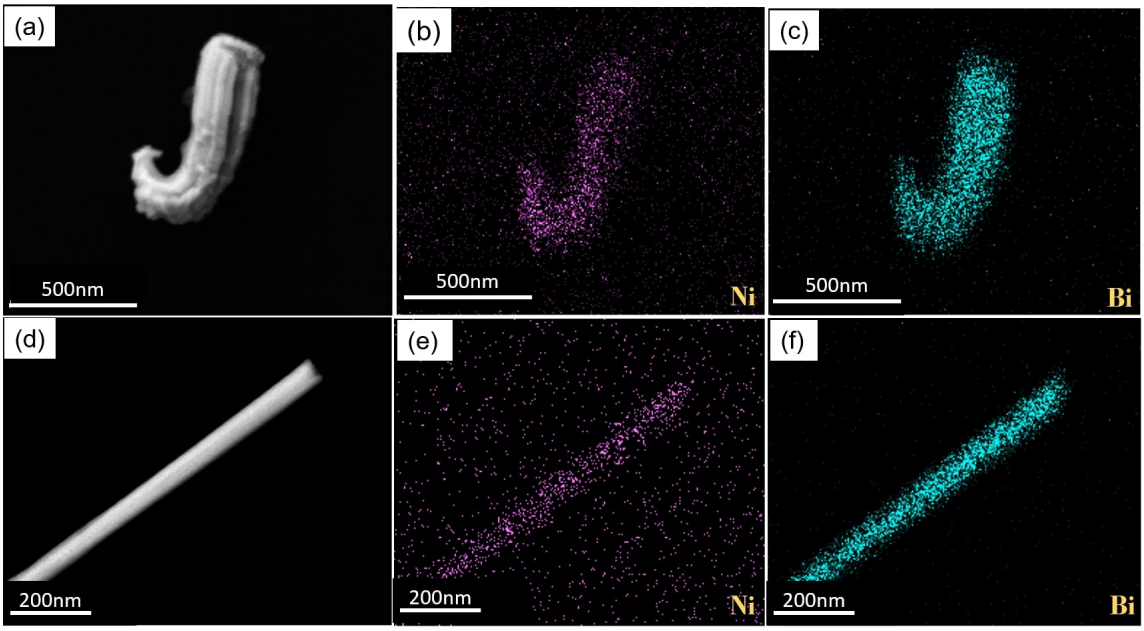

Figure 2.13: (a) FESEM image of single nanorod extracted from the thin film sample-C on the TEM grid, with corresponding elemental mapping of (b) Ni (c) Bi (d) FESEM image of single nanowire on the TEM grid, with corresponding elemental mapping of (e) Ni (f) Bi. Inset in (a) & (b) Elemental spectrum showing Ni, Bi and C, Cu, O from TEM grid.

Figure-2.13 shows the FESEM images and EDAX mapping of individual nanorods and nanowires extracted from the thin film and placed on TEM grids. Figure-2.13(a) shows the FESEM image of the nanorod formed on sample-C, here it can be seen that the nanorod is

clean and the clump-like appearance is clearly visible. Also the width (300nm) and length (1-2μm) of the nanorod is matching with the dimension mentioned above. The EDAX mapping of nanorod is shown in Fig-2.13(b) for Ni and Fig-2.13(c) for Bismuth. Similarly, Fig-2.13(d) is the SEM image of one of the nanowires formed on sample-E and corresponding EDAX mappings of Ni and Bi is shown in Fig-2.13(e),(f).

Here it is apparent that Ni and Bismuth is present throughout the nanorod and nanowire in a standard ratio of 1:3. Inset in both Figure-2.13(a) and (b) show the elemental spectrum for Ni, Bi as well as C, Cu, O from the TEM grid. For further characterization on the single nanorods and nanowires we have performed transmission electron microscopy measurement on these samples which is discussed below.

2.3.4 Transmission Electron Microscopy of nanorods and nanowires

To understand the crystalline behavior of these nanorods and nanowires, we have performed High-Resolution Transmission Electron Microscopy on the corresponding samples. Figure-2.14 shows the TEM image results with the 2D modeling for nanorods formed on sample-C. The polycrystalline nature of nanorods is observable in Figure-2.14(a). It is a zoomed region (Purple square box) of the portion of nanorod shown in the inset which is a comparatively thin part electrons could transmit easily. Here we have shown at right panel (b), (c), (d) 3 different $NiBi_3$ planes (2 1 0), (0 2 0), (1 1 2) marked in three coloured (Dark Blue, Dark Yellow, Light Green) square boxes in Fig-2.14(a). These three $NiBi_3$ planes are consistent with the 3 XRD peaks corresponding to 2-theta values 29.6°, 44.13°, 28.5° shown in Fig-2.9(d). The inter-planar spacing d values shown in the corresponding images match very well with the database JCPDS file no: 65-0088 and standard Cambridge Crystal structure database ICSD: 391336. For these 3 different $NiBi_3$ planes, we have shown a 2D representation of these at the right extreme panel (e), (f), (g). The modeling has been done using the well-known VESTA program [82]. The orthorhombic primitive cell's six unit cells are

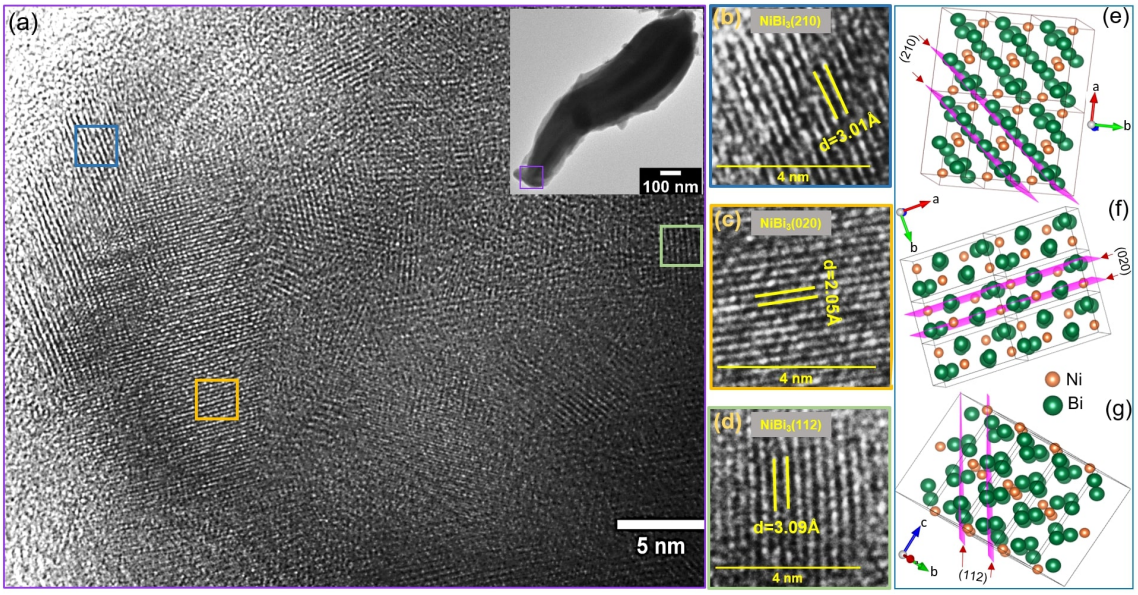

Figure 2.14: (a) HRTEM image of the selected area (square box in Inset) of nanorod formed in sample-C, Inset: shows the Bright field TEM image of the full nanorod. (b), (c), (d) are the high-resolution image of different $NiBi_3$ planes (2 1 0), (0 2 0), (1 1 2) which are the zoomed region of marked square boxes of (a). Right side panel is the $NiBi_3$ crystal structure showing atomic arrangements for respective planes in 2-D view (e) plane- (2 1 0), (f) plane- (0 2 0), (g) plane- (1 1 2).

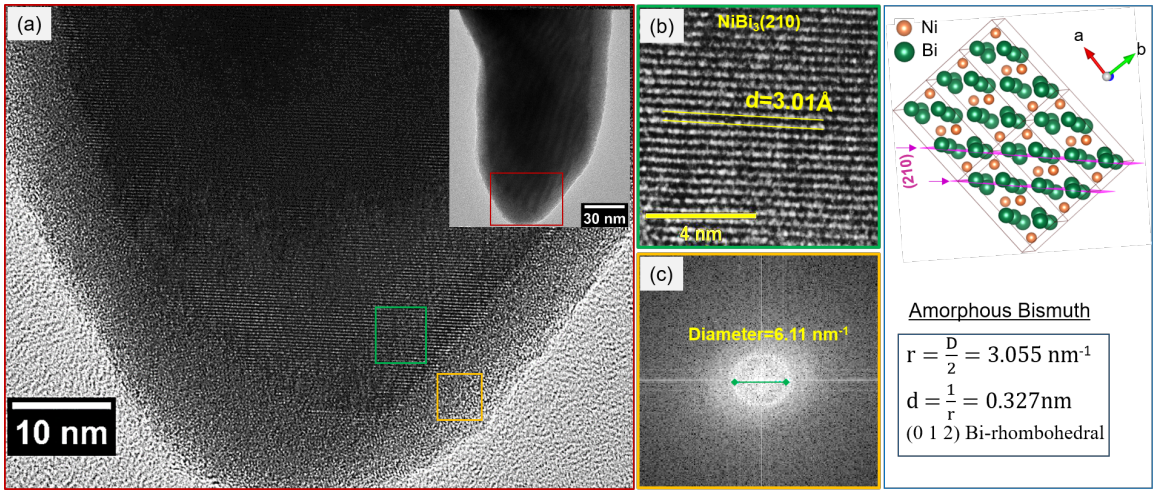

Figure 2.15: (a) HRTEM image of the selected area in Inset for the nanowire formed on the sample-E, Inset: Bright field image of the part of nanowire. (b) High resolution TEM of the zoomed region of Green marked square box in (a), showing the $NiBi_3$ single crystalline plane (2 1 0). (c) Fast Fourier Transform (FFT) of the Amorphous Bismuth for the selected region Dark Yellow square box in (a).

represented in the 2D modelling of the $NiBi_3$ crystal structure that is described here. Parallel Pink borders indicated here mimic the parallel planes in the HRTEM images displayed in (b), (c), and (d), where arrow marks indicate the crystal structure's orientation. From these HRTEM images, it is confirmed that the nanorods formed on sample-C is polycrystalline in nature with overlapping boundaries consists of different planes of $NiBi_3$ which is mimicking the polycrystalline behaviour of thin film as shown in XRD.

Figure-2.15 depicts the HRTEM results of another type of nanowire generated on sample E. The bright field TEM image of a portion of the nanowire is shown in the inset in Fig-2.15(a). Figure-2.15(a) depicts a zoomed part of the HRTEM picture (marked as a RED square box in the inset). The nanowire, in this case, is crystalline $NiBi_3$ (2 1 0) with an inter-planar spacing d value of 3.01Å. This $NiBi_3$ (2 1 0) plane agrees with the XRD peak, corresponding to the 2-theta value 29.623° as shown in Fig-2.13(b). Figure-2.15(b) shows a zoomed view of a comparatively smaller magnified region with a scale bar of 4nm which we have used to extract the d value using the Digital micrograph software. These nanowires

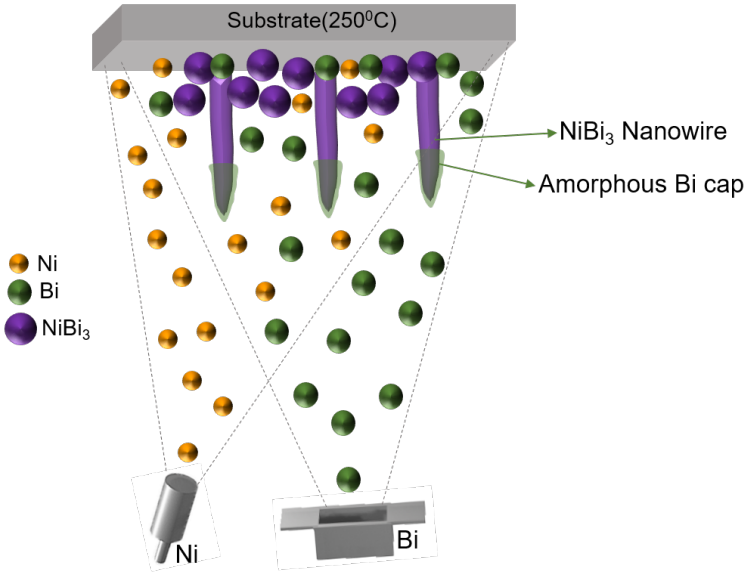

Figure 2.16: Schematic representation of the formation of $NiBi_3$ nanowires during the co-evaporation process at substrate heating temperature of 250°C corroborating the Vapour Liquid Solid (VLS) mechanism.

are formed on sample-E, and sample-E is co-deposited at a temperature of 250°C close to the melting point of Bismuth (271°C). It is very well known that deposition in the presence of temperature initiates the re-crystallization process [83]. Also, the GIXRD plot showed that the FWHM was increasing and the relative intensity of corresponding peaks enhanced. This behavior also scales in the TEM images of nanowires formed during the deposition, indicating the re-crystallization of nanowires. Other than the crystalline behavior of the nanowire, it is also observed that there is an amorphous capping layer at the tip of the nanowire. We have represented a Fast Fourier transform (FFT) of this amorphous region as marked by a yellow square box in Fig-2.15(c). This FFT indicates the unstructured behavior as a circular ring with a diameter (D) of 6.11nm^{-1}, which is matching with the d value of (0 1 2) plane of the hexagonal-Bi for which calculations are shown in the right panel. This amorphous Bismuth at the tip indicates a similarity in the nanowire formation in the well-known Vapour-Liquid-Solid (VLS) method. In this method, the molten metal nanoparticle

works as catalyst hosts the an-isotropic growth of nanowire [84, 85, 86, 87] in presence of chemical vapour at high temperatures. The amorphous Bi cap is very similar to the liquid phase as discussed in several literature [88, 89, 90, 91]. During the co-evaporation process, Ni and Bi interact in the vapor phase state to form $NiBi_3$ alloy. Other than this diffusion process, some extra Ni and Bi vapor also reach the heated substrate. As Bi has a low melting point, the Bi reaches the heated substrate becoming vapour which imitates the liquid phase. Further, Ni and $NiBi_3$ coming in contact with the apparent molten phase of Bi get catalyzed in the same manner as in VLS growth of nanowires in the presence of Au droplets [92, 93].

Figure-2.16 represents the schematic process of formation of $NiBi_3$ nanowires during the co-evaporation process at a substrate heating temperature of 250°C where the green capping tip at the nanowire mimics the amorphous Bismuth cap. In the standard VLS mechanism process, the molten metallic nanoparticle plays the liquid phase which is staying as the amorphous Bi cap here. We would like to highlight here that the average length of nanowires formed during this process is in between 10-25μm which is not yet reported in the literature.

2.3.5 Superconductivity in single crystalline $NiBi_3$ nanowire

As we have observed, the nanowires formed during the co-evaporation process at substrate heating temperature of 250°C are single crystalline and long enough (10-25μm), that the superconducting properties of these nanowires will be easily accessible in a single nanowire device fabrication process. For this purpose, we have fabricated single $NiBi_3$ nanowire devices using a standard electron beam lithography process. We have discussed the complete process of the Electron-beam lithography process in section 2.2.5. Here we have presented a schematic of our nanowire device in Fig-2.17(b). A standard four-probe geometry was used for the electrical contact measurement process denoted by I+, I-, V+, V-. The yellow contact pads are Au thin film deposited using DC magnetron sputtering whereas Blue

line corresponds to the $NiBi_3$ nanowire. A SEM image of the actual device is shown in fig-2.17(c) where it is apparent that the length of the nanowire is 12μm and the width is 350nm. Figure-2.17(a) shows the normalized resistance vs temperature measurement on a single Nanowire device compared with the $NiBi_3$ thin film deposited under the same condition. For both cases, the resistance has been normalized at 4.75K. Here it is evident that the $NiBi_3$ thin film has a sharp superconducting transition of 4.4K with a transition width of 0.05K whereas $NiBi_3$ nanowire shows a sharp superconducting transition around 4.3K with a transition width of 0.1K. It is also observable that the resistance of $NiBi_3$ nanowire does not go to zero value which is understood as a standard phase slip phenomena [94]. This phase slip phenomenon is very well-known in superconducting nanowires. This causes the superconducting order parameter to fluctuate and the associated phase of these order parameters to shift at any given position along the nanowire by a multiple of 2π. The average effect of multiple random phase slip events at random locations transforms those locations into normal regions, which ultimately increases the amount of resistance in presence of a bias current [94, 95].

2.3.6 An attempt for electron beam annealing-assisted growth of nanowires

In a separate experiment on the thin $NiBi_3$ film, we have performed electron-beam annealing process to visualize the growth of nanowires. The discussions in the previous sections suggest that the formation of single crystalline $NiBi_3$ nanorods is promoted by two essential conditions, viz. (i) the presence of hexagonal Bi phase in the $NiBi_3$ film and (ii) higher temperature of growth close to the melting point of Bi. In order to further verify this observation, we have performed a local annealing experiment on the series of co-evaporated films grown at ambient temperature (Samples A, B, and C).

In the sample-C we observed the appearance of a bubble in the initial phases (Fig-2.18(a) which expanded with increasing time of irradiation. After about 2 minutes of irradiation

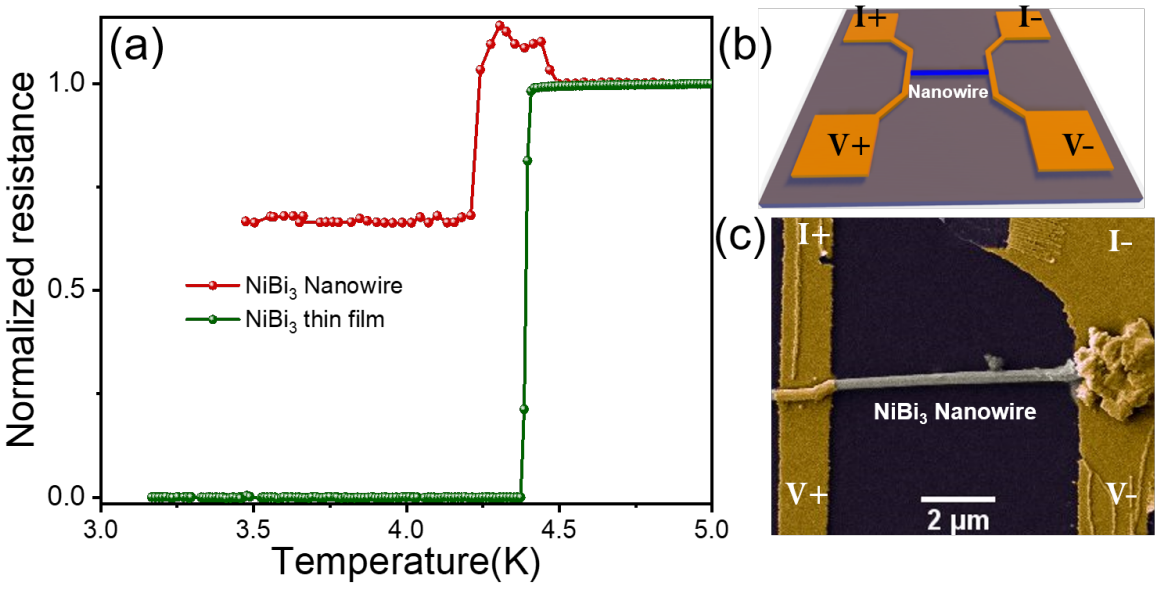

Figure 2.17: (a) Resistance (R) vs Temperature (T) plot for the $NiBi_3$ nanowire compared with the thin film of same sample-E. (b) Schematic of the geometry for the pattern use for contact to a single nanowire. (c) SEM image of the respective $NiBi_3$ nanowire after EBL patterning and gold thin film deposition.

the expansion of the bubble saturated (shown in Inset of Fig-2.18(a)) and a $NiBi_3$ nanowire started to grow on the bubble. The energy deposition from the incident electrons is expressed by the relation [96, 97];

$$E = E_{\max} \sin^2(\theta/2)$$
$$E_{\max} = E_0 \left(1.02 + E_0/10^6\right) /(465.7A) \tag{2.3}$$

Where E_0 is the energy of incident electron in eV and A is the atomic number of the impacted nucleus. According to Kolosov (2018), [98] similar re-crystallization of bismuth thin films has been reported utilizing an electron beam in a transmission electron microscope with two applied voltages, such as 5 kV and 200 kV. Due to bismuth's low melting point, researchers found several clear microstructures. In the present scenario, the co-evaporated sample contains a large quantity of bismuth, as indicated by XRD, which may result in the formation of microstructures when the incident high-energy electrons collide.

In Fig 2.19, We have shown that the Sample-A and Sample-B have excess Bi in the film

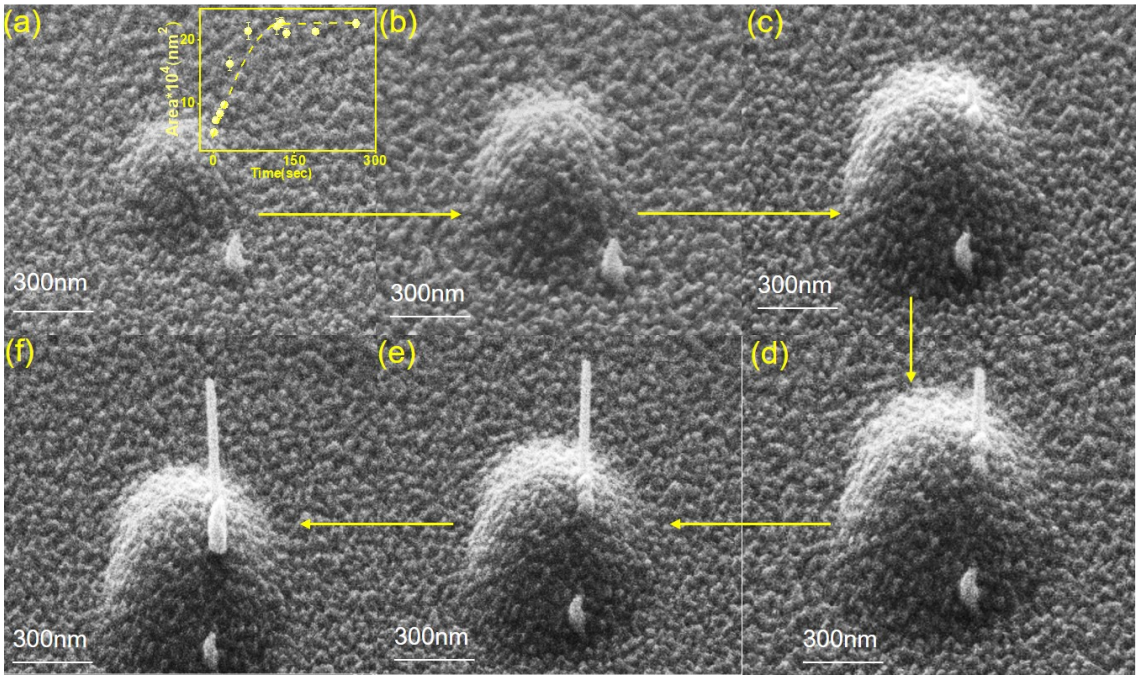

Figure 2.18: Electron-beam assisted growth of nanowires on sample-C. (a) A bubble type feature is appearing on the surface. (b)-(d) Increase in the area of bubble region, (c) A small nanorod growing on the bubble of the surface, length of which is increasing in the vertical direction(d)-(f).

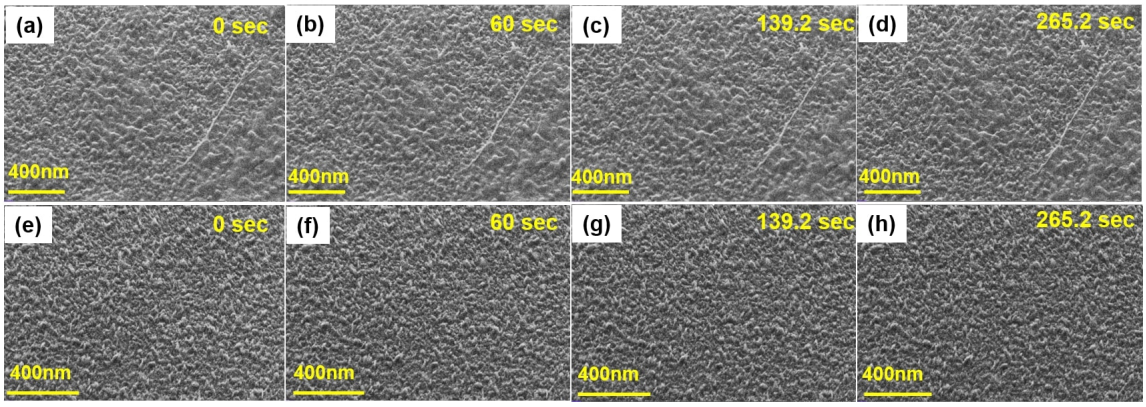

Figure 2.19: Real-time FESEM images of sample-A(top 4 pictures) and sample-B (bottom 4 pictures) with exposing 20keV electron beam. There is absolutely no change in the surface morphology.

in the rhombohedral axis symmetry form, while Sample-C has excess Bi in the hexagonal axis symmetry. We used a FESEM system to irradiate a small area ($\sim$ 1 μm^2) on the films with a 20 keV electron beam, while simultaneously imaging the same area. In samples A (Figure-2.16(a)-(d)) and B (Figure-2.16(e)-(h)) we observed no change on the surface with increasing time of irradiation.

If only the excess bismuth just below the surface is triggering the growth of nanorods, then in sample-A and sample-B, there was no such appearance observed. This indicates the growth of nanorods using an electron beam is also phase-dependent on bismuth as in the case of sample-C, the bismuth is hexagonal axis symmetry.

2.4 Summary

In this chapter, we have discussed the congruent growth of $NiBi_3$ nanorods and nanowires on $NiBi_3$ film by varying several parameters, such as the evaporation rate of Bismuth (0.2Å/s, 0.4Å/s, 0.8Å/s) and substrate temperature (150°C, 250°C) during co-evaporation of Ni and Bismuth. FESEM images confirmed the presence of nanorods with an average length of 1-2μm and width of 100nm-350nm in the sample co-evaporated at 0.8Å/s. We find that the evaporation rate of Bismuth plays a significant role in the growth of nanorods. From the GIXRD plot of variation in the evaporation rate of Bismuth, we have found that the hexagonal-axis symmetry of Bismuth triggers the growth of nanorods. The GIXRD plot of temperature-dependent grown samples further verifies this result. In the case of the sample deposited at 250°C, the formed nanowires were found to be longer than the previously reported literature. The average length of nanowires was 10-25μm, and the width was 300nm. The elemental mapping on these nanorods and nanowires confirmed the presence of Ni and Bismuth. We have also performed transmission electron microscopy on these nanorods and nanowires to ensure the elemental composition and crystalline behaviour fur-

ther. The nanorods were found to be polycrystalline $NiBi_3$ with different planes oriented at different angles, whereas nanowires were found to be single crystalline $NiBi_3$. Other than the single crystalline nature of nanowires, we have also found the nanowire tip was covered with an amorphous Bismuth layer which we have discussed in terms of the growth of nanowires in well known Vapour-Liquid-Solid (VLS) process. In a separate experiment, we exposed the thin film samples with 20kV electron beam where the growth of nanorods was observed in the sample with hexagonal-Bi. The superconducting transition temperature of a single crystalline nanowire was recorded and found to be 4.3K, same as the reported single crystal T_c.

Chapter 3

Signature of coexistent Ferromagnetism and Superconductivity in partial core-shell Bismuth coated Nickel nanoparticles

3.1 Introduction

Magnetic nanoparticles have found widespread application in the separation and purification of cells and biomolecules. This is attributed to their diminutive size, favorable separation capabilities, and excellent dispersibility. The integration of such magnetic materials into multi-component hybrid nanoparticles has garnered significant interest owing to their potential utility across various domains, including medical diagnostics, drug delivery [99], and magneto-plasmonics [100]. Studies involving core-shell configurations comprising ferromagnetic and antiferromagnetic materials [101, 102] and investigations into combinations of soft and hard ferromagnetic materials have gained considerable attraction. This is primarily due to the potential benefits of heightened magnetic exchange bias and increased coercive fields which are convenient tuning parameter for spintronic applications [103]. The hybrid nanoparticles incorporating both ferromagnetic and superconducting materials could be a fascinating area of research in such aspect. The proximity of superconducting and ferromagnetic materials introduces competing spin orderings, leading to a range of distinctive physical phenomena at the interface of S-F heterostructures. These phenomena hold both fundamental and applied significance. As a result the S-F hybrid structures have been widely studied in the literature [104, 105, 106, 107]. Damped oscillatory behaviour of the superconducting order parameter at a ferromagnetic interface [108, 109] and long range

spin triplet supercurrent at ferromagnetic interfaces with non collinear magnetic moment [110, 111] are a few examples. Although a large number of S-F bilayers and multilayers have been fabricated and studied [112, 106, 107, 113] in this context, there are no reports the S-F hetero-structures in nanoscale geometries such as nanoparticles. Small magnetic nanoparticles coated with a superconducting shell, for example, may be an interesting system to study proximity effect in the confines of the particle.

Previously, the coexistence of superconductivity and ferromagnetism has been documented in core-shell nanoparticles composed of Pb/PbO [114] and Sn/SnO [115], with Pb and Sn serving as the superconducting constituents. In these reports, the presence of ferromagnetism is traced back to imperfections and oxygen vacancies occurring at the interface between the metal and oxide layers on these core-shell structures. The challenge encountered in producing F-S nanostructures lies in the absence of suitable chemical methods for creating such structures where both superconducting and ferromagnetic properties are firmly established within the respective materials.

This chapter focuses on the production of isolated nanoparticles that possess both ferromagnetic and superconducting properties, achieved through a purely physical approach. When using a complete physical approach, a thin film of ferromagnetic material can be easily deposited in a single step. However, exposing the film to the environment is necessary for the formation of ferromagnetic (FM) nanoparticles. Subsequently depositing superconducting material (e.g., Nb) may fulfill the hybrid structure, but it often leads to damage at the interface of the superconductor (SC) and ferromagnet (FM), adversely affecting the physical properties. To address these challenges, we opted for Ni as the transition metal for the ferromagnetic component, and $NiBi_3$ as the superconducting component. $NiBi_3$ is formed through the self-diffusion of Bi into Ni. This self-diffusion phenomenon is driven by the high kinetic energy of Bi, coupled with the lower formation energy of $NiBi_3$ in comparison to Ni and Bi. Importantly, the interface is protected as it forms after the deposition

process of Bi. This innovative concept presents a promising avenue for creating core-shell nanoparticles with a superconducting $NiBi_3$ shell encapsulating a ferromagnetic Ni core.

3.2 Experimental details

3.2.1 Sample Preparation

3.2.1.1 Thin film growth

For the initial stage of SC-FM hybrid nanoparticle synthesis, Ni was chosen as the ferromagnetic material. Ni thin layers were deposited using an E-beam evaporation system, maintaining a base pressure of 1×10^{-7} mbar, onto commercially bought Si/SiO_2 substrate. The deposition process was closely monitored, achieving a consistent deposition rate of 0.1 Å/s via a quartz crystal monitor (QCM) integrated with the system. Before the deposition, the substrates underwent a thorough cleaning process involving immersion in acetone and isopropanol baths, followed by ultrasonication. Subsequently, these pristine substrates were positioned within the E-beam evaporation chamber utilizing a substrate holder clips. A series of Ni thin films were deposited with varying thicknesses: 5nm, 7nm, and 10nm. The deposited Ni films underwent subsequent processing stages to promote the formation of nanoparticles, and a comprehensive discussion of these stages is provided in the following sections.

3.2.1.2 Formation of Nickel Nanoparticles using Plasma Enhanced Chemical Vapour Deposition (PECVD)

To produce nanoparticles, the Ni thin films were annealed within a Plasma enhanced chemical vapour deposition system (PECVD). The thermal dewetting process transforms the thin film into an assembly of nanoparticles. This progression typically involves three stages: hole formation, hole growth and impingement, and ligament breakup. It is important to emphasize that dewetting takes place at temperatures significantly below the melting point

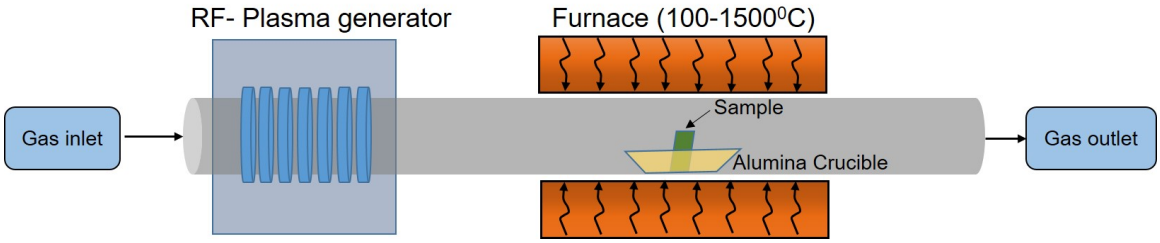

Figure 3.1: A schematic of the Plasma enhanced chemical vapour deposition system (PECVD). Typically sample is placed at the center of heating coil.

of the film, ensuring that the material remains in a solid state throughout this process. The thermal dewetting process occurred in the quartz tube here on the sample positioned at the center of the PECVD furnace, utilizing a forming gas environment consisting of 5% Hydrogen in Argon. Figure-3.1 illustrates the schematic of the PECVD system, where the sample's position is depicted at the center of the heating coil, a typical location for precise temperature control. The entire Quartz tube is connected to a vacuum system followed by dry scroll pump and turbo pump. An RF-plasma generator was employed to create plasma with the forming gas, ensuring a cleaner surface for the sample.

Several parameters were deliberately varied during the dewetting process, including the annealing temperature (ranging from 800°C, 900°C, to 1000°C), the duration of annealing (1 hour, 2 hours, or 3 hours), and the flow rate of the forming gas (ranging from 50sccm, 100sccm, 150sccm, to 200sccm). Prior to annealing, the CVD tube was pumped to a base pressure of 3×10^{-2} mbar and flushed several times with the forming gas. During the dewetting process, flow rate of forming gas was maintained at a fixed sccm observed through the mass flow controller(MFC) fixed on the gas mix chamber. The furnace temperature was planned to reach 900°C in 50 minutes, in a stepwise manner, once the gas flow rate was stabilised. A fixed plasma power of 150W was used at the maximum annealing temperature for the fixed duration of annealing. We have shown some of our optimization results with varying annealing duration and temperature in results and discussion section.

3.2.1.3 Formation of Bismuth coated Nickel Nanoparticles

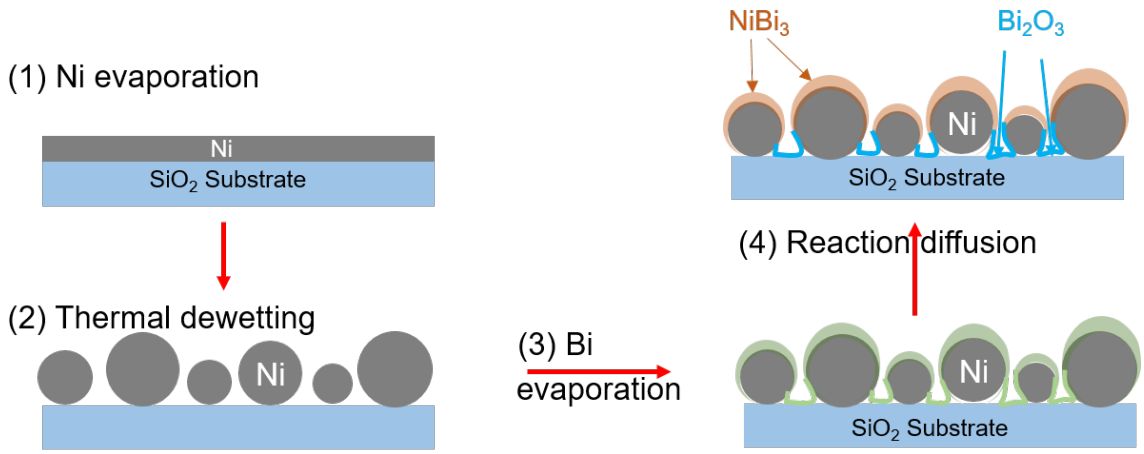

Figure 3.2: Schematic of steps for hybrid superconductor-ferromagnet nanoparticle formation.

For hybrid superconductor-ferromagnet nanoparticle preparation, a thin film of 5nm Bismuth was thermally evaporated onto the prepared Ni nanoparticle samples. Figure-3.2 represents the schematic of the complete process of superconductor-ferromagnet nanoparticle preparation. Step 4 of Figure-3.2 is a final schematic of the prepared sample. schematic view of a single superconductor-ferromagnet nanoparticle. It is very well known that Bismuth can diffuse into the Ni layer to form a superconducting layer of $NiBi_3$. So in the cross-sectional view, the upper layer shows the $NiBi_3$ formed due to the interdiffusion of Bi and Ni. The leftover Bi on the surface has been oxidized while exposed to the atmosphere as shown Bi_2O_3 on the surface of the substrate.

3.2.2 Magnetization measurements using vibrating sample magnetometry(VSM) in physical property measurement system(PPMS)

Magnetization measurements were conducted on both as prepared Ni nanoparticle sample and the Bi-coated Ni nanoparticle samples using the Vibration Sample Magnetometry (VSM) technique within a physical property measurement system (PPMS) setup. The VSM,

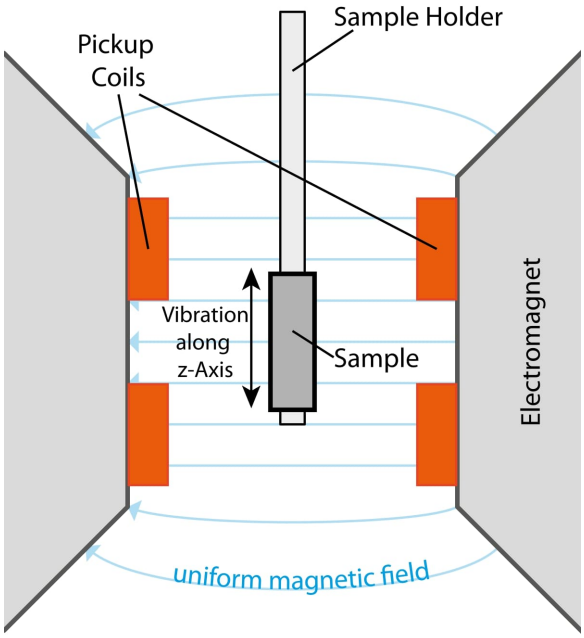

Figure 3.3: A schematic representation of Vibrating sample magnetometer (VSM) probe inserted in the physical properties measurement system (PPMS) equiped with in-build electromagnets.

also referred to as a Foner magnetometer, is a scientific instrument employed to assess magnetic properties by leveraging Faraday's Law of Induction. Figure-3.3 illustrates the schematic representation of the VSM probe, which is commonly inserted into a PPMS system featuring built-in magnets. The sample is affixed to the lower extremity of a sturdy rod and set into vertical oscillation, typically spanning a range of 0.1 to 1.5 mm and operating at frequencies between 10 to 100 Hz, often at 21 Hz (in our case 17Hz). When the sample is magnetized, either permanently or in response to an external applied field, the oscillation will induce an AC signal in a set of suitably placed pick-up or sense coils as shown in Fig-3.3. The amplitude of this signal is proportional to the magnetic moment of the sample. All signal analysis assumes that the moment is a magnetic dipole and that the size of the sample is much smaller than the dimensions of the pick-up coils. The pickup coils are matched and connected in opposite sense. In absence of a sample in position, an external field would in-

duce equal and opposite voltages in the two sets of pickup coils, producing no overall signal. Once in position upward motion of the magnetic sample causes an increase in flux through the upper pick-up coils and decrease in flux through the lower pick-up coils. The reverse is true for downwards motion of the sample. Therefore the overall voltage induced when sample is vibrating is proportional to, the magnetic moment of the sample. In VSM measurements, the proportionality constant often relates the applied magnetic field (in Tesla or Gauss) to the resulting magnetization (in emu or $A*m^2$). This constant may change based on sample geometry, calibration of the device, and measurement circumstances, among other things. It is crucial to calibrate the VSM equipment using recognised standards and protocols supplied by the manufacturer or developed in the field in order to receive correct measurements. This calibration procedure may yield the proportionality constant.The proportionality constant, as previously stated, connects the applied magnetic field to the resultant magnetization. This constant is measured during calibration by observing how a sample with known magnetic properties—like a standard reference material—responds to a range of known magnetic field intensities in terms of magnetization. These measurements are then used to derive the proportionality constant.

3.3 Results and discussion

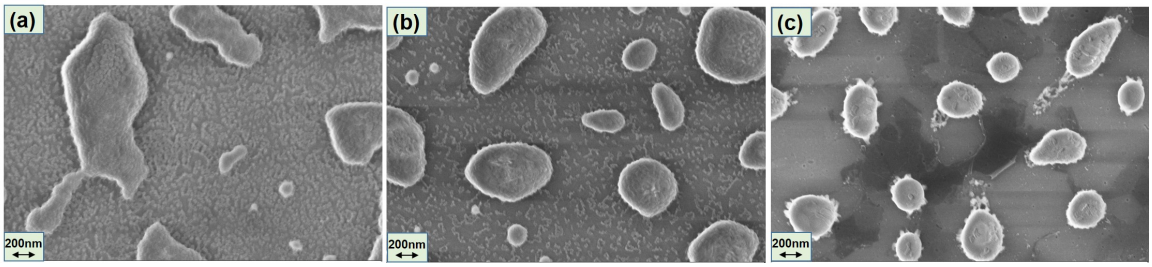

Figure 3.4: FESEM images of the Nickel nanoparticle samples with temperature of annealing variation: (a) 50sccm, 100W, (b) 100sccm, 100W, (c) 100sccm, 150W

3.3.1 Morphology characterization and EDAX mapping of Nickel nanoparticles

The morphological characterization of the prepared nanoparticle samples was conducted. As detailed in the sample preparation section, various parameters were adjusted to achieve the desired size distribution of nanoparticles. In Figures-3.4 and 3.5, we present some of the optimized FESEM results. Figure-3.4 illustrates FESEM images for three different Ni nanoparticle samples, with the annealing temperature fixed at 900°C while varying the flow rate of forming gas and plasma power. In Figure-3.4(a), where the flow rate was at a minimum of 50sccm, the shape and size of particles were abrupt, and the surface exhibited some residual constituents. Subsequently, increasing the flow rate improved the particle shape, as depicted in Figure-3.4(b). Further increases in plasma power to 150W resulted in a completely clean surface (Figure-3.4(c)). It is evident that the use of plasma enhances surface cleaning, and increasing the flow rate of forming gas improves the sharpness of nanoparticle size. Despite further increases in both the flow rate and plasma power, no significant changes were observed. Therefore, we adhered to the optimal parameters of a flow rate of 100sccm and a plasma power of 150W.

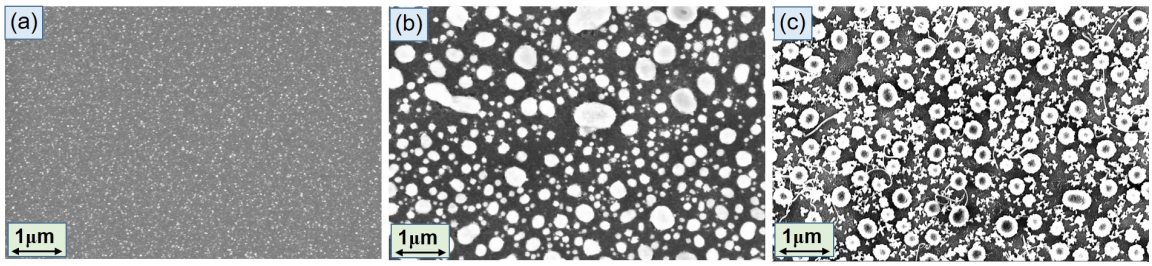

Figure 3.5: FESEM images of the Nickel nanoparticle samples with the temperature of annealing variation: (a) 800°C, (b) 900°C, (c) 1000°C

Likewise, Figure-3.5 showcases FESEM images of three different samples, where optimization was carried out with a fixed flow rate of 100sccm and plasma power at 150, while the annealing temperature was varied at 800°C, 900°C, and 1000°C. It is evident that at

800°C, the thin film dewetting process was not completed. At an annealing temperature of 1000°C, in addition to particles, thread-like connections were observed. However, at 900°C, the sample exhibited a well-distributed array of nanoparticles without any irregularities. So we followed with the best parameters from the optimization process as flow rate of 100sccm, plasma power of 100W, and annealing temperature of 900°C. Figure-3.6 shows the FESEM image of Ni nanoparticle samples prepared by de-wetting of 7nm Ni thin film annealed at 900°C for 3 different durations (a) for 1 hour (sample-A), (b) 2 hour (sample-B), (c) 3 hour (sample-C). The annealing process led to the transformation of the thin Ni film into various sizes of nanoparticles, constituting the solid-state de-wetting method [116]. It is evident that sample-A contains a higher number of smaller particles, approximately 50nm average size (Figure-3.6(d)). In contrast, sample-B and sample-C exhibit a noticeable decrease in the abundance of smaller nanoparticles.

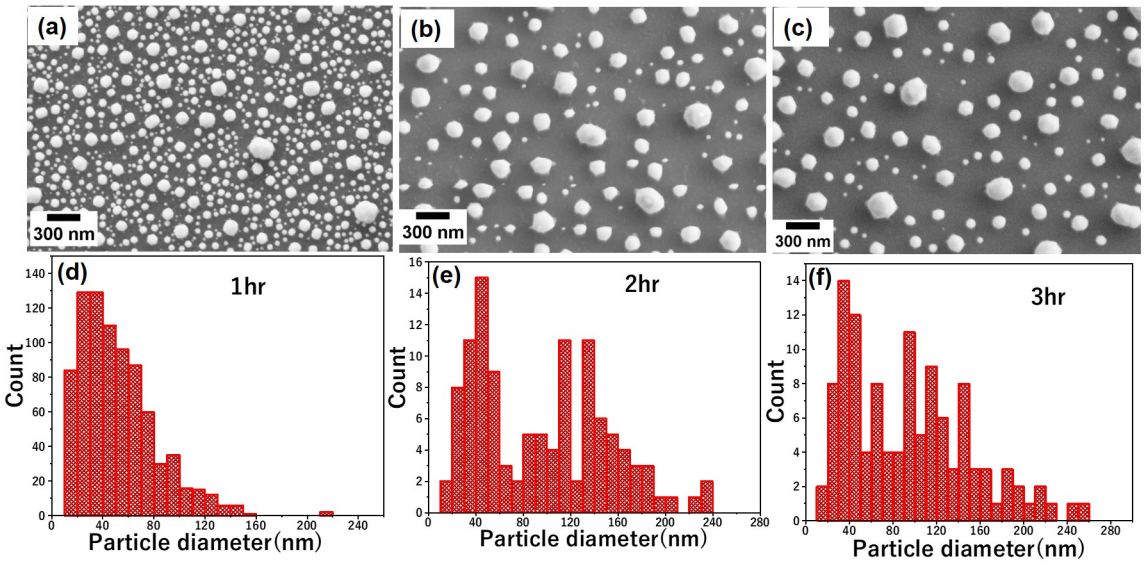

Figure 3.6: FESEM micrograph of Nickel nanoparticles annealed for 3 different duration (a) 1 hour (sample-A), (b) 2 hour (sample-B), (c) 3 hour (sample-C). The graphical plot of average size distribution of nanoparticles (d) sample-A, (e) sample-B, (f) sample-C.

Besides that, sample-B and sample-C exhibit an increase in the average number of particles with a mean size distribution of approximately 120nm as evident from Figure-3.6(e)

and (f). The primary difference between sample-A and sample-B/C lies in the duration of annealing. The difference between mean size is consistent with the well-known process called Ostwald's ripening [117]. The particle size and number of particles are entirely identical in sample-B and sample-C, indicating that the de-wetting process has reached its saturation point. To vary the shape and size of nanoparticles, we have experimented with several parameters, including annealing temperature (800°C, 900°C, 1000°C), flow rate of forming gas (100sccm, 150sccm, 200sccm), and plasma power (100W, 150W, 200W). After extensive testing, we discovered that the combination of 900°C annealing temperature, 150W plasma power, and 100sccm flow rate resulted in an excellent distribution and isolation of nanoparticles. Figure-3.7 shows the single Ni nanoparticle and EDAX mapping of

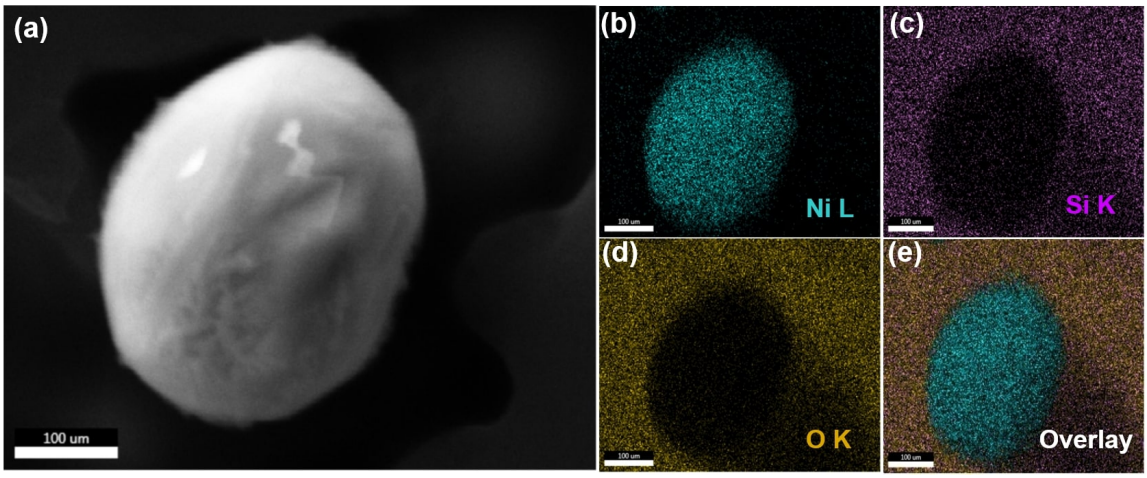

Figure 3.7: SEM image of a single Nickel nanoparticle. EDAX mapping of that nanoparticle showing elements such as Ni in (b), Si in (c), O in (d), and overlay image in (e).

the corresponding nanoparticle. Here it is evident that Ni is present only on the nanoparticle and Oxygen is completely absent on the same. After the annealing process, the nanoparticle is completely de-wetted into a single Ni nanoparticle.

3.3.2 Magnetic characterization of Nickel Nanoparticle

We have performed magnetization measurements on the prepared Ni nanoparticle samples.

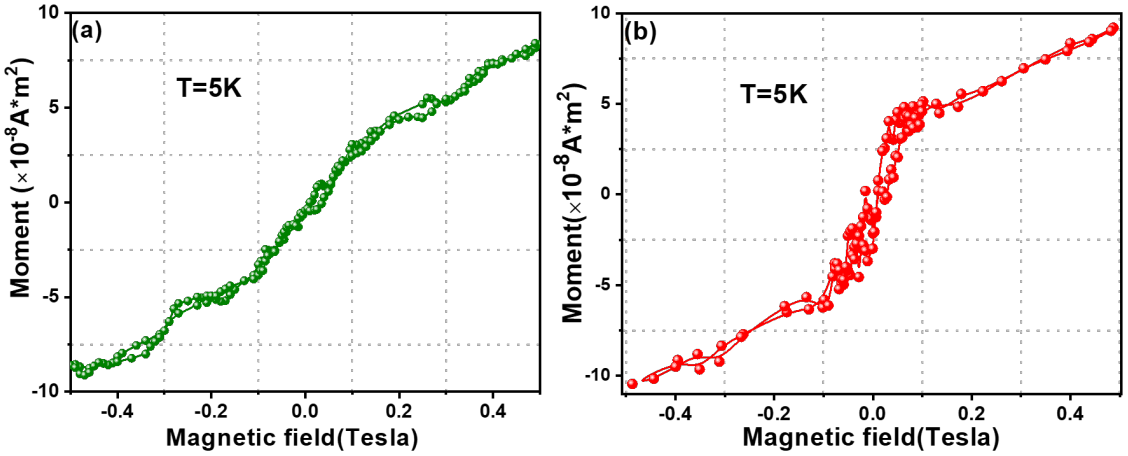

Figure 3.8: Magnetization(M) vs magnetic field(H) plot for nickel nanoparticle sample annealed for 2 different duration 1 hour(a) and 2 hour(b) respectively.

Figure-3.8 depicts the plots of magnetic moment versus magnetic field for two samples annealed for different durations: 1 hour (a) and 2 hours (b). Since there was no significant change in the average particle size from the 2-hour sample to the 3-hour sample, the magnetic hysteresis *MH* results for these two samples are identical. Therefore, we present the results only for the 1-hour and 2-hour annealed samples. It is evident that in one case, there is a higher abundance of smaller-sized nanoparticles, while in the other case, a bimodal distribution of particles is observed. Magnetic measurements were conducted with the magnetic field perpendicular (out of plane) to the sample surface. The applied magnetic field was scanned over the range of -0.5T to +0.5T at a temperature of T = 5K. From *MH* measurement for both the samples, it is observed that sample A shows a significantly weaker ferromagnetic response with almost negligible hysteresis, which can be attributed to its smaller mean particle size (50nm). Regarding sample B, which contains a higher number of larger nanoparticles, the ferromagnetic signature is more evident; however, the magnetization curve still exhibits only a slight amount of hysteresis. Previous reports [118] indicate that ferromagnetic nanoparticles behaves single domain like when their diameter falls below a critical value of approximately $D_s \sim 100$nm. This transition is a consequence

of the interplay between dipole energy and exchange energy [119]. Thermal excitation can flip the moment of the individual isolated nanoparticles along the magnetic easy axis of a collection of tiny single-domain ferromagnetic nanoparticles with low dipole-dipole interaction. The magnetic behavior belongs to the category of super-paramagnetic material if the magnetic easy axes of all the nanoparticles in the collection are not aligned in the same direction and the collection's net magnetization does not exhibit considerable hysteresis. Earlier studies [120] have shown that in the superparamagnetic limit, the coercive field of a collection of randomly oriented magnetic nanoparticles almost vanishes. This explanation of extremely low (negligible) coercive is apparent in Figure-3.8(a) and (b) for both samples A and B. But other than that, in the case of *MH* curve for sample-B(Figure-3.8(b)) a low but considerable remanence magnetization is observed. The observed magnetization remanence can be attributed to the presence of larger nanoparticles, with a mean size 140nm (as depicted in the histogram plot Figure-3.6(e)). These larger nanoparticles undergo a reversal of their magnetic orientation when subjected to an applied magnetic field. However, upon reducing the field strength, the moments and directions of each particle cannot return to their original state. This outcome aligns with findings reported in the literature [119] regarding single-domain nanoparticles in the superparamagnetic regime. Glancing-angle XRD was conducted on these Ni nanoparticle samples to examine potential signatures of NiO formation on the nanoparticle surface, which typically induces antiferromagnetic behavior [121]. However, no evidence of NiO formation was detected in these measurements. Subsequent magnetic characterization of the dewetted nanoparticles involved the evaporation of a thin layer of Bi onto these particles.

3.3.3 Elemental and morphology characterization of Bismuth coated Nickel nanoparticles

The Bi-coated Nickel nanoparticle samples underwent morphological characterization using FESEM (Field Emission Scanning Electron Microscopy). Figures-3.9(a) and (b) present scanning electron micrographs after a thermal coating of approximately 5 nm thick Bi film on samples A and B, respectively. Both images were acquired at the same magnification as in Figs 3.6(a) and 3.6(b) to maintain consistency in the comparison. Despite the thinness of the deposited Bismuth layer (5 nm), its appearance is granular in texture, as clearly observed in these SEM images. The deposition of Bi was carried out at an elevated substrate temperature of 150°C. Given Bismuth's low melting point (about 270°C), it is expected that such a thin layer deposited at an elevated substrate temperature would exhibit fissures or a granular form, as previously reported [122]. The similarity in the granularity of the deposited 5 nm Bi film on both the bare substrate and the Ni nanoparticles leads to the conclusion that, in this particular case, the Ni nanoparticles do not play a specific role in the granularity of the Bi film.

Based on the observations from Figure-3.9(a) and (b), it is evident that the individual nanoparticles are distinctly separated, with no significant aggregation. Moreover, the nanoparticles are effectively coated with Bismuth on their surfaces. Nonetheless, the absence of a continuous Bismuth film extending from the top of the nanoparticles onto the substrate is notable. In Figure-3.9(c), a FESEM image of a single Bi-coated Ni nanoparticle reveals the presence of granular Bi on its surface. Elemental mapping on this individual nanoparticle clearly indicates the presence of both Ni and Bi on the top of the particle, while there is availability of Bi in the vicinity of the nanoparticle. Nevertheless, the findings from earlier reports by various research groups support the consistent occurrence of the $NiBi_3$ phase formation. The outer layer of $NiBi_3$ is anticipated to follow the fissure patterns

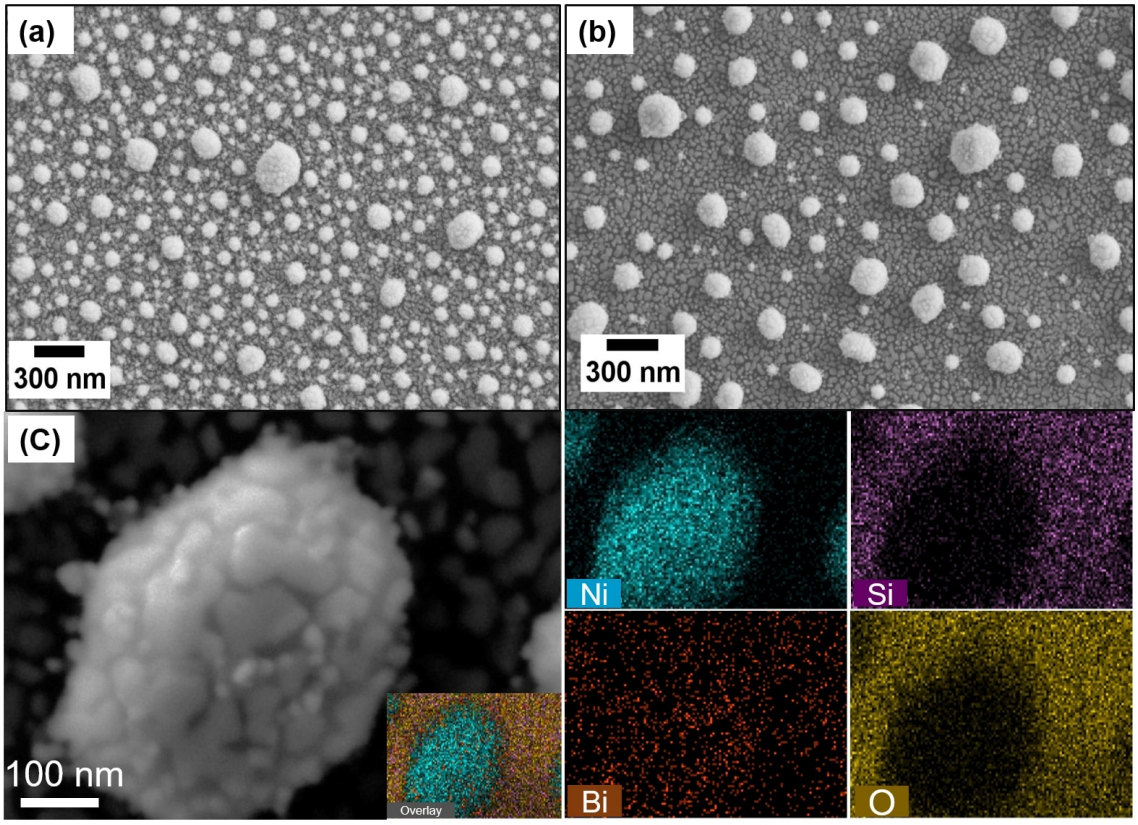

Figure 3.9: Magnetization(M) vs magnetic field(H) plot for nickel nanoparticle sample annealed for 2 different duration 1 hour(a) and 2 hour(b) respectively.

of the deposited Bi layer, as opposed to the continuous shell-like layer that is generally achieved in chemically grown core-shell particles. The absence of oxygen signal on the particle in the EDAX mapping suggests that the Bi layer has not oxidised. We go through the structural features and superconductivity in $NiBi_3$ in these Bi-coated Ni nanoparticles in the next subsections.

3.3.4 Characterization of Bi coated Nickel nanoparticles by X-ray diffraction

Figure-3.10 shows the Glancing angle X-ray diffraction for the Bi-coated Ni nanoparticle sample. GAXRD was done at different incident angles from I=0.05deg to 0.5deg. It is

observed from this plot that, with increasing incident angles, the intensity of Ni(111) peak and Ni(002) peak gradually increase, as expected due to the larger penetration depth of the x-ray at higher incidence angles. We observe that the Ni (111) and Ni (002) peaks

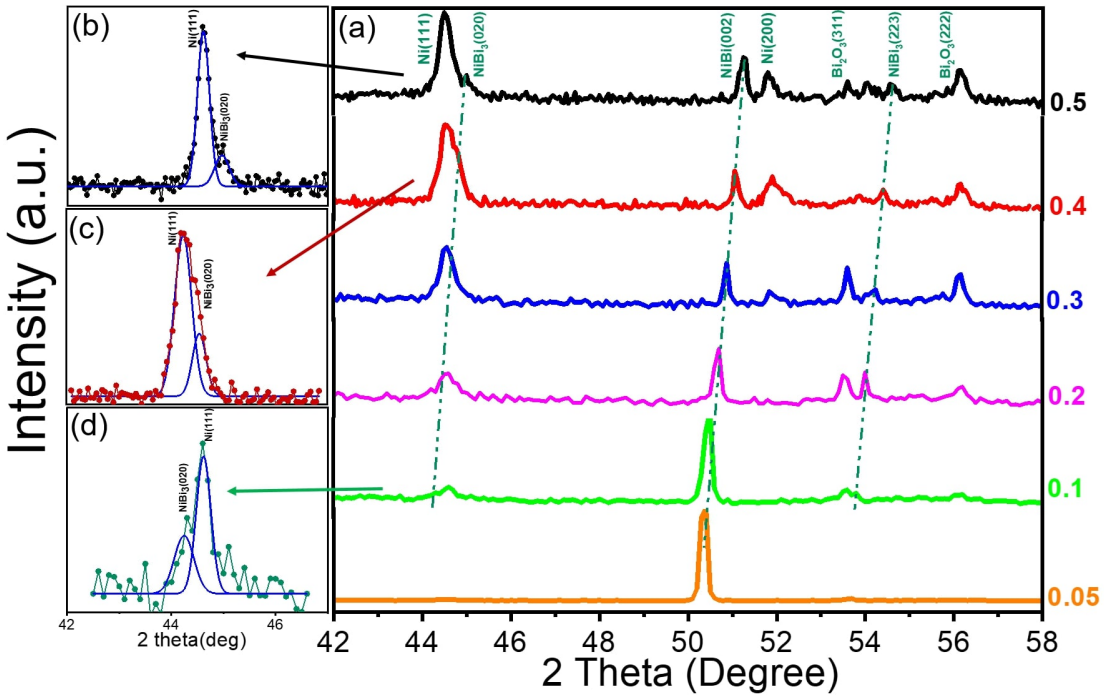

Figure 3.10: (a) Glancing incidence X-ray Diffraction of Bi-coated Ni nanoparticles at different incident angles between 0.05 and 0.5 degrees. Panels (b), (c) and (d) show the magnified view in the range of 43 degrees to 46 degrees for the incidence angles 0.5, 0.4 and 0.1 degrees, respectively. The de-convoluted Ni(111) and $NiBi_3$ (020) peaks are also plotted along with the experimental data. It shows that the $NiBi_3$ peak shifts to the higher 2-theta values with increasing angles of incidence.

remain unchanged in their positions regardless of the incidence angle. Similarly, the Bi_2O_3 (311) and (222) peaks exhibit no shifting as the incident angle is altered. However, we notice a strong NiBi (002) peak at the lowest incidence angle, which progressively moves towards the higher 2-theta values as the incidence angle increases. Similarly, 2 $NiBi_3$ peaks corresponding to lattice planes (0 2 0) and (2 2 3) are also shifting to the higher 2-theta value. The dashed lines in Fig-3.10(a) show this apparent peak shift. Due to the proximity of the Ni(111) and $NiBi_3$(020) peaks, we have presented an enlarged depiction of these

specific peaks (within the 2-theta range of 43 to 46) in panels (b), (c), and (d). These panels correspond to incident angles of 0.5 degrees, 0.4 degrees, and 0.1 degrees, respectively. The de-convoluted Ni(111) and $NiBi_3$(020) peaks have also been shown in these panels. At incident angles of 0.3 and 0.2 degrees, the two peaks merge entirely as a result of the shifting peak position of $NiBi_3$(020) with respect to the incident angle.

It is noteworthy that there is no shift observed in the Ni peak, suggesting the absence of any scattering channels that could arise from isolated nanoparticles dispersed in a substrate during the analysis of glancing-angle X-ray scattering [123]. In the context of the current investigation, alternative scenarios for the observed shift in peak positions arise, particularly considering the outer edge of Ni nanoparticles where the diffusion layers of NiBi and $NiBi_3$ may experience distinct levels of strain at varying depths. Drawing parallels with the work of Huang et al. [124] on irradiated W thin films, the possibility of a sub-surface strain profile is contemplated. However, the unique geometry of the diffracting volume, composed of nearly spherical particles as opposed to a flat sheet, poses a challenge for a comparable modeling approach. To unravel the intricate strain dynamics, we undertake an exploration of different depths within the sample by manipulating the incident glancing angle of X-ray. The attenuation length of Cu K radiation, pertinent to $NiBi_3$ and NiBi, spans from 2 nm to 20 nm for incidence angles ranging between 0.01 and 0.5 degrees. Consequently, it is plausible that the observed peak shift with varying incidence angles is indicative of the nuanced variations in strain occurring at diverse depths within the sample. An alternative elucidation for the observed peak shift could stem from geometric considerations. The discerned strain apparent in the incident X-ray manifests an augmentation with an increasing angle of incidence owing to the configuration of $NiBi_3$ as a thin layer enveloping the spherical surface of Ni particles. Consequently, the peak position may exhibit variations contingent upon the angle of incidence. The manipulation of the incidence angle affords the exploration of distinctive depths within the specimen, thereby providing initial insights

into its stratified composition, as depicted in Figure-3.10. A notable observation lies in the conspicuous absence of peaks corresponding to pure Bi, indicating the comprehensive diffusion of Bi into Ni nanoparticles and the subsequent formation of NiBi and $NiBi_3$ phases. It is imperative to acknowledge potential surface imperfections, such as fissures, within the layer. During X-ray diffraction measurements conducted within a few weeks of sample preparation, the prevalence of the NiBi phase on the surface was evident. Concurrently, the Bi layer deposited proximate to the bare substrate adjoining the Ni particles underwent oxidation, culminating in the formation of Bi_2O_3. Remarkably, the X-ray diffraction peak corresponding to the (222) planes of Bi_2O_3 remains constant irrespective of the incidence angle, as illustrated in Figure-3.10(a). Consequently, the elucidated peak shift observed in the $NiBi_3$ and NiBi phases likely originates from geometric factors, as discussed in the antecedent paragraph.

3.3.5 Characterization of Bi coated Nickel nanoparticles by Transmission Electron Microscopy (TEM)

In order to confirm the findings from the x-ray diffraction analysis discussed earlier, we performed high-resolution transmission electron microscopy (TEM) on the nanoparticles. Both Ni nanoparticles and Bi-coated Ni nanoparticles were transferred from Si/SiO_2 substrates to carbon-coated copper grids for the TEM investigations. Figure-3.11 represents the results obtained from bright-field TEM examination of a single Ni nanoparticle. In Figure-3.11(a), the hexagonal morphology of the particle is distinctly evident, consistent with our field emission scanning electron microscopy (FESEM) images. Figure-3.11(b) provides an HRTEM image of a magnified section of this particular nanoparticle, revealing its single crystalline nature. The Gatan Microscopy suite was employed to compute the inter-planar spacing (d) based on the observed fringe patterns. In Figure-3.11(a), the calculated ”d” value was determined to be 0.203 nm, corresponding to the Ni(111) planes. This Ni(111)

plane is associated with a 2-theta angle of 44.5 degrees, as demonstrated in XRD Figure-3.10(a). Notably, the uncertainty in the estimation of d-values was approximately 0.0002 nm, determined by evaluating the variations of d-values from the same fringes sampled across multiple locations. The atomic structural model representation of the (111) plane of Ni is depicted on the right-hand side of Figure-3.11(c), utilizing VESTA software [82]. This representation aligns well with the d-spacing calculated from the HRTEM image.

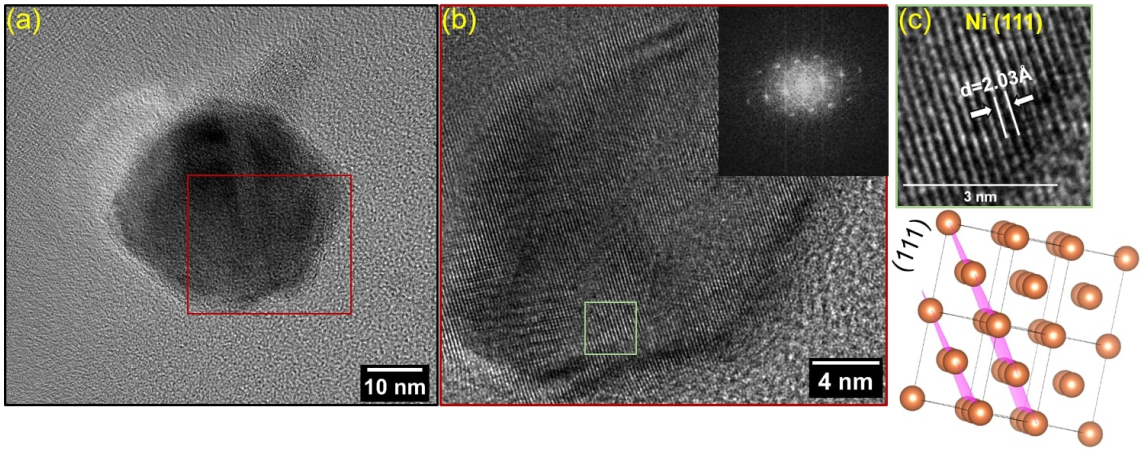

Figure 3.11: (a) TEM image of Ni nanoparticle, (b) HRTEM of the selected area RED marked square box in (a), Inset: Fast fourier transform (FFT) of the selected area. (c) Zoomed view of the specified region in (b) showing Ni (111) plane with corresponding 2D-model representation using VESTA program.

We show the bright field image and the HRTEM image of a Bi coated Ni nanoparticle in the Figure-3.12(a). Inset in the Figure-3.12(a), shows the low magnification of nanoparticle, the hexagonal shape is well matching with the FESEM image. Other than this, there are some leftover region visible towards the left of nanoparticle which is nothing but the scratched Bi_2O_3 from the surface of substrate as it is not so easy to exclude the surface material during scratching process. From the TEM image in the inset, it is clearly observed that the boundary of the nanoparticle is not clean but covered with another layer. In order to further ascertain this, we have presented a zoomed HRTEM image of square marked region in Figure-3.12(a). In Figure-3.12(a), there is an observable boundary region at the edge

of the larger nanoparticle, which appears to vary across different plane orientations. This boundary region displays a clearly defined curvature along the circumference of nanoparticle. Moving to the high-resolution depiction in Figure-3.12(b), a distinct boundary layer is evident, demarcated by dashed lines. This layer stands apart from the planes constituting the inner Ni particle.

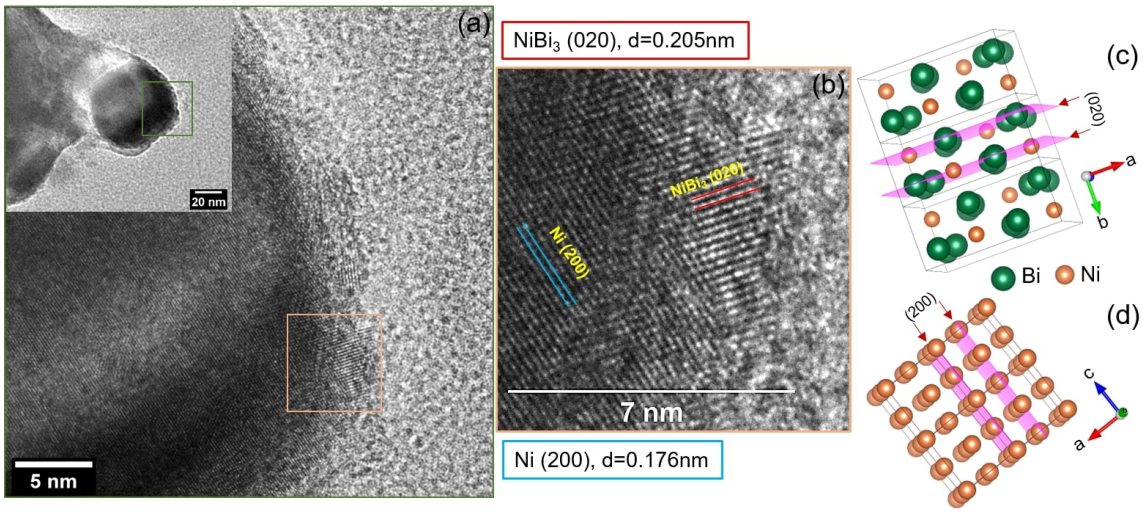

Figure 3.12: (a) HRTEM of Bi coated Ni nanoparticle zoomed view of the selected Green square box in Inset: Low magnification TEM image of the same particle. (b) Zoomed view of the marked square box in (a) showing Ni (200) plane and $NiBi_3$ (020) plane. Panel (c) and (d) show the 2D-model representation of $NiBi_3$ and Ni crystal structure with corresponding planes.

Strikingly, this boundary layer closely resembles the fissured structure observed in the Bi film atop the Ni particles, as depicted in the FESEM image found in Figure-3.9. In contrast, when compared, the boundary of the as-dewetted Ni particle seems considerably pristine, showcasing a solitary crystal orientation, as depicted in Figure-3.11(a). Further analysis through magnification of the high-resolution transmission electron microscopy (HRTEM) image reveals that the inter-planar spacing within the boundary region shown in Figure-3.12(b) measures 0.205 nm, which corresponds to the (020) planes of $NiBi_3$. Here the shell of $NiBi_3$ is observed on the core Ni (200) plane of inter-planar spacing 0.176nm

consistent with the XRD plot Figure-3.10. A visual representation of the atomic structure is also provided on the right-hand side for clarity. It is crucial to note that $NiBi_3$, formed at the Ni/Bi interface, undergoes strain, as indicated by the observed shift in peak positions in the grazing-angle X-ray diffraction (GAXRD) measurements (Figure-3.10), which is angle-dependent. However, directly quantifying this strain at this resolution from TEM images poses challenges. Due to the strain at the interface, the inter-planar spacing within the curved $NiBi_3$ boundary varies, ranging from 0.202 nm to 0.205 nm, a result we have extensively validated. No signature of the NiBi phase was identified. The Ni-Bi binary phase diagram [11] indicates that at normal temperatures, the $NiBi_3$ phase is significantly more stable than the NiBi phase, which has a much higher energy of formation. Consequently, over time, NiBi transforms into the $NiBi_3$ phase through partial diffusion reactions, driven by the higher stability of the $NiBi_3$ phase [11].

$$2Bi_{(\text{Diffusion})} + NiBi = NiBi_3 \tag{3.1}$$

Hence, we are unable to detect any discernible indication of the NiBi phase in the high-resolution transmission electron microscopy conducted well after the X-ray diffraction measurements. It's noteworthy that NiBi also exhibits superconducting properties, sharing a comparable transition temperature with $NiBi_3$.

3.3.6 Magnetic Characterization of Bi coated Nickel nanoparticles

As delineated in the extant literature [29], $NiBi_3$ has been recognized as a superconducting alloy exhibiting a critical temperature (*Tc*) of 4.2 K. Our preceding sections' observations provide insights into the formation of a thin $NiBi_3$ layer, functioning as a cap, encapsulating the larger Ni nanoparticles. The elucidation of the fabrication methods and the discernment derived from FESEM images unequivocally indicate the successful segregation of Ni nanoparticles coated with Bi. Consequently, owing to this arrangement of isolated

nanoparticles, traditional resistivity measurements become impractical for probing the intrinsic superconducting behavior within these Bi-coated Ni nanoparticle samples, as explicated earlier. In this context, the manifestation of the diamagnetic transition, recognized

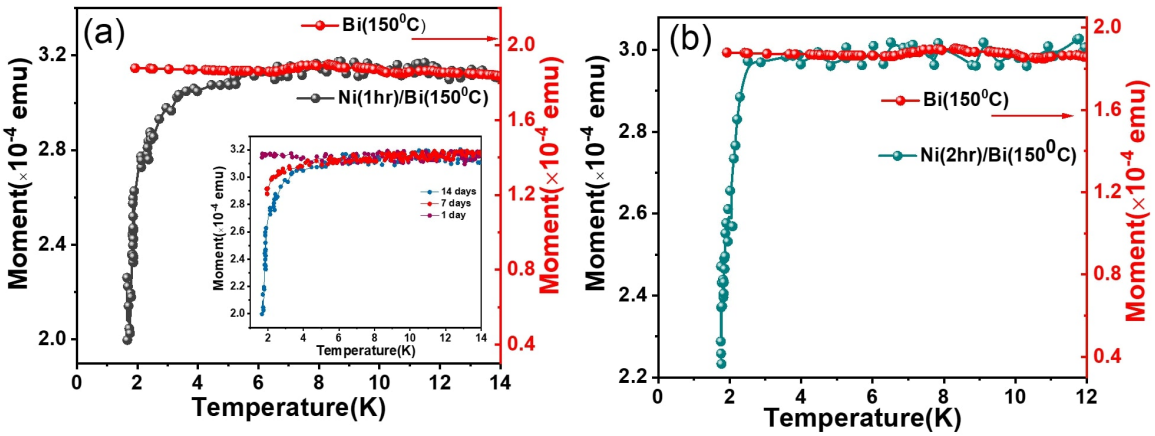

Figure 3.13: The left hand axes of panels (a) and (b) show the temperature dependent magnetic moment(M) of the Bismuth coated Nickel Nanoparticle samples A (smaller average particle size) and B (larger average particle size), respectively. In both cases, the right hand axis shows the background signal of the plane Bi film. The inset in the panel (a) shows the *M(T)* data of the Bi coated A sample measured at different times showing a gradual evolution of the $NiBi_3$ superconducting phase due to reaction diffusion of Bi into Ni.

as the Meissner effect, assumes prominence as a distinctive indicator of superconductivity, providing a mechanism for ascertaining the transition temperature. This approach aligns with established methodologies in academic literature, especially when conventional resistance measurements are impractical, as illustrated in instances involving organic superconductors [125]. The detection of a diamagnetic transition proximate to the recognized critical temperature (*Tc*) of bulk $NiBi_3$ remains the exclusive avenue for discerning vestiges of superconductivity within these nanoparticles, precluding measurements via scanning tunneling microscopy. In the present investigation, equilibrium magnetic moment (M) vs temperature (T) measurements have been conducted to scrutinize any potential diamagnetic.

Figure-3.13(a) and (b) display the magnetic moment versus temperature profiles for

sample-A and sample-B, respectively, with both measurements conducted under an applied magnetic field of 0.1T perpendicular to the sample surface. Notably, the diamagnetic transition initiates at 3K for sample A and at 2.5K for sample B, as evident from these plots. Strikingly, the profiles reveal an intriguing observation: contrary to the anticipated negative value characteristic of the superconducting state, the total magnetic moment maintains a positive orientation throughout the measurement range, extending down to the lowest attainable temperature of 1.9K. This outcome is consistent with expectations, considering the predominant magnetic contribution from the larger Ni nanoparticle compared to the thinner $NiBi_3$ layer. In the current context, the observed diamagnetic transition temperature is marginally lower than the previously reported Bulk *Tc* [13]. An inset within Figure-3.13(a) illustrates the *MT* plot for the sample at various time points (1 day, 7 days, 14 days), revealing the progressive development of the $NiBi_3$ superconducting phase due to the reaction diffusion of Bi into Ni. This finding aligns with prior literature [70], which suggests a specific duration for this reaction diffusion process. Additionally, it is observed that the sample with the lower average particle size exhibits a somewhat higher initiation temperature for the diamagnetic transition. The observed decline in the critical temperature in this scenario may be attributed to larger Ni nanoparticles exerting a more pronounced magnetic proximity impact on the superconducting $NiBi_3$.

The right hand side axis in both the *MT* plots show moment vs temperature plot for pure Bi deposited on Si/SiO_2 substrate at the same condition as the surface layer of Bi coated Ni nanoparticle. The intrinsic magnetic moment of a planar bismuth (Bi) film deposited on a Si/SiO_2 substrate is examined. The film thickness aligns with that of the Bi layer applied to samples A and B. The growth of this Bi film transpired within the identical deposition cycle used for coating Bi onto samples A and B. The background magnetization curve of Bi, as depicted in Fig-3.13, encompasses the magnetic response attributed to the naturally formed Bi_2O_3 layer. Notably, this Bi_2O_3 layer is also present in samples A1 and A2 within

the inter-particle regions. Consequently, we can confidently disregard the diamagnetic response stemming from the underlying Bi film. The information within Figure-3.13(a) and (b) demonstrates an absence of diamagnetic transitions within the Bi/Bi_2O_3 film, extending down to the lowest temperatures of measurement. Consequently, we deduce that the observed diamagnetic transitions in the Bi-coated samples A and B must indeed arise from the formation of $NiBi_3$ on the Ni nanoparticles. Here, it is important to highlight that a number of alternative theories on the development of superconductivity in Ni-Bi systems have been covered in the literature. LeClair et al. [57], for instance, previously investigated superconductivity in Ni/Bi bilayers by studying the altered band structure of Bi in proximity to Ni. Their research focused on the tunnelling conductance in Al(4.2 nm)/Al_2O_3/Ni(1.6 nm-5.4 nm)/Bi(40 nm) junctions. In contrast, various studies by other research groups [29, 13] consistently report the development of $NiBi_3$ at the Ni and Bi interface, regardless of the film growth order, at ambient temperature. In an alternative interpretation of superconductivity in Ni-Bi bilayers, Gong et al. [31] demonstrated the emergence of superconductivity with a non-trivial symmetry within the bulk of Bi adjacent to an extremely thin Ni layer in epitaxial Ni-Bi bilayers. Notably, their study involved large Ni particles with a fine layer of Bi, differing from our distinct scenario. Our X-ray diffraction (XRD) and high-resolution transmission electron microscopy (HRTEM) analyses of Bi-coated Ni particles have not indicated the presence of Bi; instead, we observe $NiBi_3$ at the boundaries of Ni particles. Consequently, the origin of superconductivity, leading to the observed diamagnetic response below approximately 3 K, can be ascribed to the development of the $NiBi_3$ phase.

3.4 Summary

This chapter is dedicated to the fabrication of nanoparticle samples that combine both ferromagnetic and superconducting properties (Ni-$NiBi_3$), achieved entirely through a physical methodology. The procedure initiates with the creation of ferromagnetic Ni nanoparticles via the solid-state dewetting process involving e-beam evaporated thin Ni films. By manipulating the duration of annealing, distinct size distributions were achieved, with mean values clustering around 50 nm and 120 nm, respectively. Magnetic hysteresis (*MH*) measurements performed on these nanoparticle samples exhibit superparamagnetic behavior, consistent with existing literature [119]. A layer of Bi with a thickness of 5 nm was deposited onto these nanoparticles at an elevated temperature of 150°C to facilitate the formation of an outer $NiBi_3$ layer. The well-established process of reaction diffusion drives the development of this $NiBi_3$ outer layer on the nanoparticle surfaces. Glancing angle X-ray diffraction performed with varying incidence angles confirmed the presence of $NiBi_3$ at the interface of Ni. High-resolution transmission electron microscopy (TEM) images of these nanoparticle samples provide further substantiation of the formation of the outer $NiBi_3$ layer on the Ni nanoparticles. The superconducting behavior was verified through magnetization versus temperature measurements, revealing a diamagnetic transition occurring at around 3 K. Varying the time gap between deposition and measurement spanning 1 day, 7 days, and 14 days we demonstrated the gradual diffusion of Bi into Ni to form $NiBi_3$, which correlates with established literature [70]. Comparative analysis of the *M(T)* measurements unveiled that the initiation of diamagnetic response transpired at a slightly lower temperature in the sample containing a larger average Ni size. This suggests a relatively stronger magnetic proximity effect in this configuration.

Chapter 4

Role of magnetic impurity on the resistive state transport of $NiBi_3$ Nanowires below Tc

4.1 Introduction

Superconductors carry lossless current [126] via Cooper pairs formed by phonon mediated coupling of a pair of electrons. The cooper pair order parameter is represented by the wave function

$$\psi(\mathbf{r}) = \sqrt{n(\mathbf{r})}e^{i\phi(\mathbf{r})} \tag{4.1}$$

, where $|\psi|^2 = n(\mathbf{r})$ is the density of superconducting Cooper pair, ϕ is the phase of the order parameter which is constant over a superconducting sample. This is a typical property in any superconducting bulk and thin films, but the situation is different in a low dimensional superconducting sample specially in wide stripes, nanowires etc. It is now very well known that in lower dimensional superconductors below T_C the long-range order can destroyed locally by fluctuations [127] which leads to suppression of superconductivity in certain parameter space. Therefore, understanding the cause and effect of local fluctuations in superconducting nano systems is a necessity from application point of view. A number of physical phenomena have been observed for low dimensional superconductors such as a wide superconducting transition in resistance *(R)* vs temperature *(T)* curve [128], large transition region between the first finite voltage and completely normal state region in current voltage characteristics (CVCs) [129]. The wide transition and a finite resistance in *RT* curve as well as in *IV* curves is the early signatures of a well known concept called Phase

slips. Phase slip occur as phase slip centers (PSCs) in 1-D nanowires [130] and Phase slip Lines (PSLs) in 2-D wide stripes [131]. The Cooper pair order parameter essentially undergoes fluctuations during phase slip events, occurring locally and at random points, resulting in the generation of finite voltage or resistance. Throughout a phase slip process, the superconducting order parameter fluctuates to zero at various points along the nanowire. As the phase of the order parameter slips by 2π, this induces a finite voltage at each phase slip point, the summation of which leads to an effective voltage or finite resistance. The cumulative impact of these phase slip events becomes evident in superconducting nanowires with dimensions characterized by $\xi(T) \ll$ width(w) $\ll \lambda_{eff}(T)$ [132, 133], noteworthy that the width (w) $\ll \xi(T)$ and $\lambda_{eff}(T)$. The investigation into the dissipation nature in low-dimensional superconductors below the critical temperature (T_c) has garnered attention due to the widespread application of superconducting nanowires in classical and quantum information-processing devices [134, 135, 94], photon detectors [136], among other areas. Therefore, it is imperative to delve into the study of understanding the causes of phase slip fluctuations and identifying the influencing factors.

So, in this context our aim is to study the effect of magnetic impurity on the phase slip activity in the $NiBi_3$ sample. The $NiBi_3$ is a unique system to study these effects because of in build presence of Ni impurity as well as the superconducting T_c of $NiBi_3$ is robust to the presence of magnetic impurity. Other than the study of phase slip phenomena in the $NiBi_3$ nanowires, we have also studied the magneto-transport properties in this system. The thin $NiBi_3$ film was found to be granular in our case and transport in granular superconducting films is often interpreted in terms of a coupled network of Josephson junctions, where individual grains with well defined superconducting order parameters couple across the grain boundaries. In such an aggregation, Abeles [137] has demonstrated that the inter-grain charging energy resulting from a finite inter-grain capacitance is crucial for determining the system's critical response. Mesoscopic phase variations are inherently present in mul-

tiplexed superconducting grains due to the distribution of intergrain charging energy (or, more accurately, the distribution of capacitance). Phase fluctuations translate to Cooper pair number fluctuations in a reciprocal manner because the phase and the number of Cooper pairs are conjugate variables inside a superconducting grain. The superconducting grains connected via the inter-grain boundaries can be imagined as the SNS junctions. Mesoscopic current fluctuations can totally control the transport in disordered SNS junctions [138], particularly near the limit of suppressed current across the junction. When magnetic inter-grain zones separate superconducting grains, a condition like this can occur [139]. In the $NiBi_3$ granular films, the inter-grain boundaries are expected to be magnetic. So in order to study the effect of such magnetic impurity in such physical phenomena we have analyzed the *MR* properties of $NiBi_3$ nanowire.

4.2 Experimental details and standard characterization of the test samples

4.2.1 Thin film growth

To study the phase slip fluctuations we need to fabricated $NiBi_3$ nanowires from a uniform layer or form of the same is necessary. It is very well known that $NiBi_3$ forms at the interface of Ni and Bi which is not a uniform film of only $NiBi_3$ due to the continuous layer of Nickel underneath as well as a continuous layer of Bi or Bi-oxides over it. For this purpose we have prepared a uniform thin film of $NiBi_3$ using co-deposition of Ni and Bi. Here in the present study our aim was to study the effect magnetic impurity on phase slip fluctuation, for which a variation of magnetic impurity in the sample is necessary. As we know $NiBi_3$ consists of Nickel as magnetic impurity in it. So to vary the Ni atomic concentration a homemade setup was prepared.

A series of thin film of $NiBi_3$ were prepared at ambient temperature using the combi-

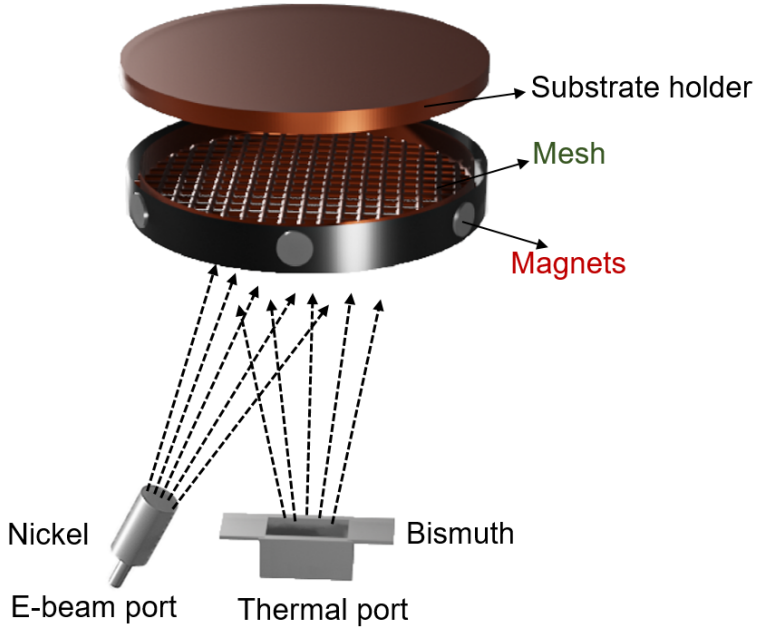

Figure 4.1: Schematic of the deposition set up for the co-deposition of thin film

nation of electron-beam and thermal evaporation process while Ni was e-beam evaporated, Bi was thermally evaporated simultaneously. Since our aim Here our aim was to study the effect of magnetic impurity, we co-evaporated Ni and Bi in two different conditions. In one case the co-evaporation was done in the normal way by placing the cleaned Si/SiO_2 substrates in front of the evaporation flux. Since in this method, individual metals are independently evaporated, maintaining the stochiometry of $NiBi_3$ required careful optimization of the evaporation rates. However, we find that some Ni content still remains in the co-evaporated $NiBi_3$ films as discussed in previous chapters, finding a way to control the Ni is necessary. For this purpose we have made a set up with a mesh connected with 6 magnets as shown in the schematic Figure-4.1. These magnets were placed equally opposite to each other. In this way, the magnetised mesh was acting as magnetic filter so that Nickel reaching to the substrate will be obstructed at the the mesh connected over the magnet pieces. With this setup, we have co-deposited thin film of $NiBi_3$ on the substrates. These films were further used for nanowire fabrication.

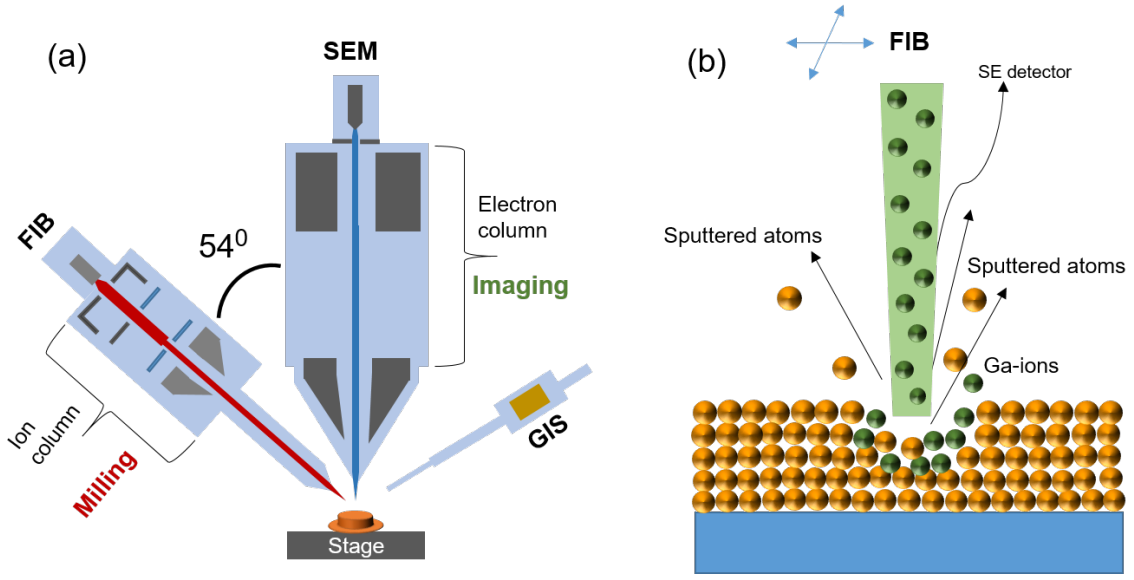

Figure 4.2: (a) Schematic of the crossbeam system showing 3 different components SEM column, FIB column, GIS system. (b) Schematic of the FIB milling procedure where Green balls are Ga-ions which implanted during the milling of any material.

4.2.2 Fabrication of Nanowires using Focused Ion Beam (FIB)

For the fabrication of nanowires, we have used the focused Ion Beam(FIB) of Zeiss Cross-beam 340. Figure-4.2(a) shows the schematic of the cross-beam system with various components such as scanning electron microscope (SEM) column, focused ion beam column (FIB) and gas injection system (GIS). However, in this work we have not used GIS. The working principle of SEM was discussed in detail in our previous chapter. The FIB column is connected along with the SEM column at an angle of 54° and source of this FIB system typically use liquid metal ion sources (LMIS), particularly gallium ion sources. Gallium metal is put in contact with a tungsten needle in a gallium LMIS, and heated gallium wets the tungsten and flows to the tip of the needle, where the opposing forces of surface tension and electric field form the gallium into a cusp-shaped tip known as a Taylor cone. The radius of tip is very small around 5nm. The gallium atoms are ionized and extraced from metal surface by field transmission while an electric field is applied(more than $1*10^8$ volts

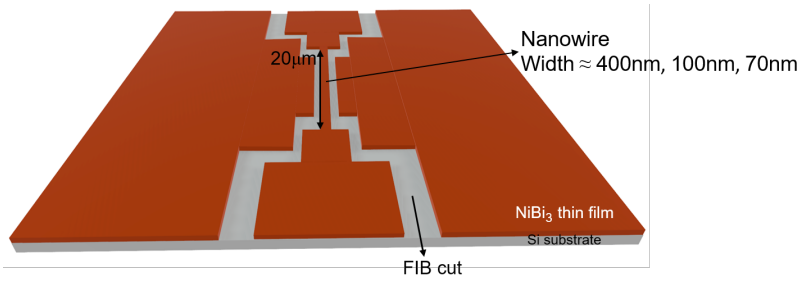

Figure 4.3: Schematic of a single Nanowire geometry fabricated on the thin film of $NiBi_3$ using FIB.

per centimetre). The source ions are then typically focused onto the sample by electrostatic lenses connected inside the FIB column after being accelerated to an energy of 1-50 kilo electronvolts (0.16-8.01 fJ). In our case, the maximum voltage achieved by the FIB Ga-ion system is 30kV. A finely focused ion beam is utilized in FIB systems. This beam can be operated at low beam currents for imaging or at high beam currents for site-specific sputtering or milling. In Figure-4.2 (b), we have shown the schematic of milling process with the help of FIB source. Here it can be seen that when Ga-ion interacts with the surface of sample, the atoms knocked out or sputtered out of the surface because of highly energetic galium ions which leaves the surface as either secondary ions (i+ or i−) or neutral atoms (n0). Secondary electrons (e) are also produced by the original beam. The signal from the sputtered ions or secondary electrons is gathered to create an image while the primary beam rasters across the sample surface. This is a basic idea on FIB milling technique, using this we have fabricated some nanowires on the thin $NiBi_3$ films. Nanowires of 3 different widths (keeping length fixed as 20μm) such as 400nm, 100nm, 70nm were fabricated on the thin film of co-deposited $NiBi_3$ samples, as shown by the schematic of Figure-4.3, the nanowire was isolated from the thin film in sequentially decreasing widths. The steps from the wider region to the narrower region ensure lesser heat generation when applying a high-bias current. Here the grey region is nothing but the substrate after the milling process. The nanowire was fabricated in 2 steps: in the 1st step the nanowire with an edge was isolated

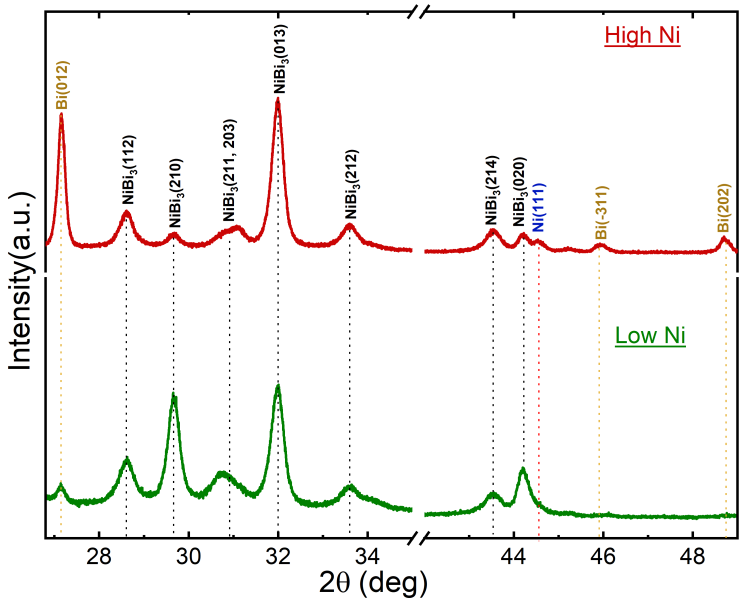

Figure 4.4: Comparison of Glancing angle X-ray diffraction pattern for the two samples deposited with and without magnetized mesh. The RED XRD plot is for High Ni and Green curve is for low Ni.

at a low FIB current of 30kV, 50pA to avoid gallium poisoning on the nanowire and in the 2nd step the wider regions with step were fabricated. The dimension of the contact pad area is 400*350μm, so a high FIB current of 30kV, 1.5nA was used for the milling process. The time duration for milling the nanowire region was almost 10sec whereas the time duration for the contact pad region was almost 3min. To study the effect of magnetic impurity on the phase slip fluctuations, we have chosen 2 thin films: (1) Co-deposited without using the magnetized mesh, (2) co-deposited with using 6 magnets.

4.2.3 X-ray diffraction measurement of thin film of $NiBi_3$

As discussed above in the experimental section, we aim to study the effect of magnetic concentration. It is necessary to do a background check for the magnetic concentration, which is Nickel here. For this purpose, we have performed X-ray diffraction measurements on the thin $NiBi_3$ films for high Nickel and low Nickel samples. Figure-4.4 shows the XRD

plot for these two samples; we have named the samples High Ni and low Ni, which will be used in further discussions. In both cases, plenty of $NiBi_3$ peaks were present matching with the JCPDS database no:65-0088, and the highest intensity peak of Bismuth (0 1 2) was also observed. We note that the (2 1 0) peak of $NiBi_3$ is highly prominent in the low Ni sample. The intensity of the second highest peak of $NiBi_3$ (0 1 3) was fund to be slightly decreased in the low Ni sample compared to the high Ni sample. Other than this, a most crucial point to be noted here is that the Nickel (1 1 1) peak is prominent in the high Ni sample but is absent in the low Ni sample. This is clear evidence of the intended variation in nickel concentration. The $NiBi_3$ plane (0 2 0), close to the Nickel peak has been enhanced in the low Nickel sample. In the low Ni sample, there was no signature of Nickel in XRD measurement possibly due to minimal amount of Nickel concentration. So For further clarification, we have performed resistance(R) vs temperature(T) measurement on the prepared nanowire, which is discussed in the later section.

4.3 Phase slip in the resistive state of $NiBi_3$ nanowires

On the prepared nanowires, we conducted transport measurements. Resistance vs temperature measurement for studying the phase slip fluctuation, current vs voltage for background measurement of these nanowires.

4.3.1 Current vs Voltage characteristics

We present zero field current vs voltage characteristic of the high-Ni nanowire in Figure-4.5 for all 3 widths at 2K. In the blue curve, the superconducting state (zero voltage) is very well defined up to 113μA current above which the superconducting state is jump to normal state with finite voltage response. Similar behaviour is observed for the 100nm nanowire (Red curve) also but with an increase in critical current. The IV curve was, however different for 60nm nanowire. The 60nm nanowire was very thin and appeared granular type. Here

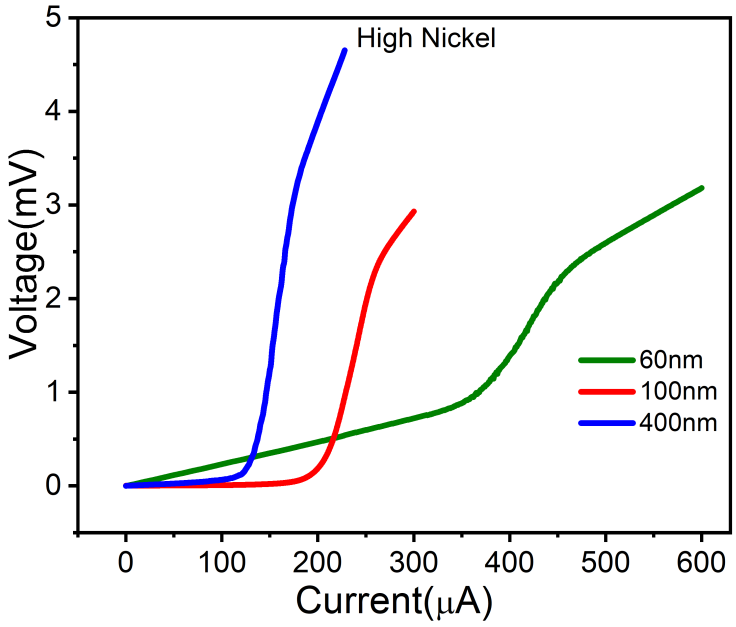

Figure 4.5: Current (I) vs Voltage (V) characteristics of high Nickel sample for all 3 width of nanowires.

in the green curve, the superconducting state is poorly defined with a linearly increasing voltage up to 339μA above which the nanowire looses its superconducting state completely at 469μA. The increase in critical current may be due to pinning of self-field vortices at the granular spots along the width of nanowire. The increase in the critical current can be explained below. According to the discussion in the literature[132], if width of the nanowire is such a way that $\xi < W < \lambda_{eff}$, then the formation of phase slips lines (PSLs) can be more pronounced than the phase slip centres (PSCs). These PSLs can act as extended pinning centres compared to the PSCs and these pinning centres can hold the self-field vortices produced due to the applied current. From the calculation, it is known that in case of $NiBi_3$, the coherence length ξ = 11nm and effective penetration depth λ_{eff} = 100nm. In case of narrower wires with width of 100nm and 60nm, the condition for formation of PSLs is satisfied. This leads to the fact that the extended pinning centres hold the self-field vortices gives rise to increase in the critical current compared to the wider nanowire (400nm). For

this reason the 60nm nanowire did not attain a fully superconducting state but remained in a resistive state. In Figure-4.5 it is observed that the critical current increases with the decreasing width of nanowires. The motive behind measuring *IV* characteristics here was to observe any steps like features that are typical in current carrying thin superconducting nanowires [140]. However, the IV curves did not exhibit any step-like features, which may be attributed to the factors explained by Ivlev et al. [140], specifically, the considerable length of the nanowire (20μm). As the length of the sample increases, the reduction in the electron mean free path induces multiple scattering effects. Consequently, this results in a continuous increment in voltage, instead discrete finite steps in IVCs, leading to a diminution in the clarity of the steps and a smoothing of the curve. Additionally, another contributing factor is the substantial thickness of the film, which measures 100nm. This thickness, in turn, mitigates the effect of phase slip along the thickness of the film.

4.3.2 Study of Phase slip in the resistive state

To study phase slip in $NiBi_3$ nanowires, current dependence resistance(R) vs temperature(T) measurements were performed. In Figure-4.6, we present *RT* plots of all 3 different widths of nanowires (400nm, 100nm, 60nm) corresponding to low Ni and high Ni samples. The first transition in the *RT* curve near the normal state shows the superconducting behavior of the contact pads, whereas the transition below $0.9T_c$ corresponds to the nanowire becoming superconducting. It can be observed that there are finite resistance tails at low temperatures (much below T_c). With increasing bias currents, the resistance at the lowest available temperature 1.8K ($0.4T_c$) increases and subsequently collapses to a single value at sufficiently high bias currents. Typically, the behavior of a one-dimensional superconductor is analogous to the motion of a particle in a ”washboard-like” potential [141]. The increase in effective resistance can be understood in terms of the change in the slope of washboard

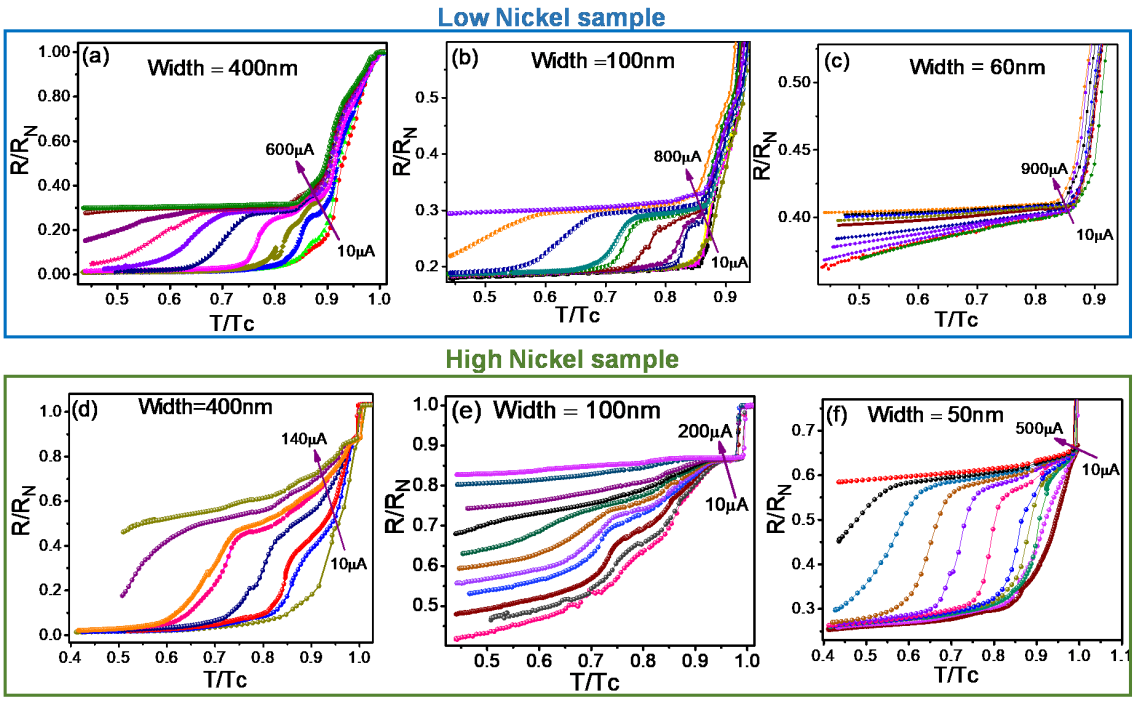

Figure 4.6: Normalized resistance *(R/R$_N$)* vs normalized temperature *(T/T$_c$)* curve for low Nickel and high Nickel samples respectively.

potential as the average slope of washboard potential is proportional to the current [141]:

$$\Delta F_I = \pm hI/2e \tag{4.2}$$

where ΔF_I is the difference in free energy between two adjacent minima, e is the electronic charge, and I is the bias current. As the bias current increases, so does the difference between the washboard potential minima, implying an increase in the subsequent potential barriers, resulting in an increase in effective resistance. These are the macroscopic quantum phenomena and the fluctuation due to these phenomena is also termed phase slip fluctuation [142]. Due to such phase slip fluctuation finite resistance in RT is typically observed in superconducting nanowires and [128]. The phase slip term explains the phase of Cooper pairs slipping by a multiple of 2π [140] at several random points in any superconducting nanowires. During a phase slip event, the order parameter fluctuates, momentarily creating a normal region in the nanowire. The time average of several such events adds finite

resistance to the superconducting state. Depending on the temperature regime, phase slip process is divided into two categories: 1) Thermal phase slip [143, 144], 2) Quantum phase slip [145, 127, 141, 146, 147]. The activation temperature regime for the thermal phase slip is near T_c [143, 144], whereas that for the Quantum phase slip is well below $T_c \sim 0.7T_c$ [127, 133]. From Fig-4.6 it can be seen that the finite resistance tails appear at low temperatures much below T_c, which may be associated with the quantum phase slip phenomena. In order to verify this possibility, we have fitted our experimental curves with the theoretical model of phase slip-induced resistive state which is explained below.

4.3.2.1 Fitting with the theoretical Model

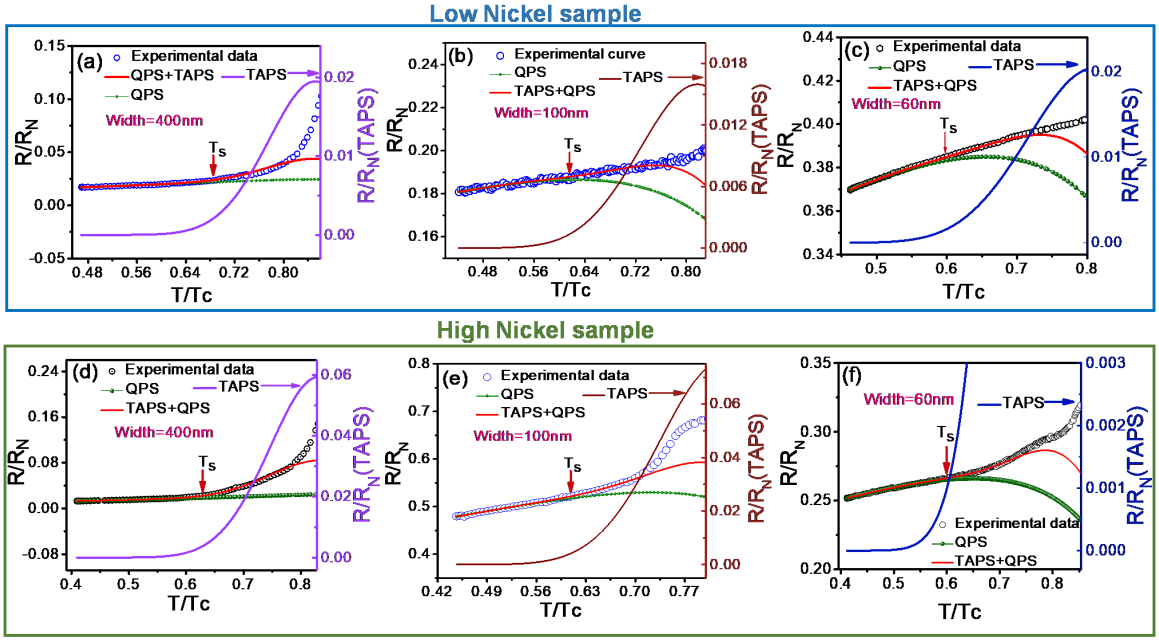

Figure 4.7: Low bias RT fitting curves for all widths of nanowires for low Nickel(a, b, c) and High Nickel(d, e, f) sample.

At sufficiently low temperatures phase slip should arise from quantum fluctuation of the order parameter. Observation of such quantum phase slips(QPS) was first reported by Giordano [145]. The measured resistance curves below T_c can be fitted as the sum of two

terms due to TAPS and QPS [148] in the form of the equation (4.3). The TAPS model explains the *RT* behavior only very close to T_c whereas QPS model explains well below T_c. There is an optimum temperature value below $0.718T_c$ below which the Giordano model predicts a higher QPS rate compared to the TAPS rate. Also in reference [133] by Cecile et al., a QPS-like decay was experimentally observed below 0.7 of T_c. We have fitted the *RT* curves for both samples using the normalized form as in equation (4.3)

$$\begin{aligned} R &= R_{\text{TAPS}} + R_{\text{QPS}} \\ &= \frac{\pi\hbar^2\Omega_{\text{TAPS}}}{2e^2kT}\exp\left(-\frac{\Delta F_{\text{TAPS}}}{kT}\right) + \frac{\pi\hbar^2\Omega_{\text{QPS}}}{2e^2\left(\frac{\hbar}{\tau_{\text{GL}}}\right)}\exp\left(-\frac{\Delta F_{\text{QPS}}\tau_{\text{GL}}}{\hbar}\right) \end{aligned} \tag{4.3}$$

The first and second term of the right hand side of equation 4.3 corresponds to the thermally activated phase slip(TAPS) and quantum phase slip(QPS) respectively. Here, $\Omega_{TAPS(QPS)}$= *(L/ξ)*$(\Delta F_{TAPS(QPS)}/kT)^{1/2}$ is the attempt frequency [95], ΔF_{TAPS} and ΔF_{QPS} are TAPS and QPS energy barriers. τ_{GL}= $\pi\hbar/8k(T_c\text{-}T)$ is the G-L relaxation time also called tunneling time of a QPS [95]. The equation 4.3 can be written in terms of normalized resistance by $r=R/R_N$ and normalized temperature $t=T/T_c$ [149] and as,

$$\begin{aligned} r = \frac{R}{R_N} &= at^{-3/2}(1-t)^{9/4}\exp\left(\frac{-b(1-t)^{3/2}}{t}\right) \\ &+ c(1-t)^{3/4}\exp\left(-d(1-t)^{1/2}\right) \end{aligned} \tag{4.4}$$

With a, b, c, and d serving as the four dimensionless parameters, we fit our *RT* data using equation 4.4. We performed the fitting until the adjusted R-square=0.99 has been obtained. In Figure-4.7, we have shown the fitting curves with the *RT* experimental data for low-bias currents. Here in all the curves, the right-hand side axis represents the TAPS theoretical plotted curve. The red solid line represents the fit of the sum of TAPS and QPS, while the green solid dots depict the QPS fit. In all graphs, we've marked a point *Ts* where the QPS plot deviates from the experimental data. This *Ts* is called the QPS threshold temperature, signifying the point where QPS begins to decay, and TAPS takes over the transition. We've

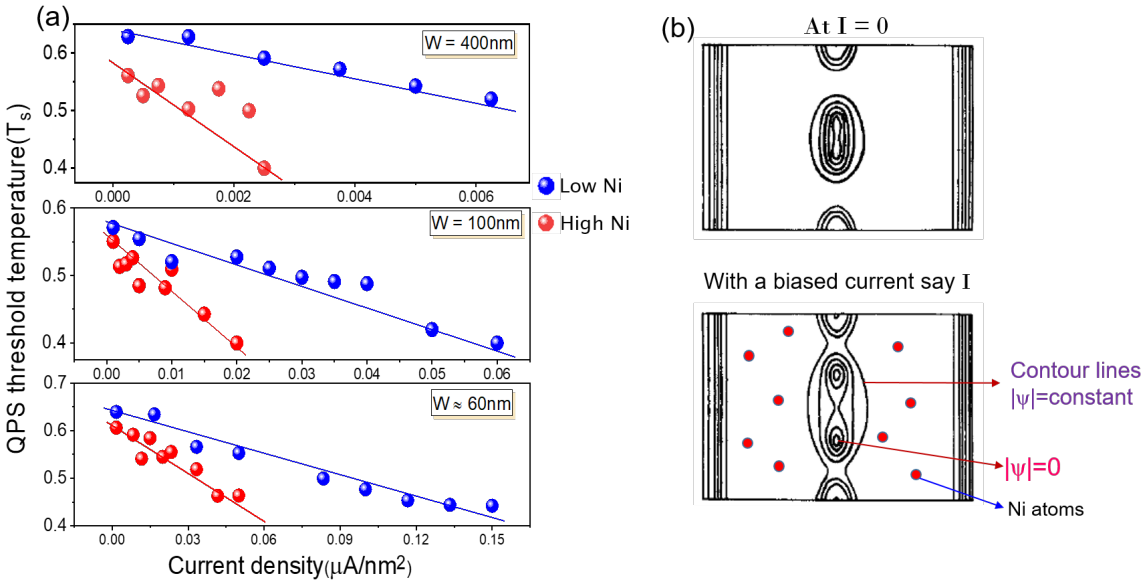

Figure 4.8: (a) QPS threshold temperature(Ts) vs current density(J) for all samples.Blue dots for low Ni sample, Red dots for high Ni sample. (b) Representative picture adapted from literature by explaining our observation.

noted and plotted the *Ts* values from these fitted curves at different currents, allowing for a straightforward comparison between low Ni and high Ni samples.

4.3.2.2 Discussion on the QPS threshold temperature Ts

Figure-4.8(a) shows the QPS threshold temperature (Ts) plotted against the current density for all nanowires, illustrating a comparison between the low Ni and high Ni samples. Here few things can be noticed: (i) *Ts* is higher in nanowires prepared from low Ni sample compared to the high Ni sample, (ii) QPS sustains up to higher current densities in the low Ni sample and (iii) with decreasing widths of the nanowires *Ts* sustains up to higher current density. We discuss these observations in the light of the theoretical model on kinematic vortices discussed in the literature by Andronov et al. [132].

Andronov et al., have proposed, that there could be three regimes of widths of a superconducting stripe for being in the resistive states:(a) Widths substantially larger than the

adequate magnetic penetration depth λ_{eff} ($\lambda_{\text{eff}} = \lambda^2/d$), (b) widths below the coherence length ξ, (c) intermediate case, the width of a channel lies between coherence length ξ and penetration depth λ. In the case of $W > \lambda_{eff}$, the resistive states result from the movement of Abrikosov vortices; in the case of narrow channels ($W < \xi$), resistive states are due to the pair breaking process which produces phase slip centres (PSC) but in case of $\xi < W < \lambda_{eff}$, the order parameter and dynamic of current is 2-dimensional; on the other-hand width is too small for Abrikosov vortices. In this case, the resistive state appears due to kinematic vortices. These kinematic vortices (breaking of PSL's) are nothing but the moving PSC's across the channel. A representative contour plot in Fig-4.8(b) is adapted from Andronov et al. [132] for the explanation of results in our case. Here the parallel lines represent $|\psi|$=constant whereas the curved contour lines at the middle enclose the isolated vortex core with $|\psi|$=0, where ψ is the superconducting order parameter wave function. This is a typical situation at bias current I=0, but in the presence of finite current value, these vortices start to move along the transverse to the length of the superconducting channel. In our case, the high Ni sample exhibits a substantial amount of Nickel, as indicated by the drawn red dots in the bottom figure. Given that kinematic vortices move more rapidly with the presence of prior phase slip centers (PSCs) or prior phase slip lines (PSLs), they are expected to propagate much faster in the high Ni impurity environment, facilitated by the presence of Ni impurities. This leads to a pronounced increase in resistance at low temperatures in the high Ni sample compared to the low Ni sample. In general, phase slip lines(PSLs) are the 2D analogous of phase slip centers(PSCs) where the oscillations of order parameter may not necessarily be uniform as in the case of PSC [129, 150, 151]. These oscillations take the shape of waves that spread across the sample, bearing the order parameter singularities. These waves are also known as kinematic vortices (rapidly moving vortices), which were actually observed experimentally by Sivakov et al. [129]. Subsequently, due to the accelerated movement of vortices and the reasons discussed above, the size of phase slip centers

(PSCs) increases, accumulating nearby Ni impurities. This accumulation contributes to an increase in effective resistance, ultimately leading to the decay of the superconducting transition temperature (*Ts*) in the high Ni sample. However here we could not clarify about the occurrence of kinematic vortices as vortex-antivortex pair [150] or not. But with respect to the dimensions as discussed in the literature we can make a qualitative argument that the occurrence of phase slip activities as well as the results of *Ts* can be due to movement of Kinematic vortices.

4.3.3 Study of Magneto-resistance in $NiBi_3$ nanowires

$NiBi_3$ has been identified as a disordered superconducting system, as evidenced by observations from FESEM images detailed in Chapter 2. The transport characteristics of disordered superconducting systems are typically expounded through the lens of a coupled network of Josephson junctions. In this framework, individual grains possessing well-defined superconducting order parameters establish coupling across grain boundaries. The work of Al'stuler and Spivak [138] has elucidated that mesoscopic fluctuations in current can exert significant influence on transport within disordered SNS (superconductor-normal metal-superconductor) junctions, particularly when the current across the junction is suppressed. This scenario is realized when superconducting grains are separated by inter-grain regions of a magnetic nature. Further insights into the consequences of fluctuations in the sign and amplitude of superfluid density on the average superconducting properties of an ensemble of superconducting grains have been provided by Kivelson and Spivak [152]. Their analysis reveals that under such conditions, magnetoresistance can exhibit sub-harmonic Aharanov-Bohm type oscillations and may result in negative magnetoresistance. To experimentally validate these hypotheses, we present the results of temperature-dependent magnetoresistance measurements conducted on a superconducting $NiBi_3$ nanowire. This nanowire was fabricated using focused ion beam patterning from a granular $NiBi_3$ film.

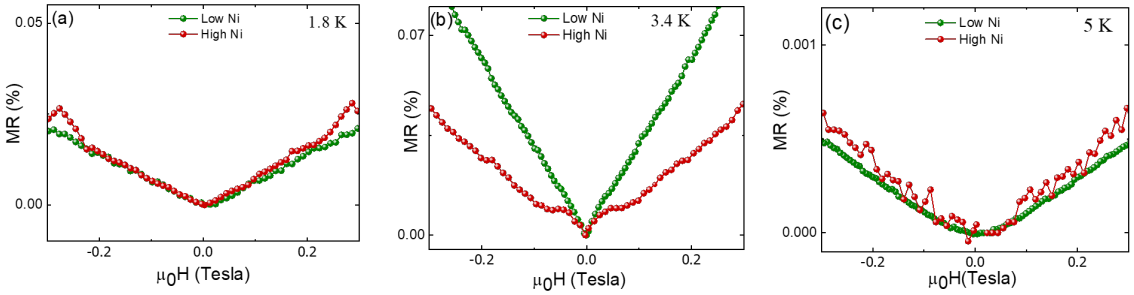

Figure 4.9: Magneto-resistance plot for the 100nm wide nanowire at temperatures (a) 1.8K, (b)3.4K and (c)5K compared between low Ni and high Ni smaple.

4.3.3.1 Temperature dependent Magneto-resistance comparison

In this section, we delve into the low-field magnetoresistance exhibited by both the high-Ni and low-Ni samples as a function of temperature. The measurements were conducted with a current of 70 μA within a field range spanning approximately 2800 Oe, encompassing temperatures from 1.8 K to 5 K. Our focus in this investigation lies on the resistive state of the nanowire, where the current density assumes significance within the context of phase slip phenomena. As the current density increases, a higher frequency of phase slip events occurs, potentially driving the nanowire into a fully normal state [133]. Consequently, magnetic resistance (*MR*) measurements at elevated current densities were excluded to mitigate potential heating effects. Figure-4.9 shows the *MR* plot at three different temperatures 1.8K, 3.4K and 5K. The observation that the low-field magnetic resistance (*MR*) at 1.8 K nearly overlaps as shown in Figure 4.9(a), suggests that the nanowires experience comparable field-dependent pair-breaking orbital effects. The *MR* plot above the superconducting T_c at 5K in fig-4.9(c) shows no significant change with respect to field and very small change in magneto-resistance for both the nanowires. This indicates that there is no effect of magnetic impurity on the change in magneto-resistance response. But a peculiar behaviour in *MR* occurs at 3.4K in case of high Ni sample as shown in fig-4.9(b). Here the change in magneto-resistance for low Ni sample is very sharp, double the change in low Ni sam-

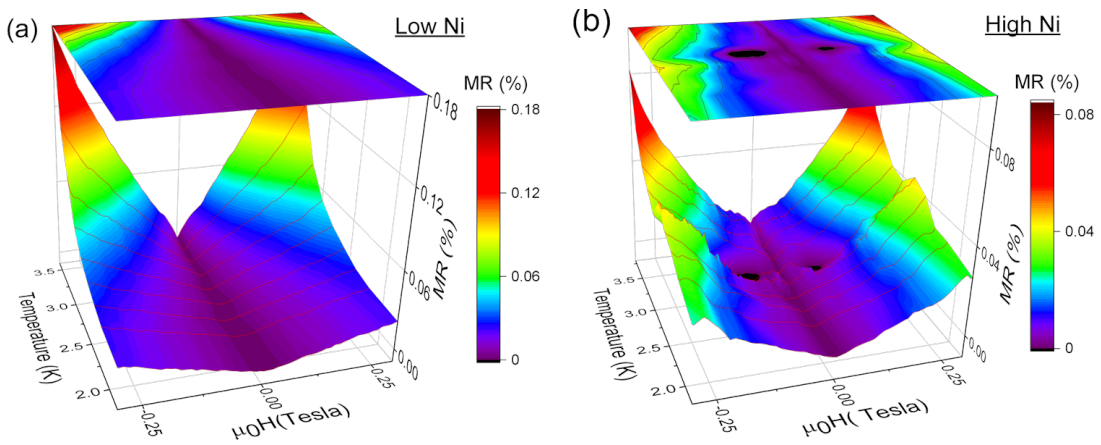

Figure 4.10: The 3D surface map and the corresponding contour maps for the MR measurements performed at various temperatures are shown in panels (a) and (b) for the low-Ni and high-Ni nanowires. The high-Ni sample shows a clear negative *MR* region, marked black in the color map in panel (a), unlike the smooth temperature dependence of *MR* for the low-Ni nanowire shown in panel (b)

ple and linear with magnetic field whereas for high Ni sample, the *MR* is non-monotonic. Also, in the *MR* plot of high Ni sample, oscillatory behaviour has been observed. As we have discussed above the resistive behaviour of nanowires depend upon the bias currents which affect the fraction of phase slips in the nanowire, which can substantially transform the nanowire into normal state. So in order to rule out the possibility of heating effects on change in magneto-resistance, we have measured the RH at 70uA.

For clarity, we have compiled the *MR* data measured at several temperatures in a 3D-surface map shown in Figure-4.10(a) for the low Ni sample, Fig-4.10(b) for the high Ni sample respectively. The color scale represents the *MR* percentage in these figures with corresponding 2D surface projections. It is apparent that the *MR* response of low Ni sample is monotonic with monotonic dependence on magnetic field and temperature. But in the case of a high Ni sample, a clear non-monotonic oscillatory behavior is observed in *MR*. Other than the oscillatory behavior, a negative magneto-resistance was observed in a certain temperature regime shown black deep in Figure-4.10(b).

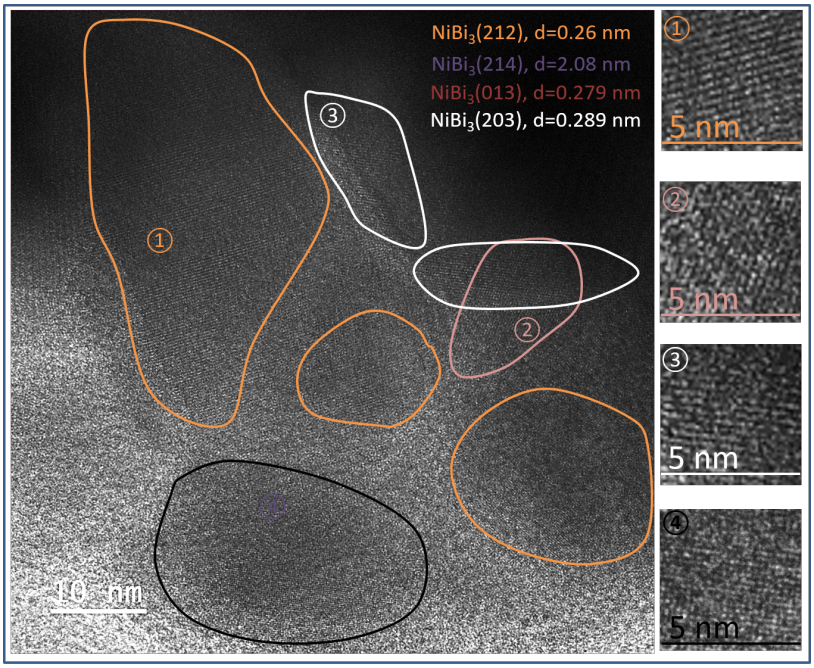

Figure 4.11: A representative high-resolution transmission electron micrograph of the $NiBi_3$ film showing the dispersion of randomly oriented grains. Right panel: zoomed view of the corresponding $NiBi_3$ planes marked by different colours.

Several physical phenomena can give rise to negative magneto-resistance in superconducting nanowires. For example, Xiong et al. [153], have experimentally verified the negative magneto-resistance (*nMR*) in Pb amorphous wires measured near to T_c where they have explained the *nMR* due to the non-equilibrium charge imbalance effect of normal-superconductor interface. Here normal-superconductor interface is nothing but the interface around the phase-slip centre where the cooper pair breaks down at the center. The center is a normal region surrounded by the circulating screening current where the Andreev reflection process introduces charge imbalance over a length scale of λ_Q. inversely proportional to the normal state resistivity of the materials [154]. Schmid et al., have shown that the application of a small magnetic field can decrease the λ_Q. Subsequently, the resistance of the phase slip process decreases as well as overall drop in the resistance is possible with an applied magnetic field [155]. Later research on NbN nanowires [156, 157] and InO nanowires

[158] also, interpreted the occurrence of large negative magneto-resistance(*nMR*) based on the above discussions. The explicit field dependence of the resistance of the phase slip center [154, 155], however, does not account for a non-monotonic temperature dependence of this effect. Therefore, this mechanism can be ruled out in the context of our data. Another possibility for the negative magneto-resistance in MoGe and Nb nanowires were proposed by Rogachev et al [159] which is due to stray field produced at the surface of nanowires. The pair breaking effects due to this stray magnetic field can cause a negative Magneto-resistance in the nanowires, but in this case the *nMR* appears at the zero magnetic field itself. $NiBi_3$ nanowires contain magnetic impurities which may be one of the reasons for not fitting with the explanation of *nMR* with the Rogachev et al. Other than this, there are two more reasons we can use to rule out this possibility: (i) *nMR* does not start at zero magnetic field and (ii) the *nMR* effect appears only in certain temperature range. Other reports suggest the observation of normal-state magnetic resistance (*nMR*) in Zn nanowires through experimental work conducted by Tian et al. [160]. Fu et al. [161] have provided theoretical explanations for this phenomenon, attributing it to a dissipative boundary effect associated with the contact pads. In this scenario, the field-induced suppression of superconductivity in the contact pads facilitates the dissipation of vortex-antivortex pairs from the nanowire, thereby promoting normal-state magnetic resistance. Similar way of explanation for the occurrence of *nMR* is also shown for NbN nanowires [156]. Another possibility of negative *MR* is reduced phase fluctuations due to field driven enhancement of the dissipative quasiparticle channel in nanowires explained by Chen et al. [162], where a monotonic temperature dependence is expected similar to the *nMR* response in Pb nanowires [153]. Our findings are again inconsistent with this explanations as we have a non-monotonic temperature dependence. In our $NiBi_3$ nanowires, the magnetic inter-grain regions serve as precursors for negative inter-grain currents, leading to fluctuations in the sign of the order parameter, consequently inducing negative magnetoresistance (*MR*). We present here the

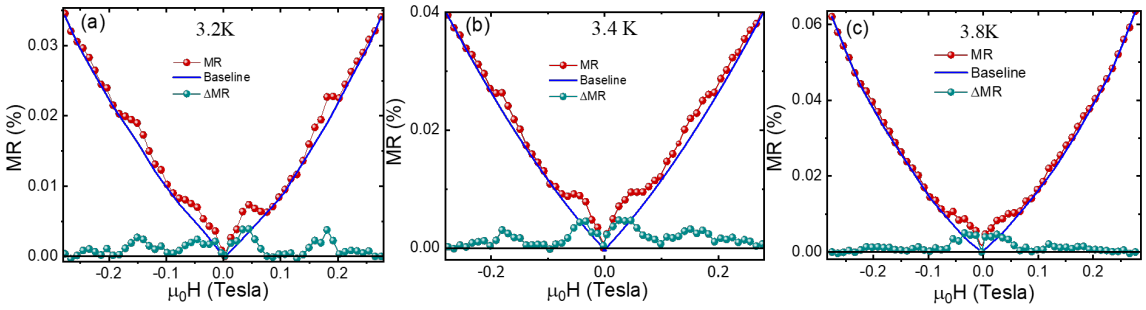

Figure 4.12: Magneto-resistance as a function of the applied magnetic field are shown at 3.2 K, 3.4 K, and 3.8K. The polynomial baseline in each case, subtracted from the respective *MR* data, are also shown in this figure as solid lines. After subtraction of the baseline, the resultant *ΔMR* shows clear symmetric oscillations.

HRTEM image of $NiBi_3$ film in Figure-4.11 , which shows the granular structure of thin films with well-defined grain boundaries. The different colors correspond to the different orientations of several $NiBi_3$ planes shown at the right panel for (2 1 2), (0 1 3), (2 1 4), (2 0 3). It can be observed that the planes are not deformed, so the magnetic impurities are not on top of $NiBi_3$ grains and must stay at the inter-grain regions. So the coupling between $NiBi_3$ superconducting grains happens via Ni ferromagnetic impurity here. The coupling between two superconducting regions separated by a ferromagnetic region can be 0-type or π-type depending on the spatial variation between those 2 SCs [163, 164]. This is the only situation that can give rise to the random 0, π coupling between 2 SCs.

Another important aspect of *MR* graph in Fig-4.9(b) is oscillations in high-Ni sample. For comparison at different temperatures and oscillation periods we have shown a smooth polynomial baseline corrected graph in Figure-4.12. Although the oscillations are faint, two clear oscillations are visible in the ΔMR curve, as indicated by the light blue color. The oscillations in *ΔMR* is visible at all temperatures but is more pronounced at 3.4K. Oscillations in *ΔMR* can be due to different reasons such as incoherent penetration of vortex bundles into the nanowires [165] via flux matching effects [166]. In that scenario, the period of the oscillations should be a function of magnetic field, unlike our data (Fig. 4.9

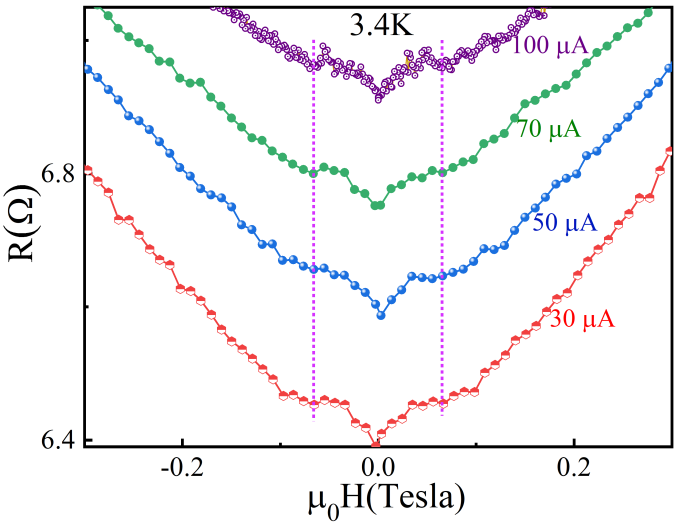

Figure 4.13: Current dependence of magnetoresistance for high-Ni nanowire measured at 3.4 K. *MR* oscillations do not seem to depend on the bias current, ruling out the possibility of flux pinning-related *MR* oscillations, as discussed in the text.

and 4.10). Periodic magnetoresistance (*MR*) can arise from matching effects that result from equalizing the density of the pinning force and the density of vortices [167, 168, 169]. Gurevich et al. [169] have demonstrated that this effect is significantly dependent on the applied current. However, the current-dependent *MR* plot depicted in Figure-4.13 provides evidence that the oscillations in the present case are independent of the applied current. This measurement, conducted at 3.4 K under various bias currents, reveals that both the depth of the minima and the period of the oscillations remain constant across different current levels. Therefore, matching effects can be ruled out in our results. The oscillatory *MR* in the high Ni sample may arise from granularity, as reported in granular NbN nanowires [170], granular Sn nanowires [171], and amorphous InO nanowires [172], where the oscillation in *MR* is caused by flux quantization effects through an effective phase-coherent loop created by the current distribution. A similar effect may be the origin of *MR* oscillations in high-Ni $NiBi_3$. The only unified model that describes both the *nMR* and oscillation in *MR* is the Kivelson and Spivak model [152]. Kivelson and Spivak have shown that large

fluctuations in amplitude and sign of the order parameter in a superconducting system can naturally lead to both of these effects. Although fluctuations in the amplitude of the order parameter can be expected in granular superconductors, no clear scope for a fluctuation in the sign of the order parameter has been identified in the earlier reported nanowire systems [156, 157, 153, 171]. The $NiBi_3$ system is a unique system that provides ample scope for the fluctuations of sign and magnitude of cooper pair order parameters due to the magnetic inter grains. The coupling between two superconducting regions separated by a ferromagnetic region can be 0-type or π-type depending on the spatial variation between those two SCs [163, 164]. Here in $NiBi_3$ sample, the HRTEM (Fig-4.11) image shows the granular textures, each grain is $NiBi_3$ superconductors, and in the case of high-Ni sample, the grains can be assumed to be separated by magnetic Ni impurities. This is the only situation that can give rise to the random 0, π coupling between 2 SCs. Hence we understood the occurrence of *nMR* and oscillation are due to above discussed reasons. So in this chapter, we studied the transport in $NiBi_3$ nanowires which we have discussed.

4.4 Summary

In this chapter, we have explored the transport properties of six $NiBi_3$ nanowires fabricated on two distinct thin films with varying concentrations of magnetic impurities. The conducted transport measurements encompassed current vs voltage characteristics, resistance vs temperature profiles, and resistance vs magnetic-field responses. Comparisons were made between the current-voltage characteristics of all nanowires for the high Ni sample and the low Ni samples, revealing a resistive nature in the nanowires. The resistance-versus-temperature curve provided insights into phase slip activities within the nanowires, with an observed increase in the fraction of phase slip events as the bias current was elevated. Theoretical fitting was performed for two phase slip phenomena—Thermal phase slip and

Quantum phase slip—across all room temperature curves. Analysis of these fittings indicated that the threshold temperature for Quantum Phase Slip (QPS) is higher in the low Ni sample compared to the high Ni sample. Magneto-resistance measurements unveiled the presence of oscillatory behavior and normal-state magnetic resistance (*nMR*) in $NiBi_3$ nanowires, particularly in the high Ni sample. This observation was attributed to the existence of magnetic Ni impurities at the inter-grain boundary regions.

Chapter 5

Planar Josephson Junction from $NiBi_3$ thin film via focused Ga ion beam irradiation

5.1 Introduction

Josephson junctions represent superconducting devices in which two superconducting electrodes are separated by a non-superconducting region, giving rise to a current-phase relation of the form $I = I_0 * Sin\Phi$. [173] Here, Φ denotes the phase difference between the two superconducting electrodes. When operating in the tunneling limit of the barriers, commonly referred to as superconductor-insulator-superconductor (SIS) junctions, these devices exhibit a characteristic hysteretic current-voltage response [174, 175]. In contrast, when functioning in the diffusive limit, they display a non-hysteretic current-voltage behavior, and this category is often termed SNS junctions [176, 177]. While SIS junctions are typically constructed in the vertical geometry [178] due to the substantial energy barrier width of the insulating layer, SNS junctions offer more flexibility in terms of device architecture. This flexibility arises from the fact that the geometrical gap between the superconducting electrodes in SNS junctions can be on the order of tens of nanometers, unlike SIS junctions where the geometrical gap cannot exceed a few nanometers. Consequently, in the existing literature [179, 180], SNS junctions have been fabricated both in the vertical geometry and in planar geometries such as microbridge and wider planar junctions.

Within the specific focus of this thesis on $NiBi_3$, the feasibility of vertical junctions was limited primarily by the comparatively larger surface roughness exhibited by the co-evaporated $NiBi_3$ films in comparison to other metallic superconductors. The pronounced

roughness inherent in the $NiBi_3$ film results from the natural inclination of $NiBi_3$ to develop vertical nanowire-like structures, a phenomenon elucidated in chapter-2 of this thesis. The high roughness prevents the realization of vertical junctions in multilayer structures, as it leads to shorting through the layers, eliminating any possibility of obtaining a vertical junction. Consequently, we opted for the planar junction geometry for $NiBi_3$, a decision detailed in chapter-4. The microscopic structure of the $NiBi_3$ film is characterized by nanoscale superconducting grains separated by boundaries, and Josephson coupling across these boundaries gives rise to macroscopic superconductivity in these films. The study focuses on the intriguing scenario of Josephson coupling between two $NiBi_3$ electrodes, where a random network of Josephson couplings exists inside the electrodes. To create planar junctions from the co-evaporated $NiBi_3$, we employed a local irradiation technique to define a narrow barrier region. Initially, the film was narrowed down to tracks of a few micrometers width using optical lithography and chemical etching. Subsequently, narrower constrictions were generated by exposing a region of the constrictions to 5kV Ga ions through the focused ion beam system. At these energies, the Ga ions were implanted within a depth of approximately 15nm, suppressing superconductivity in the exposed region. The width of the exposed region, set at around 100nm, serves as the Josephson barrier width, demonstrating that $NiBi_3$ junctions exhibit Josephson behavior only when narrowed down to nanowire dimensions.

5.2 Experimental details:

Realizing Josephson planar junctions from $NiBi_3$ thin films required optical lithography patterning of co-evaporated thin films and extensive focused ion beam patterning. Finally transport in these devices was measured at 1.8K. In this section we explain the details of the experimental methods.

5.2.1 Thin film deposition

At ambient temperature, a thin film of $NiBi_3$ was co-deposited in a system combining both E-beam and thermal evaporation with a base pressure of 1.2×10^{-7}mbar using high purity (99.99%) Nickel wires and Bismuth ingots as the target materials. The detailed experimental procedure of co-deposition was explained in chapter-2. The thickness of the film was confirmed using X-ray reflectivity (XRR) measurement as well as using a Step pro-filer to be around 50nm. The reason behind this choice of thickness was to ensure Ga-ion induced suppression of T_c in the Josephson barrier region. For thicker films, local suppression of superconductivity may be difficult to achieve and hence defining a Josephson barrier may not be feasible. For further fabrication process, we have followed the lithography process for patterning the thin film of $NiBi_3$.

5.2.2 UV Lithographic patterning

To get the desired pattern on the co-deposited thin film sample, several steps were followed which are described in this section. A schematic of the standard procedure for positive lithography using the positive photo mask is presented in Figure-5.1. In the first step, the thin film was spin-coated at 4000rpm for 30sec with the thick positive photo-resist mp-1205. The sample was dried on a hot plate at a temperature of 75°C. After cooling, the first layer of photolithography was performed to define the contact pads and the μm scale tracks of $NiBi_3$. This was done using positive photo mask, which protects the desired area under the lithography pattern and exposes the remaining regions, as shown in the Figure-(5.1). The open space was exposed to UV light for 10 seconds while the film underneath the mask was protected. A typical NaOH developer: DI water solution (1:1) was used to develop the exposed region for 15 seconds. After developing the PR pattern the exposed, part of the thin film was removed using a diluted Nichrome etchant solution in the ratio with DI water(1:10)

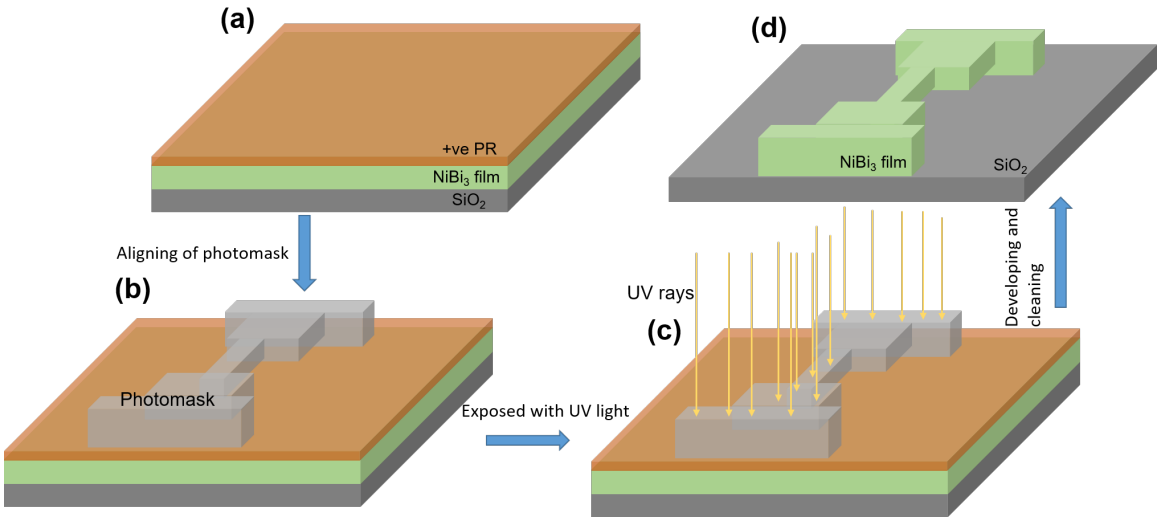

Figure 5.1: Schematic representation of UV lithography process for the positive lithography using both positive photo-resist and positive photo-mask.

for 20sec. After the chemical etching process, the sample was thoroughly cleaned with DI water and checked under the microscope to determine whether proper etching was done. In the last step, the sample was cleaned using acetone to remove the remaining photo-resist. As shown in the FESEM image of the final product of this stage, 5μm wide tracks were obtained along with attached contact pads of size 400 $\times$ 300 μm^2.

5.2.3 Nano-constriction using Focused Ion Beam (FIB)

Subsequent to the UV lithography step we patterned the nanoscale Ga-implanted Josephson barrier using FIB. Firstly the working voltage of the Ga beam was set to 5kV, 10pA current. The beam was then focused on the $NiBi_3$ film surface at a spot away from the area of interest. A narrow line of $\sim$ 100nm width was then drawn across the 5μm track, as shown in Figure-5.3. The beam voltage of 5kV was selected based on a calculation of the penetration depth of the Ga ions into $NiBi_3$, using the Transfer of Ions in Matter (TRIM) package [181]. Simulated ranges of Ga ion beam in $NiBi_3$ of several energies between 0.5kV to 30kV are shown in Figure-5.2. At 5kV, the overall range of implantation was found to be $\sim$ 15nm.

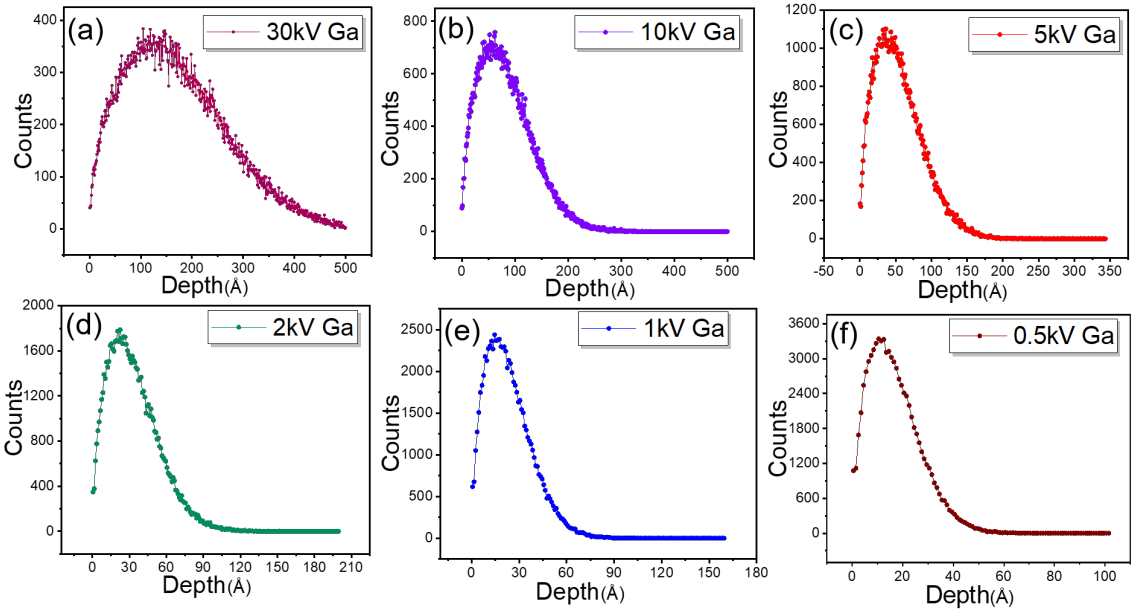

Figure 5.2: Simulated penetration depth of Galium into the $NiBi_3$ thin film at various voltages(a) 30kV, (b) 10kV, (c) 5kV, (d) 2kV, (e) 1kV, (f) 0.5kV using TRIM software.

Since the process of implantation, using a focused beam also significantly sputters out the $NiBi_3$ material, we found 5kV to be optimum in this case. At higher voltages, the sputtering rate becomes too high to control while at lower voltages the range of ions becomes low. Since the film thickness was $\sim$ 50nm, 5kV focused ions provide a good implantation range while allowing for some sputtering from the exposed area which defines the Josephson barrier. The depth of milling is discernible from the FESEM image shown in the Figure-5.3(b). After transport measurements of these implanted wide (5μm) tracks, they were further narrowed down by FIB milling at 30kV and 50pA. The geometry of this narrowed region is a 200nm nanowire as shown in Figure-5.3(c).

5.2.4 Transport measurements

We have performed electrical transport measurements such as Resistance(R) vs temperature(T), current(I) vs voltage(V), and voltage(V) vs magnetic field(H). An example of standard four-probe contact positions is shown in Figure 5.4(a) where V is the notation for

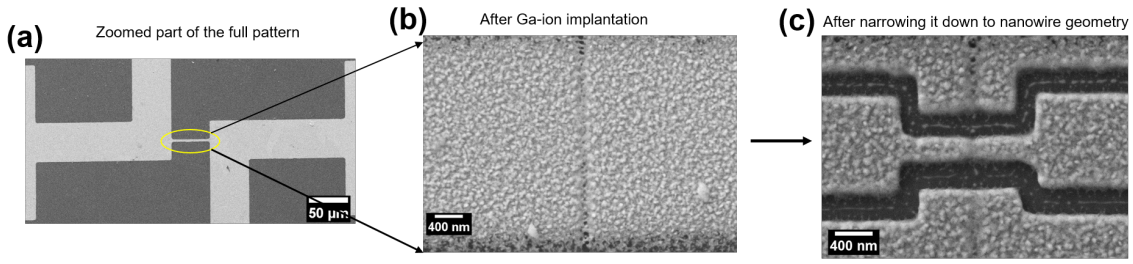

Figure 5.3: (a) FESEM image of the lithography pattern made on the co-deposited thin film. (b) An example of FESEM image of the wide track after a poisoned cut was made. (c) FESEM image of the same track after narrowed down to nanowire geometry.

voltage contacts for that particular spot and current contacts are across as shown. Similarly, the voltage and current contacts were made for other tracks. We have used Aluminium wire bonding to make contact with the sample holder used in DC electrical resistivity dipstick for the CRYOGENIC physical property measurement system. Measurements were performed at temperatures down to 1.8K. In the case of magnetic field dependence of junction voltage, the external field was applied perpendicular to the plane of the devices.

5.3 Results and discussion

As described in the experimental details section, we implemented Ga-implanted junctions in a nanowire planar geometry. In the context of nanowire geometry, the following sequence of measurements and fabrication procedures was executed. Initially, transport data for the pristine 5µm-wide track was acquired immediately after the etching of the tracks, preceding the Ga implantation. Subsequently, Ga implantation was performed to delineate a barrier region, following the previously described procedure. The transport response of the implanted wide junction was then recorded. After these measurements, the wide implanted track was further narrowed down to 200nm wires for subsequent transport measurements.

5.3.1 Transport measurements on Ga-implanted nanowire junctions

Figure-5.4 shows the SEM and transport results of 5μm wide $NiBi_3$ track before implantation and narrowing down. Figure-5.4(a) represents an SEM image of the sample where it is apparent that the film is granular, but the granular feature does not affect the Ga implantation procedure. Figure-5.4(b) shows the resistance(R) vs temperature(T) measurement for this sample at a bias current of 10μA. Here it can be seen that the T_c is around 3.8K, and there is a residual resistance value of 2Ω at 1.8K. The highly granular nature of $NiBi_3$ is responsible for the residual resistance. The $NiBi_3$ track with 5μm wide exhibits resistance, much like the $NiBi_3$ nanowires mentioned in Chapter 4, primarily due to phase slip activities. The track's resistive behavior in the RT curve can be attributed to its thickness of $\sim$ 50nm, which is a plausible explanation. Further evidence of phase slip activity is observed in the current (I) versus voltage (V) characteristic curve in Figure-5.4(c), measured at 1.8K. The distinct step-like patterns observed in the curve are also indicative of characteristic features associated with phase slip occurrences in any superconducting samples [133, 182]. Here we observe some similar step-like features in the **IV** curve, just above the superconducting critical current I_c. These steps can be described as discrete voltage increments that align with multiple instances of phase slip, wherein Cooper pairs locally transform into normal electrons. Figure 5.4(d) illustrates our measurements of voltage versus perpendicular magnetic field. It is evident from the graph that the voltage exhibits a linear relationship with the magnetic field typical for a superconductor. Our objective was to investigate the transport properties of the $NiBi_3$ tracks under the influence of Ga-implantation. In order to achieve this, conducting background measurements were essential. Therefore, Figure 5.4 presents the results of these background measurements conducted prior to the Ga-implantation procedure. Sequential measurements were conducted after each step of the fabrication process. Initially, the wide track was measured, and subsequently, in the following step, the same

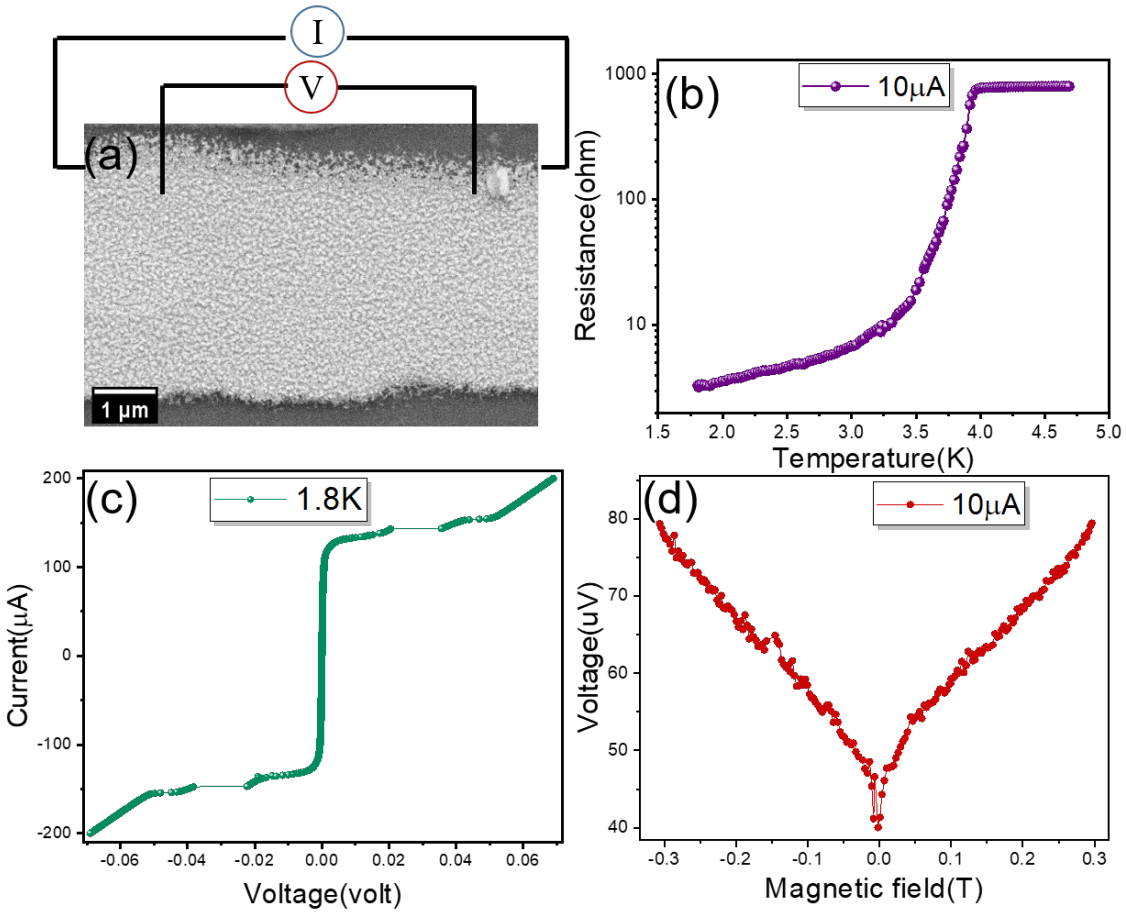

Figure 5.4: (a) SEM image of 5μm wide track of $NiBi_3$ thin film, (b) Resistance(R) vs temperature (T) measurement plot for this sample measured at 10μA bias current, (c) Current (I) vs voltage (V) plot for this sample measured at 1.8K, (d) Voltage (V) vs magnetic field (H) measurement plot.

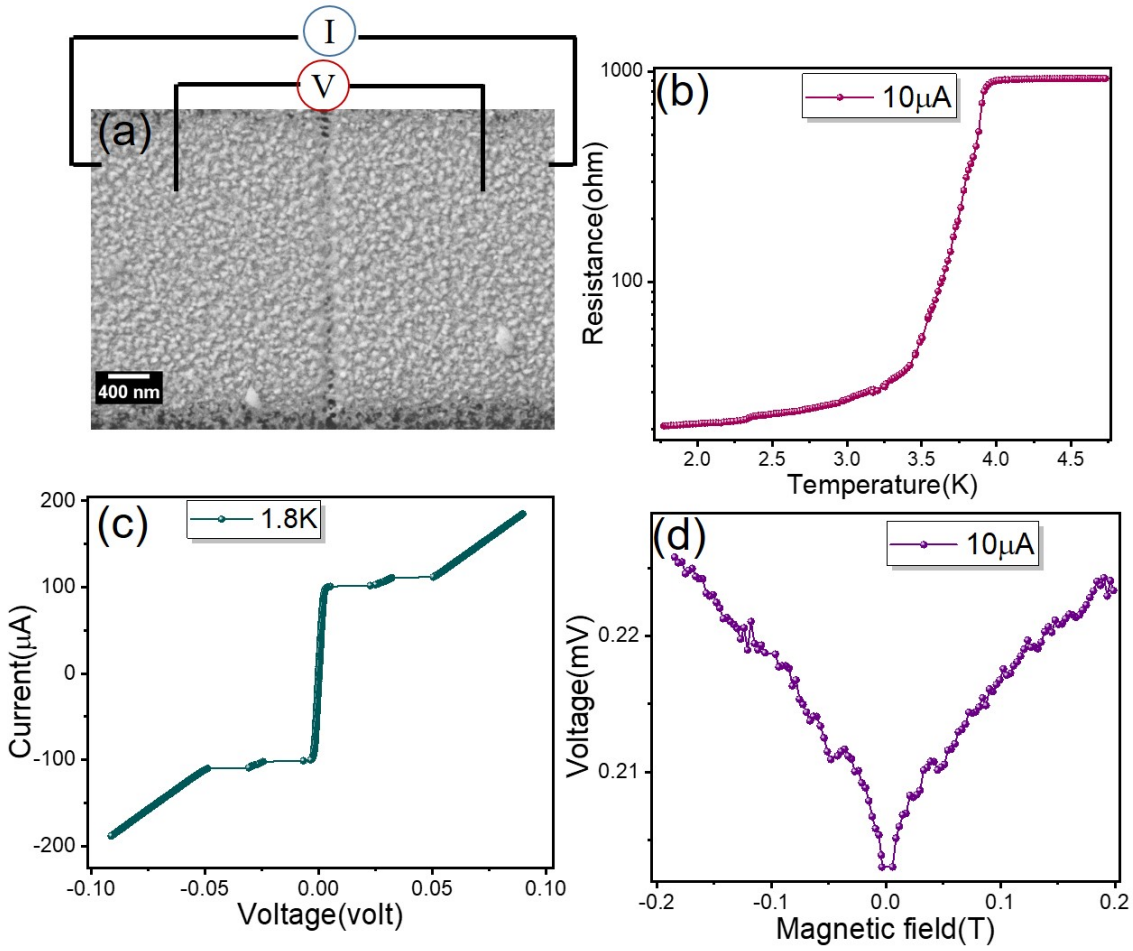

Figure 5.5: Wide track poisoned at a dose of 200mC/cm^2. (a) SEM image of the sample showing the poisoned region in the middle, (b) Resistance(R) vs temperature(T) measurement plot for the sample where T_c is prominent at 3.8K (c) Current(I) vs voltage(V) at 1.8K showing distinct steps indicates the phase slip activities, (d) Voltage(V) vs magnetic field(T) at bias current 10μA at 1.8K.

wide track was subjected to Ga-implantation with a low dose of 200mC/cm^2. The results of the transport properties of the wide track implanted with Ga are displayed in Figure-5.5. Figure-5.5(a) illustrates the scanning electron microscopy (SEM) image of the track after the Ga-implantation process. The width of the implanted region, as indicated by the scale bar, measures approximately 80nm. The film texture appears granular, while the implanted area exhibits a relatively consistent pattern, as observed in the SEM image. The *RT* plot (measured at the same bias current of 10μA as previously) in Figure-5.5(b) illustrates an elevated residual resistance at 1.8K when compared to the previously recorded *RT* measurements depicted in Figure-5.4(b) before implantation.

The observed increase in residual resistance can be ascribed to a potential drop induced by the contaminated region affected by Ga implantation. To delve deeper into this matter, we conducted current-versus-voltage measurements. Figure 5.5(c) illustrates the recorded *IV* curve for the respective sample, revealing a significant reduction in the superconducting critical current (*Ic*) when compared to the pre-implantation measurements of *Ic* in Figure 5.4(c). This outcome is as anticipated, considering the emergence of a finite voltage, akin to the response observed in the *RT* curve (Figure 5.5(b)). The rise in potential drop across the Ga-implanted barrier region significantly influences the reduction in *Ic*, leading to an earlier transition of the track to the normal state. Additionally, we repeated the measurement of voltage versus magnetic field to observe the magneto-resistance response, as depicted in Fig-5.5(d). Here a similar linear voltage response concerning the magnetic field has been recorded.

In our experimental plan, we outlined our intention to observe Josephson junction-like behaviour in a device created using the Ga-implantation technique. Figure-5.6(a) shows the SEM image of this spot after narrowing down using FIB. To investigate the transport properties of this nanowire sample, we conducted measurements using similar protocols. Firstly, we performed a resistance (*R*) vs temperature (*T*) measurement, as illustrated in Figure-

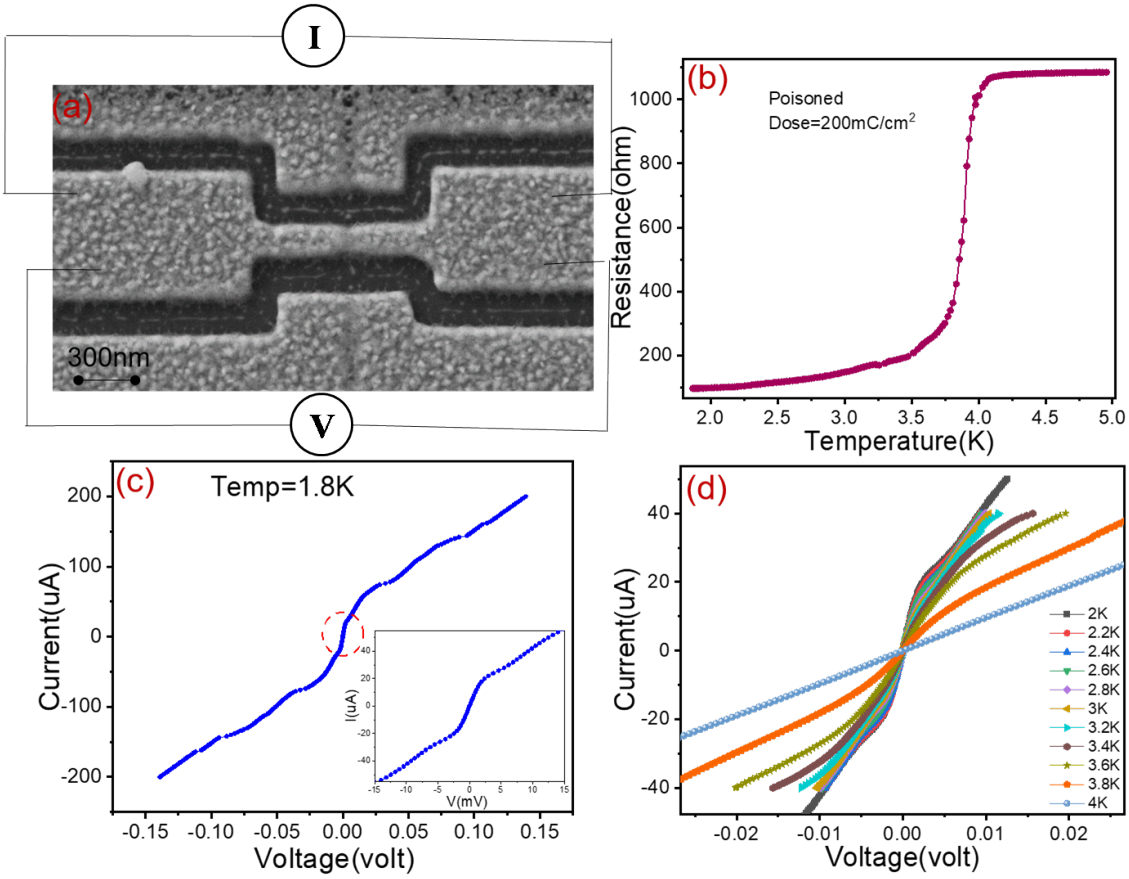

Figure 5.6: Nanowire geometry on the poisoned spot. (a) SEM image of the nanowire-implanted spot. (b) Resistance (R) vs temperature (T) plot of the corresponding sample. (c) The sample's current (I) vs voltage (V) plot at 1.8K. Inset: zoomed region of the dotted circular region. (d) Temperature-dependent of IV measurements plot.

5.6(b). Here the *RT* plot clearly indicates a further increase in the resistance at 1.8K, which is expected due to the voltage drop across a narrow poisoned region. The sample became resistive, but the superconducting nature was not hampered by this procedure. It is well known that the superconducting nanowires typically exhibit a resistive state at low temperatures [127]. In Figure-5.6 (c) and (d), we have illustrated the IV characteristic curves. Figure-5.6(c) displays the IVC measured at 1.8K. The main panel in the figure represents the entire IV curve upto $\pm 200\mu$A, similar to the range of Figure-5.4 and Figure-5.5. The inset IV curve exhibits characteristics of a Josephson junction. To further confirm the presence of Josephson junction-like characteristics of the low current regime (between $\pm 50\mu$A,), we conducted IV measurements at various temperatures, as depicted in Figure-5.6(d). In this case, the critical current (*Ic*) consistently decreased from 2K to 3.8K. The extracted *Ic*

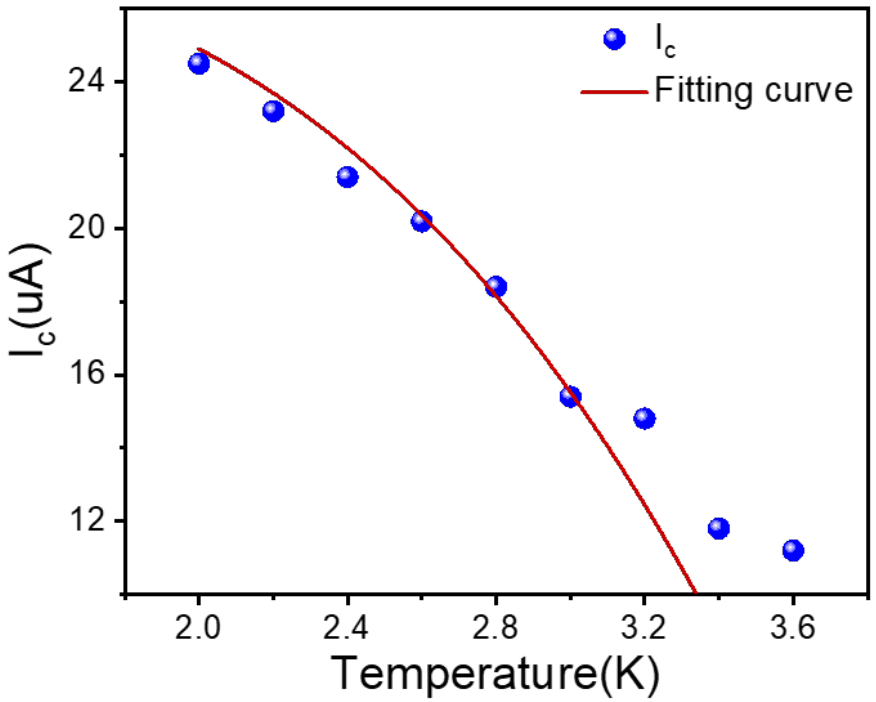

Figure 5.7: Ic vs temperature(T) plot. Blue points are the experimental data and Red solid curve is the fitting curve.

values from each IV curve are plotted in figure-5.7, and fitted using the provided theoretical

model shown below [183]:

$$I = Ic\left[1 - \frac{T}{Tc}\right]^n \tag{5.1}$$

using the parameters Ic, T_c, and n. Following the fitting procedure, the value of n was determined to be 0.428, indicating that the junction barrier tends to exhibit more insulating characteristics [183].

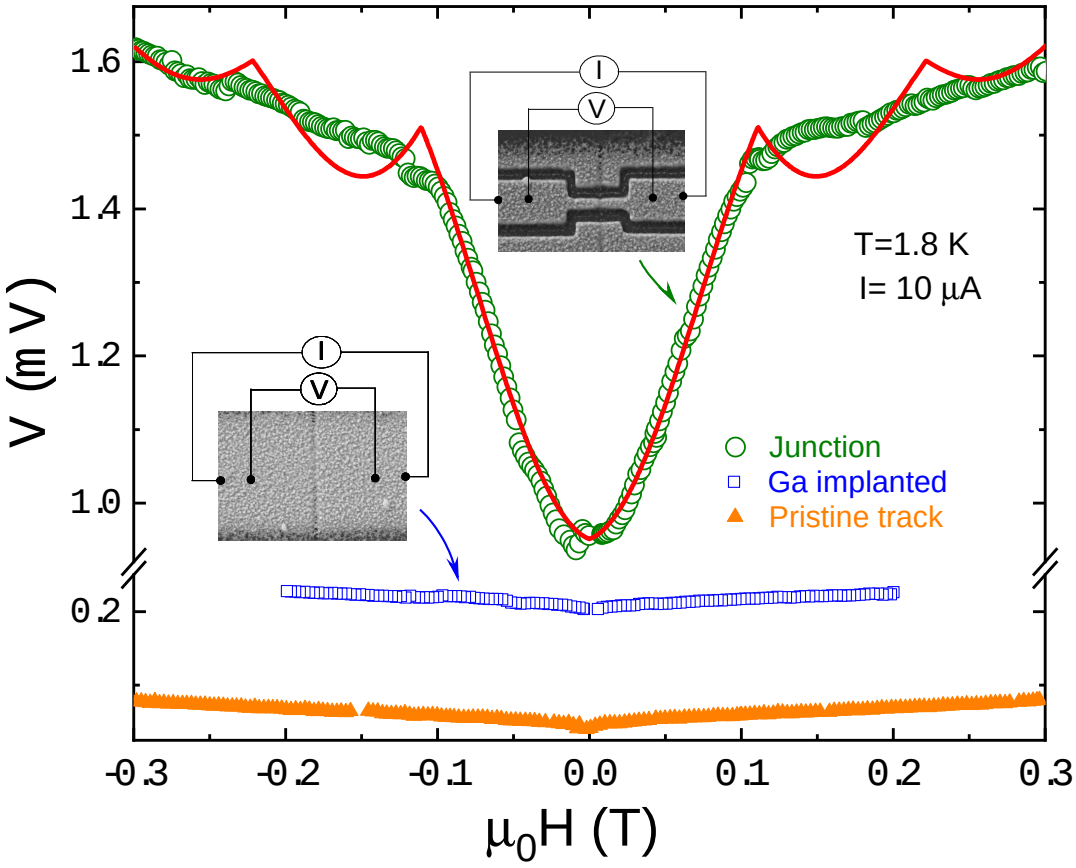

Figure 5.8: Voltage (V) vs magnetic field (H) measurement for different stages of $NiBi_3$ track. Orange plot represents the VH for pristine track, Blue represents the VH for Ga implanted wide $NiBi_3$ track and Green plot represents the VH for 200nm nanowire Ga implanted $NiBi_3$ track. Red solid curve shows the simulated VH curve.

By using HRTEM, it has been shown in the chapter-4 that the underlying microstructure of co-evaporated $NiBi_3$ film is highly granular with well defined grain boundaries. Therefore, transport phenomena in these films, even in the superconducting state, is largely

dominated by intergrain coupling across the grain boundaries. The effect of the large fraction of grain boundaries is evident from the fact that even 5μm wide virgin tracks of $NiBi_3$ exihibit a large residual resistance at 1.8K, well below the T_c. Therefore, Ga poisoning of the nanoscale grains and grain boundaries can indeed be expected to shift the inter-grain conductance towards the insulating side. As a result, the temperature dependence of critical current shows a critical exponent (n in the fitted curve in fig-5.7) closer to the insulating barrier type.

A more defining feature of a Josephson junction is quantization of magnetic flux through the junction. As a result of the flux quantization the critical current across a josephson junction takes a magnetic field dependence of the form:

$$I_c\left(\Phi_J\right) = I_0 \cdot \left| \frac{\sin \pi \frac{\Phi_J}{\Phi_0}}{\pi \frac{\Phi_J}{\Phi_0}} \right| \tag{5.2}$$

where Φ_0 is the flux quanta and I_0 is critical current at zero magnetic field. When the voltage across a junction is measured, instead of the critical current as a function of magnetic field, the qualitative features of the Fraunhoffer-like periodic oscillations remain the same, albeit with maximas replaced by minima and vice-versa. The junction voltage measurement, at a fixed bias current close to the critical current is a much quicker method of detecting flux quantization compared to the critical current measurements. The equivalence of these two modes of measurements has been shown in a recent publication [184].

In the figure-5.8, we have shown the magnetic field dependence of the voltage across the nanowire junction. clearly, the *V(H)* in this case is significantly different from the *V(H)* of the wider track of $NiBi_3$ before and after defining the ion implanted junction area. For a direct comparison, we have shown all three *V(H)* curves in the Fig-5.8, on the same scale. The nanowire junction shows a clear Fraunhoffer-like dependence, unlike the wider track. It can, however be noted that only the first lobe of the Fraunhofer pattern is apparent while

higher-order lobes are suppressed, possibly due to the resistive nature of the superconducting state in the $NiBi_3$ electrodes. We have attempted to simulate the *V(H)* curve of the nanowire junction by adding a resistive background to the Fraunhofer like oscillatory function as below:

$$V(H) = \mathrm{V_{BG}} - \mathrm{V_{c0}} \times \left| \frac{\sin \Phi \times H}{\Phi \times H} \right| + [\mathrm{M} \times |H| + \mathrm{C}] \tag{5.3}$$

where the parameter $\Phi = \frac{\pi \times \text{Junction Area}}{\Phi_0}$, $\mathrm{V_{BG}}$= a constant background voltage, M and C are the slope and intercept of the assumed linear resistive background voltage respectively. Assuming a linear background voltage as a function of magnetic field is reasonable based on the linear *V(H)* of the wider junctions shown in the figure-5.8. The solid line in the figure-5.8 shows the fit using the above function. From this fitting, we have estimated a value of $\Phi_0 \sim 2.24 \times 10^{-15}\ T.m^2$ by considering a junction area of 200nm × 100nm from SEM image. The estimated value of the flux quantum Φ_0 is very close the theoretical value $2.06 \times 10^{-15}\ T.m^2$. Therefore we have realized a nanowire josephson junction using local Ga ion implantation to define the junction area.

5.3.1.1 Transport results on the spot irradiated with high dose

In a separate experiment, we varied the gallium dose to demonstrate improves and clearer junction characteristics in the nanowire geometry. In Figure 5.9(a), the FESEM image displays the spot irradiated with a high dose of 492 mC/cm^2. As seen in this image, the nanowire's width (200nm) and length were kept similar to the low dose nanowire junction.

In Figure 5.9(b), the plot illustrates the resistance versus temperature plot for this nanowire junction measured at a bias current of $I = 1\mu A$. We note that even with 1μA bias current, in this case the residual resistance at 1.8K is similar to the residual resistance of the low dose junction (Fig-5.6). This indicates that the high-dose junction is much more resistive compared to the low-dose junction, as expected. From the *I(V)* curves shown in Fig-5.9(c) we

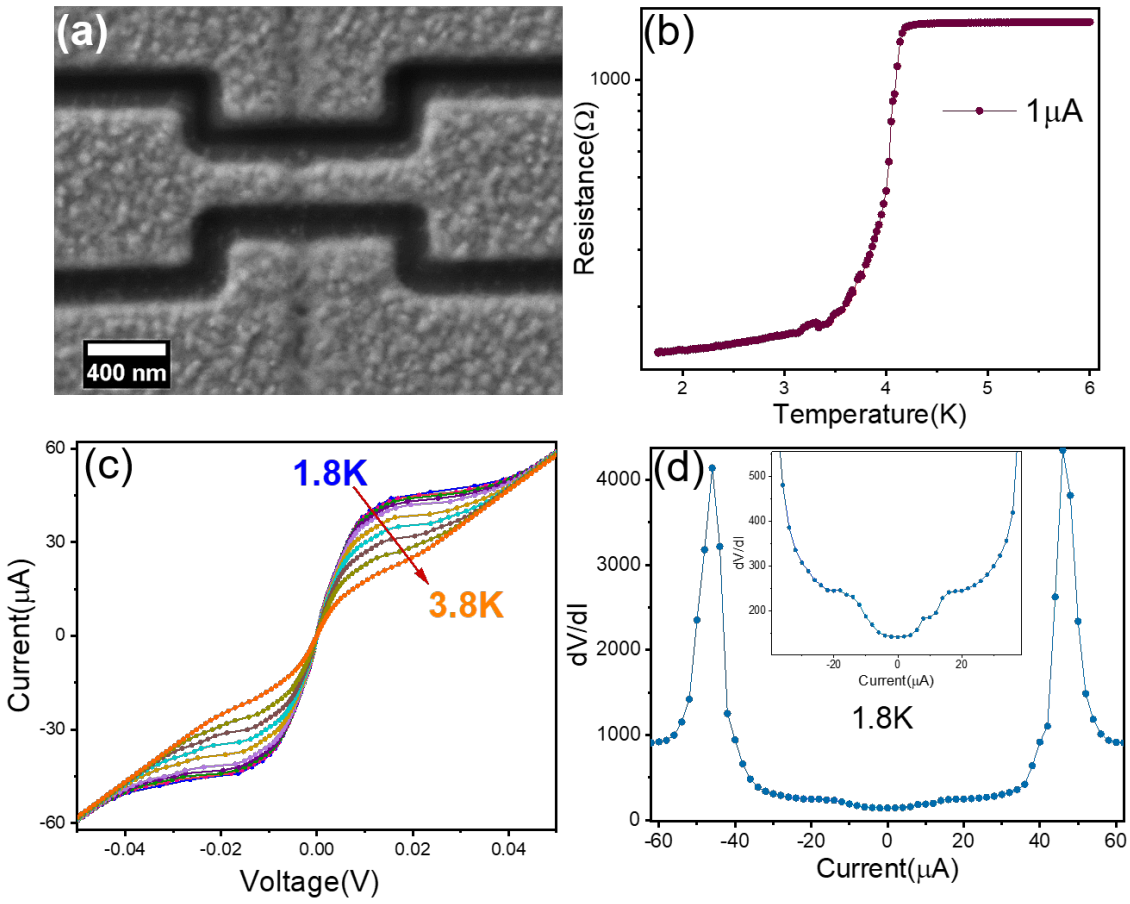

Figure 5.9: (a) FESEM image of the track exposed with high dose of 492mC/cm^2. (b) Resistance(R) vs temperature(T) of the corresponding spot. (c) Current (I) vs voltage (V) plot measured with increasing temperature. (d) dV/dI curve generated from IV plot at 1.8K. Inset: zoomed region of central part shows the junction critical current.

notice clearly that the resistance corresponding to 10μA current is close to 500Ω, compared to the $\sim$ 100Ω resistance of the low dose junction at 10μA current. The superconducting T_c is consistent with the previous one. Figure 5.9(c) depicts the current versus voltage characteristics at temperatures ranging from 1.8K to 3.8K. At higher currents, specifically around 40μA, a change in the slope of the *I(V)* curve is evident, showcasing the typical characteristics of superconducting electrodes. However, a distinct change in slope is observed at lower bias current values, indicating the typical *I(V)* characteristics of a weak link acting

as a junction. To further validate this observation, we have presented a *dV/dI* plot (Figure 5.9(d)), extracted numerically from *I(V)* curve at 1.8K. This curve shows a dip reflecting the change in slope corresponding to *I(V)* curve. From here the Junction critical current appears to be around 5μA compared to the critical current of 15μA for the low dose junction.

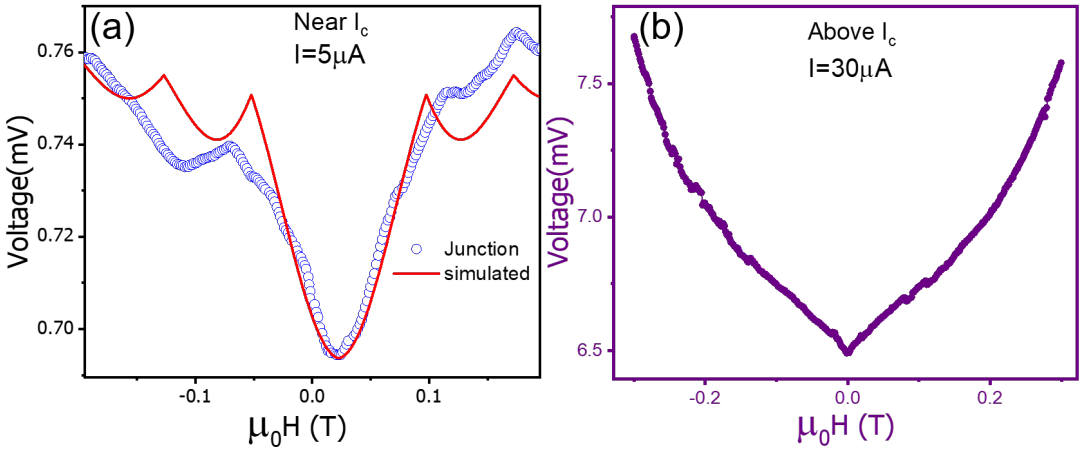

Figure 5.10: (a) Voltage vs magnetic field for the high dose sample measured near Ic value (b)Voltage vs magnetic field for the high dose sample measured above Ic value.

For further verification of typical characteristics of a Josephson junction, we have measured the voltage (V) vs magnetic field (H) near the critical current values. Here we present the *V(H)* plot at $I=5\mu A$ in Figure-5.10 (a), where the Blue curve is the experimental plot and the Red curve is the simulated plot using equation 5.3.

In Figure 5.10(a), it is noticeable that the *V(H)* curve has a slight shift from the origin along the x-axis. In the fitted curve this shift along the x-axis was accommodated by replacing $|H|$ by $|H+D|$, where D was a constant representing the magnitude of the shift. The reason behind this shift could be due to vortex trapping in the junction as the high Gallium dose exposure and the granularity of the thin film increase the likelihood of vortex trapping at the junction region. In addition to this, a noticeable asymmetry is observed in the *V(H)* curve between the positive and negative magnetic field sides. We attribute this asymmetry to the granularity present in the thin film, causing a non-uniform distribution of current

along differently coupled grains through the Ga-implanted barrier. In this context, the simulated RED curve closely matches the Blue curve in the first minima and the positions of the second and corresponding third lobes, except for slight deviations due to the asymmetry. So here the second lobe and above in the *VH* curve is clearly visible which means the Josephson coupling is better established compared to the low-dose sample. Figure-5.10(b) shows the *V(H)* measured at $I=30\mu A$ above I_c of the Junction, which shows typical characteristics of a nanowire rather than a junction. So in this section, we have presented the nanowire geometry with Gallium irradiated barriers at 2 different doses and both the samples show typical Junction characteristics.

5.4 Summary

In this chapter, we have discussed a simple technique to fabricate planar Josephson junction using Gallium implantation technique. Here we have fabricated 2 different type of geometry for realizing the josephson junction features: Nanowire geometry and Notched geometry. Before making the wide $NiBi_3$ track into nanowire and notched structure, one background transport study on wide $NiBi_3$ track was done. In the background measurements, we observe the resistive nature of the track as well as a linear field dependence of voltage. The characteristic features of phase slip activity in the sample was recorded in the *IV* measurement plot. In the nanowire geometry, the sample with low dose barrier exposure of Gallium, shows josephson junction type features as well as the high dose sample. The *V(H)* plot in high dose sample showed comparatively cleaner second and third lobe than the low dose sample. The characteristic I_c vs temperature curve well fitted with theoretical model [183] conveying the junction barrier to be of low conductance .

Chapter 6

Conclusion and Future scope

6.1 Summary

A summary of the key results of this thesis is presented in this chapter. Studying of structural and physical properties of Ni-Bi system in nanoscale geometry have been the focus of this thesis. Using a complete physical approach fabrication of $NiBi_3$ nanowires and Ni-$NiBi_3$ nanoparticles were done where the structural properties were studied. Transport on $NiBi_3$ nanowires fabricated from thin film of $NiBi_3$ were done in order to study the phase slip and effect of magnetic Ni impurity on the magnetoresistance measurements. Transport on Ga-implanted $NiBi_3$ nanowires (200nm) show typical josephson junction characteristics. On these two approach fabrication and transport, we have summarized in the following sections.

Chapter 1: In this chapter we discuss a self catalyzed growth of $NiBi_3$ nanowires on $NiBi_3$ films during physical vapour deposition. It is known from earlier work that Ni and Bi react spontaneously to form $NiBi_3$ due to the negative formation energy at room temperature. As a result, several groups have shown that a layer of $NiBi_3$ appears at the interface between Ni and Bi layers [70]. Therefore simultaneous evaporation of Ni and Bi onto a substrate can indeed be expected to form a film of $NiBi_3$. In addition, the reported reactive diffusivity between Ni and Bi (even in the solid phase) [185] indicates that there is a possibility of catalyzed growth of $NiBi_3$ rods, especially because of the high effective temperature of the vapour phase Ni and Bi arriving on a substrate. Based on this argument we thermally co-evaporated Ni and Bi metals onto Si/SiO_2 substrates. The evaporation rate of Bi and the temperature of the substrate were used as the control parameters in this

experiment. We observed a significant increase in the roughness of the films as the Bi evaporation rate was increased. At sufficiently high evaporation rate of Bi (with fixed Ni evaporation rate) clump-like nanorods began to emerge on the surface of the $NiBi_3$ films. These nanorods had an average length of approximately 2 μm and a diameter of about 300 nanometers. Subsequently, by elevating the temperature of the substrate holder from ambient to 250 degrees Celsius, long, straight nanorods were found to grow alongside the thin film. These nanorods had an average length of around 25 micrometers and a diameter of about 300 nanometers. X-ray diffraction analyses of the thin film samples revealed a strong correlation between the growth of nanorods with the presence of the hexagonal phase of Bismuth in the $NiBi_3$ films. We believe the similarity of the similarities in the lattice constants of hexagonal Bismuth phase with the orthorhombic $NiBi_3$ promotes preferential growth of $NiBi_3$ nanorods. However, at ambient temperatures, the nanorods were found to be highly polycrystalline in nature. When the substrate temperatures close to the melting point of Bi was used we found excellent single crystalline, vertically aligned, $NiBi_3$ nanorods on the surface of $NiBi_3$ films. Typical widths of these $NiBi_3$ nanorods were found to be $\sim$200 nm and typical lengths varied between 5 μm and 20 μm. High resolution transmission electron microscopy revealed the presence of an amorphous cap of Bi on top of the crystalline nanorods. This finding strongly suggests a growth mechanism reminiscent of the well-known vapor-liquid-solid (VLS) growth mechanism [84, 85]. In a typical VLS mechanism of formation of nanorods a molten metallic particle helps in capturing and crystallizing a chemical vapour. The molten metallic catalyst remains as a solid particle at the top of the nanorods in such processes. In an analogous manner, when physical vapour deposition is performed at substrate temperatures close to the melting point of Bismuth, in our case, the molten Bi strongly catalyzes the formation of $NiBi_3$ nanorods and finally freezes on the top of the nanorods in the amorphous form.

Chapter 2: In this chapter we discuss an attempt at the formation of a superconducting $NiBi_3$ shell on a ferromagnetic Ni core, following a fully physical route. Essentially, our goal is to produce isolated hybrid nanoparticles combining superconducting and ferromagnetic materials in the spirit of core-shell nanoparticles. The fact that $NiBi_3$ forms at the interface of Ni and Bi, was at the heart this attempt. In this work we started with a thin sputterred film of Ni and used solid state thermal dewetting [186, 116] process to obtain isolated nanoparticles of Ni on Si/SiO_2 substrates. In this process, we varied the average size of the Ni nanoparticles in the range of $\sim$ 100 nm, by changing the duration of annealing. The magnetization measurement on bare Ni nanoparticles showed superparamagnetic behavior as expected for a collection of small ferromagnetic nanoparticles [187, 118, 188]. Subsequent thermal evaporation of a thin layer of Bi onto these ferromagnetic nanoparticles, at elevated substrate temperatures, caused reactive diffusion at the top surface of the Ni nanoparticles to form a $NiBi_3$ layer. The resulting superconducting $NiBi_3$ sheath around the Ni particles was verified from analysis of high resolution transmission electron microscopy (HRTEM) on single Ni nanoparticles. While the HRTEM of bare Ni nanoparticles showed a clean and sharp Ni boundary whereas, the Bi-coated Ni nanoparticles showed a boundary of $NiBi_3$. The thickness of this $NiBi_3$ boundary was around 7 nm. The temperature dependent magnetization measurements of these nanoparticles showed a diamagnetic transition around 3K, superimposed on the strong ferromagnetic background (positive) moment of the underlying Ni nanoparticles.

Chapter 3: Starting with this chapter we shift our focus to the quantum transport in $NiBi_3$ nanowires, which were patterned from co-evaporated $NiBi_3$ films using lithography techniques. $NiBi_3$ films prepared via co-evaporation of Bi and Ni invariably contains some surplus Ni, as we have observed from the X-Ray diffraction measurements. Surprisingly, however the superconducting transition temperature of these films were found to be completely unaffected, unlike the typical superconductors, which suffer a significant degrada-

tion with ferromagnetic impurity. However, we observe a very pronounced resistive state of the nanowires patterned from these films, below the superconducting transition temperature. The low temperature resistive state in superconducting nanowires is usually a result of phase slip events [149, 128]. In this chapter we study how the microscopic phase slip behavior and the macroscopic order parameter fluctuations respond to the presence of significant magnetic Ni impurities in the system. The microscopic phase slip events operate at the scale of coherence length and add a local resistance. The time averaged resistance across many individual events spread over the entire length of superconducting nanowires lead to the resistive state of superconducting nanowires [95, 128] below the transition temperature. It has been shown that the magnitude of bias current significantly affects resistance in the resistive state. Therefore, in order to study the effect of magnetic impurities on this process we prepared two $NiBi_3$ films with different amount of Ni impurities. In order to reduce the Ni impurity in $NiBi_3$ film we placed a magnetized mesh in front of the substrate, during the deposition, to filter out some of the Ni. In contrast to the usual $NiBi_3$ films the x-ray diffraction pattern of the film deposited through magnetized mesh shows no diffraction peaks corresponding to Ni. Although one can not claim complete removal of Ni from the co-evaporated $NiBi_3$ films without further microscopic investigations, we can safely claim that the films deposited through magnetized mesh has much less Ni impurity. Therefore we have named this sample as ”low-Ni” and the film deposited without the magnetized mesh has been named ”high-Ni” sample. Current dependent resistance measurements below transition temperature was performed on nanowires of diameters varying from 70 nm to 400 nm, fabricated from the high-Ni and low-Ni films. Earlier reports [127] have shown that quantum phase slip (QPS) process ($R_{QPS} \propto e^{\frac{-\Delta F \cdot \tau}{h}}$) is expected dominate below 0.7 T/T_c, whereas thermally activated phase slip (TPS) process ($R_{TPS} \propto e^{\frac{-\Delta F}{kT}}$) dominates above this temperature. By fitting the low temperature resistance of the $NiBi_3$ nanowires using these models we extracted the actual crossover temperature (T_S) between the quantum and

thermal regimes of QPS. We found that T_s tends to be lower in the high-Ni nanowire compared to the low-Ni nanowire. With increasing bias current density the T_S decreased almost linearly for both high-Ni and low-Ni nanowires, albeit with different slops. We interpreted this effect in terms of the affinity of the high-Ni nanowire to form phase slip lines, which leads to early onset of thermal phase slip regime.

In the second part of this chapter we discussed how macroscopic order parameter fluctuations get affected by the presence of magnetic impurities. Kivelson and Spivak [152] have shown that large fluctuations in amplitude and sign of the order parameter in a superconducting system can lead to oscillations in magnetoresistance in the resistive state. We have observed from scanning electron microscopy that co-evaporated $NiBi_3$ films have highly granular texture. High resolution TEM also showed $NiBi_3$ grains separated by mostly amorphous grain boundaries. In the high-Ni film the grain boundaries are naturally expected to have significant amount of Ni impurities. This situation mimics the S-F-S Josephson coupling at a granular level and 0-type, π-type Josephson coupling is expected because of the variation in the inter-grain separation. In this case, it is reasonable to assume that the inter-grain Josephson coupling can have a random distribution of 0-type and π-type couplings.The distribution in the size and the distribution in coupling between $NiBi_3$ grains (due to Ni impurities) match very well with the assumptions of the model of Kivelson and Spivak. Therefore, the granular $NiBi_3$ nanowires are excellent systems to study this effect. In comparison to the high-Ni nanowire, the low-Ni nanowire is expected to have much less fluctuations and a comparative study can be performed for the validation of the model of Kivelson and Spivak. We conducted magnetotransport measurements on $NiBi_3$ nanowires across a range of bias currents and temperatures. Above the superconducting transition temperature, the change in magnetoresistance (MR%) remained notably low ($\sim$ 0.0005%). It exhibited a linear increase with respect to the magnetic field, showing a similar pattern for both high Ni and low Ni samples. However, in the resistive state of the nanowires below

the transition temperature, the high-Ni nanowire showed clear oscillations in the magnetoresistance. On the other hand the low-Ni nanowire of the same dimension did not show any oscillations. We believe that the MR oscillations arise from the quantization of the applied magnetic flux inside the nanowire, via supercurrent loops facilitated via random zero and π Josephson couplings. This observation is, therefore, a clear experimental validation of the Kivelson-Spivak model of magnetotrnsport in a superconducting system with large fluctuations in the amplitude and sign of the order parameter.

Chapter 4: In this chapter we have explored the possibility of realizing planar nanowire Josephson junctions from the $NiBi_3$ nanowires by Ga-ion irradiation. This is interesting because the granular nanowires of $NiBi_3$ have a pronounced resistive state, and any Josephson junction realized from these nanowires will have highly resistive electrodes, unlike typical Josephson junctions. For this purpose a thin film of 48 nm $NiBi_3$ was lithographically patterned to get a 5um wide track. In the subsequent phase of the process, the wide track was narrowed down to a width of 200 nm and length of 1 μm utilizing a Ga focused ion beam milling technique at 30 kV. The same Ga ion beam was then used to define the junction area by irradiating $\sim$80 nm wide track across the 200 nm wide nanowire, at low beam voltage of 5 kV. We used two different doses of Ga implantation viz. 200 mC/cm^2 and 500 mC/cm^2. These nanowire junctions were termed as low dose and high doze samples, respectively. The irradiated nanowires did produce IV curves similar to Josephson junctions, with very low values of critical currents. However, for a functioning Josephson junction, a typical indicator is the presence of Fraunhofer oscillations [189] in the critical current versus μ_0H or, equivalently, similar oscillations in the voltage across the junction (V) as a function of applied field (H) at a fixed current bias. The V-H curves in these devices indeed showed Fraunhofer type oscillations, albeit with a magnetoresistance background of the nanowire. The value of flux quantum extracted from these quantization resulted a value of 2.24 $\times$ 10^{-15} Wb.m, which is very close to the actual value. For the high dose nanowire, where

the junction was exposed to more Ga ion, we observed a Fraunhofer patterns asymmetric in magnetic field, which could be due to non-uniform current distribution in the junction due to factors such as vortex trapping and non-uniform coupling strength across the junctions due to the highly granular nature of $NiBi_3$ layer.

Following the above discussions we have concluded the thesis with an outlook on the possible extensions of our work in various directions. The overall summary of the thesis has been shown in the following schematic.

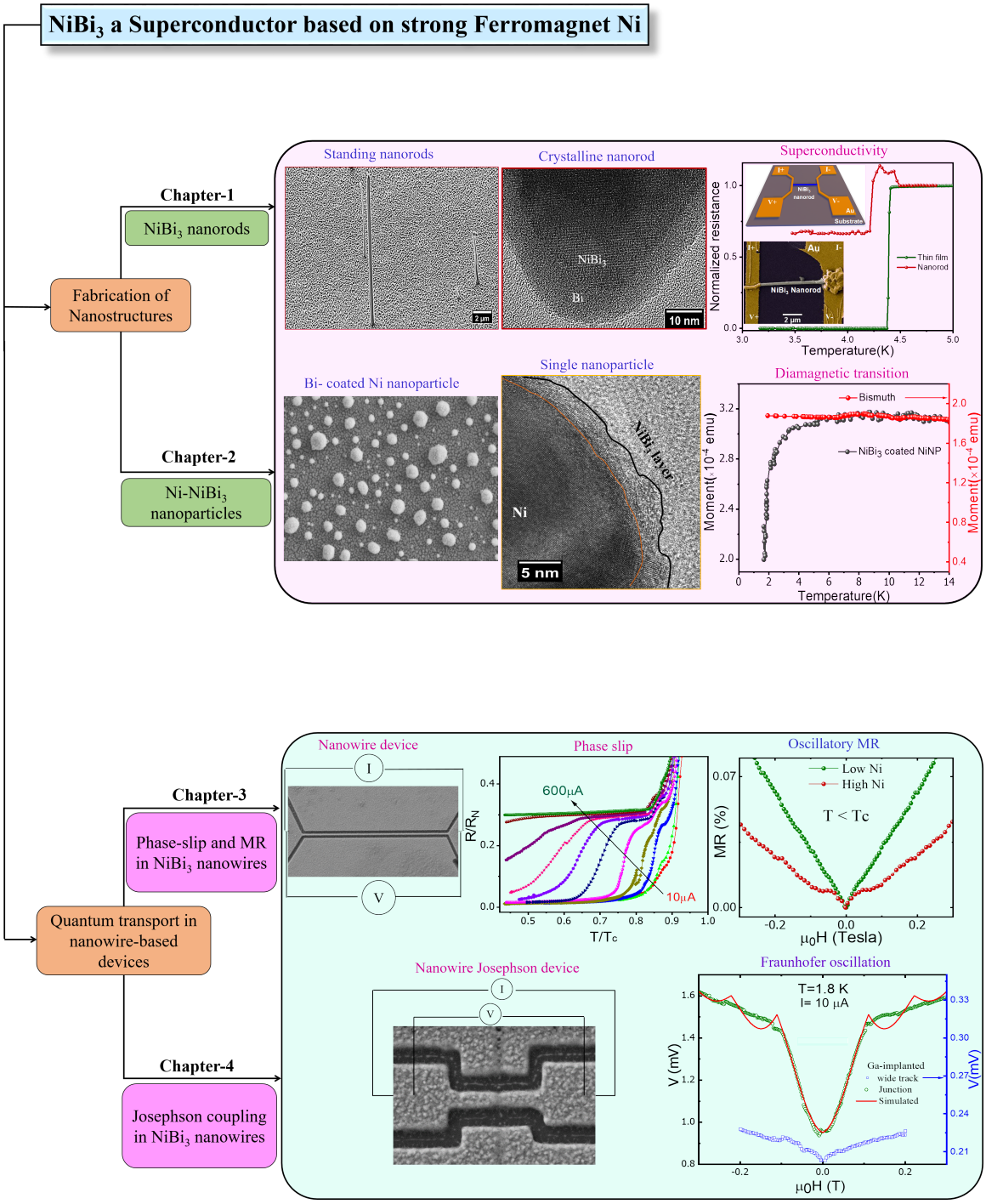

Figure 6.1: Pictorial summary of the thesis.

6.2 Future Scope

In this thesis, we have been able to fabricate and study some nanostructures of $NiBi_3$ system such as nanoparticles, nanowires. There is however, plenty of scope for further research in these nanostructures of $NiBi_3$. Below we list a few of the possible directions of future work:

- In Chapter 2, we explored the creation of single-crystalline $NiBi_3$ nanowires, uncovering their superconducting properties. The single crystal $NiBi_3$ nanowires can be ideal for studies of superconducting phase slip and also to realize phase slip Josephson junctions.

- In Chapter 4, we examined phase slip fluctuations in $NiBi_3$ patterned polycrystalline nanowires, which lead to magnetoresistance oscillations. Similar studies in single-crystalline nanowires would also be interesting to examine how sensitive the MR oscillations are to phase fluctuations.

- In Chapter 3, we have addressed the fabrication process of Ni-$NiBi_3$ S-F hybrid nanoparticles. Superconducting proximity effect in these superconductor quoted ferromagnetic particles could be an interesting direction because of the confined structure in which superconducting correlations develops. Individual Ni-$NiBi_3$ particles can be studied by scanning tunneling spectroscopy to explore the effect of confinement on the induced superconductivity.

- Till now the proximity effect in S-F multilayer hybrid structures has been extensively investigated. However, certain aspects of the proximity effect, such as the damped oscillatory behavior of the superconducting order parameter at ferromagnetic interfaces and the occurrence of long-range spin-triplet supercurrent at ferromagnetic interfaces with a non-collinear magnetic moment, can be explored in the context of S-F or F-S hybrid nanoparticle geometries.

References

[1] H Kamerlingh Onnes. The discovery of superconductivity. *Commun. Phys. Lab*, 12:120, 1911.

[2] Om Prakash, Anil Kumar, A. Thamizhavel, and S. Ramakrishnan. Evidence for bulk superconductivity in pure bismuth single crystals at ambient pressure. *Science*, 355(6320):52–55, 2017.

[3] John Bardeen, Leon N Cooper, and John Robert Schrieffer. Theory of superconductivity. *Physical review*, 108(5):1175, 1957.

[4] J. S. Shier and D. M. Ginsberg. Superconducting transitions of amorphous bismuth alloys. *Phys. Rev.*, 147:384–391, Jul 1966.

[5] Joseph M. Reynolds and C. T. Lane. Superconducting bismuth alloys. *Phys. Rev.*, 79:405–406, Jul 1950.

[6] Huan Li, Yanan Wang, Yutaro Aoki, Saki Nishiyama, Xiaofan Yang, Tomoya Taguchi, Akari Miura, Ai Suzuki, Lei Zhi, Hidenori Goto, Ritsuko Eguchi, Takashi Kambe, Yen-Fa Liao, Hirofumi Ishii, and Yoshihiro Kubozono. A new protocol for the preparation of superconducting kbi2. *RSC Adv.*, 10:26686–26692, 2020.

[7] S K Kushwaha, J W Krizan, J Xiong, T Klimczuk, Q D Gibson, T Liang, N P Ong, and R J Cava. Superconducting properties and electronic structure of nabi. *Journal of Physics: Condensed Matter*, 26(21):212201, may 2014.

[8] Sharon S. Philip, Junjie Yang, Despina Louca, P. F. S. Rosa, J. D. Thompson, and K. L. Page. Bismuth kagome sublattice distortions by quenching and flux pinning in superconducting $rbbi_2$. *Phys. Rev. B*, 104:104503, Sep 2021.

[9] S Tencé, O Janson, C Krellner, H Rosner, U Schwarz, Y Grin, and F Steglich. $CoBi_3$– the first binary compound of cobalt with bismuth: high-pressure synthesis and superconductivity. *Journal of Physics: Condensed Matter*, 26(39):395701, sep 2014.

[10] Maximilian Amsler, S. Shahab Naghavi, and Chris Wolverton. Prediction of superconducting iron–bismuth intermetallic compounds at high pressure. *Chem. Sci.*, 8:2226–2234, 2017.

[11] Roozbeh Sheikhi and Junghyun Cho. Growth kinetics of bismuth nickel intermetallics. *Journal of Materials Science: Materials in Electronics*, 29:19034–19042, 2018.

[12] P Nedellec, FV Creppy, L Dumoulin, and JP Burger. Anomalous electrical resistivity of Bi_3Ni. *Physics Letters A*, 111(1-2):67–70, 1985.

[13] Yasunobu Fujimori, Shin-ichi Kan, Bunjyu Shinozaki, and Takasi Kawaguti. Superconducting and normal state properties of $NiBi_3$. *Journal of the Physical Society of Japan*, 69(9):3017–3026, 2000.

[14] Jagdish Kumar, Anuj Kumar, Arpita Vajpayee, Bhasker Gahtori, Devina Sharma, PK Ahluwalia, S Auluck, and VPS Awana. Physical property and electronic structure characterization of bulk superconducting Bi_3Ni. *Superconductor Science and Technology*, 24(8):085002, 2011.

[15] Xiangde Zhu, Hechang Lei, Cedomir Petrovic, Yuheng Zhang, et al. Surface-induced magnetic fluctuations in a single-crystal $NiBi_3$ superconductor. *Physical Review B*, 86(2):024527, 2012.

[16] B Silva, RF Luccas, NM Nemes, J Hanko, MR Osorio, P Kulkarni, F Mompean, M García-Hernández, MA Ramos, S Vieira, et al. Superconductivity and magnetism on flux-grown single crystals of $NiBi_3$. *Physical Review B*, 88(18):184508, 2013.

[17] Masashi Sakurai, Takafumi Ono Takafumi Ono, Ikushi Yoshida Ikushi Yoshida, and Seiichi Tanuma Seiichi Tanuma. Thermoelectric and thermogalvanomagnetic properties of $NiBi_3$. *Japanese Journal of Applied Physics*, 39(11R):6366, 2000.

[18] Kristin Persson. Materials data on nibi (sg:194) by materials project, 5 2016. An optional note.

[19] M Milewits, SJ Williamson, and Haskell Taub. Exponential temperature dependence of the electrical resistivity of V_3Si. *Physical Review B*, 13(12):5199, 1976.

[20] V Marchenko. Temperature dependence of the electrical resistivity of V_3Si. *Soviet Physics-Solid State*, 15(6):1261–1262, 1973.

[21] GW Webb, Z Fisk, JJ Engelhardt, and SD Bader. Apparent t^2 dependence of the normal-state resistivities and lattice heat capacities of high-t_c superconductors. *Physical Review B*, 15(5):2624, 1977.

[22] John A Woollam and Samuel A Alterovitz. Electronic properties of $pbmo_6s_8$ and $Cu_xMo_6S_8$. *Physical Review B*, 19(2):749, 1979.

[23] B Jayaram, SN Ekbote, and AV Narlikar. Superconductivity of binary and ternary compounds of Bi. *Physical Review B*, 36(4):1996, 1987.

[24] L Dumoulin, P Nedellec, JP Burger, and FV Creppy. Superconductivity in d-and f-band metals. *Kernforschungszentrum Karlsruhe*, page 473, 1982.

[25] AF Ioffe and AR Regel. Non-crystalline, amorphous, and liquid electronic semiconductors. In *Progress in semiconductors*, pages 237–291. 1960.

[26] WL McMillan. Transition temperature of strong-coupled superconductors. *Physical Review*, 167(2):331, 1968.

[27] A B Karki, D A Browne, S Stadler, J Li, and R Jin. Pdte: a strongly coupled superconductor. *Journal of Physics: Condensed Matter*, 24(5):055701, jan 2012.

[28] L Amaral, P Nedellec, A Traverse, H Bernas, L Dumoulin, and JP Burger. Electrical transport properties of Bi_3Ni under helium irradiation and hydrogen implantation. *Journal of Physics F: Metal Physics*, 16(9):1239, 1986.

[29] Vantari Siva, Kartik Senapati, Biswarup Satpati, Sudakshina Prusty, DK Avasthi, D Kanjilal, and Pratap K Sahoo. Spontaneous formation of superconducting $NiBi_3$ phase in Ni−Bi bilayer films. *Journal of Applied Physics*, 117(8):083902, 2015.

[30] JS Moodera and R Meservey. Superconducting phases of bi and ga induced by deposition on a Ni sublayer. *Physical Review B*, 42(1):179, 1990.

[31] Xin-Xin Gong, He-Xin Zhou, Peng-Chao Xu, Di Yue, Kai Zhu, Xiao-Feng Jin, He Tian, Ge-Jian Zhao, and Ting-Yong Chen. Possible p-wave superconductivity in epitaxial Bi/Ni bilayers. *Chinese Physics Letters*, 32(6):067402, 2015.

[32] Vantari Siva, Paresh C Pradhan, G Santosh Babu, Maheswar Nayak, Pratap K Sahoo, and Kartik Senapati. Superconducting proximity effect in $NiBi_3-Ni-NiBi_3$ trilayer system with sharp superconductor-ferromagnet boundaries. *Journal of Applied Physics*, 119(6):063902, 2016.

[33] Vantari Siva, Abdelhak Chettah, Biswarup Satpati, S Ojha, D Kanjilal, and Pratap K Sahoo. Enhanced surface and interface diffusion in Ni−−Bi bilayers by swift heavy ion irradiation. *RSC advances*, 6(64):58950–58956, 2016.

[34] V Siva, A Chettah, S Ojha, A Tripathi, D Kanjilal, and Pratap K Sahoo. Interface mediated enhanced mixing of multilayered Ni−Bi thin films by swift heavy ion irradiation. *Nuclear Instruments and Methods in Physics Research Section B: Beam Interactions with Materials and Atoms*, 409:314–317, 2017.

[35] ZG Wang, Ch Dufour, E Paumier, and M Toulemonde. The Se sensitivity of metals under swift-heavy-ion irradiation: a transient thermal process. *Journal of Physics: Condensed Matter*, 6(34):6733, 1994.

[36] ZG Wang, Ch Dufour, E Paumier, and M Toulemonde. The Se sensitivity of metals under swift-heavy-ion irradiation: a transient thermal process. *Journal of Physics: Condensed Matter*, 7(12):2525, 1995.

[37] Xinxin Gong, Mehdi Kargarian, Alex Stern, Di Yue, Hexin Zhou, Xiaofeng Jin, Victor M Galitski, Victor M Yakovenko, and Jing Xia. Time-reversal symmetry-breaking superconductivity in epitaxial bismuth/nickel bilayers. *Science advances*, 3(3):e1602579, 2017.

[38] G Li, Q Zhang, D Rhodes, B Zeng, P Goswami, RE Baumbach, PH Tobash, F Ronning, JD Thompson, ED Bauer, et al. Bulk evidence for a time-reversal symmetry broken superconducting state in URu_2Si_2. *Physical Review B*, 88(13):134517, 2013.

[39] Junhua Wang, Xinxin Gong, Guang Yang, Zhaozheng Lyu, Yuan Pang, Guangtong Liu, Zhongqing Ji, Jie Fan, Xiunian Jing, Changli Yang, et al. Anomalous magnetic moments as evidence of chiral superconductivity in a Bi/Ni bilayer. *Physical Review B*, 96(5):054519, 2017.

[40] Ekta Bhatia, Abhishek Talapatra, Jyoti Ranjan Mohanty, and Kartik Senapati. Superconductivity, kondo effect, and observation of self-organized pattern formation in intermetallic $NiBi_3$ thin films. *Intermetallics*, 94:160–164, 2018.

[41] LY Liu, YT Xing, ILC Merino, H Micklitz, DF Franceschini, E Baggio-Saitovitch, DC Bell, and IG Solórzano. Superconductivity in Bi/Ni bilayer system: Clear role of superconducting phases found at Bi/Ni interface. *Physical Review Materials*, 2(1):014601, 2018.

[42] Hexin Zhou and Xiaofeng Jin. Stray field and vortex controlled magnetoresistance in superconducting Bi/Ni bilayers. *Journal of Magnetism and Magnetic Materials*, 458:171–175, 2018.

[43] Prashant Chauhan, Fahad Mahmood, Di Yue, Peng-Chao Xu, Xiaofeng Jin, and NP Armitage. Nodeless bulk superconductivity in the time-reversal symmetry breaking Bi/Ni bilayer system. *Physical review letters*, 122(1):017002, 2019.

[44] Sung-Po Chao. Superconductivity in a Bi/Ni bilayer. *Physical Review B*, 99(6):064504, 2019.

[45] Hexin Zhou, Xinxin Gong, and Xiaofeng Jin. Magnetic properties of superconducting Bi/Ni bilayers. *Journal of Magnetism and Magnetic Materials*, 422:73–76, 2017.

[46] T Herrmannsdörfer, R Skrotzki, J Wosnitza, 1 D Köhler, R Boldt, and M Ruck. Structure-induced coexistence of ferromagnetic and superconducting states of single-phase Bi_3Ni seen via magnetization and resistance measurements. *Physical Review B*, 83(14):140501, 2011.

[47] Xin Shang, Haiwen Liu, and Ke Xia. Andreev spectroscopy of the triplet-superconductor state in the Bi/Ni bilayer system. *Physical Review B*, 101(17):174514, 2020.

[48] GJ Zhao, XX Gong, JC He, JA Gifford, HX Zhou, Y Chen, XF Jin, CL Chien, and TY Chen. Triplet p-wave superconductivity with abm state in epitaxial Bi/Ni bilayers. *arXiv preprint arXiv:1810.10403*, 2018.

[49] Jia-Cheng He and Yan Chen. Evidence of triplet superconductivity in Bi/Ni bilayers: Theoretical analysis of point contact andreev reflection spectroscopy results. *Physical Review B*, 106(22):224508, 2022.

[50] P. W. Anderson and P. Morel. Generalized bardeen-cooper-schrieffer states and aligned orbital angular momentum in the proposed low-temperature phase of liquid he^3. *Phys. Rev. Lett.*, 5:136–138, Aug 1960.

[51] P. W. Anderson and W. F. Brinkman. Anisotropic superfluidity in ^{3}He: A possible interpretation of its stability as a spin-fluctuation effect. *Phys. Rev. Lett.*, 30:1108–1111, May 1973.

[52] Liying Liu, Yutao Xing, ILC Merino, DF Franceschini, IG Solórzano, and E Baggio-Saitovitch. Magnetic properties of superconducting phases NiBi and $NiBi_3$ formed during pulsed laser deposition of Ni−Bi films. *Journal of Magnetism and Magnetic Materials*, 514:167275, 2020.

[53] Liying Liu, Yutao Xing, ILC Merino, MDR Henriques, Mauro Doria, IG Solórzano, and E Baggio-Saitovitch. Spontaneous morphology and phase modification driven by sequence of deposition in superconducting Ni−−Bi bilayers. *Materials Chemistry and Physics*, 260:124112, 2021.

[54] Mauro M Doria, Liying Liu, Yutao Xing, ILC Merino, FJ Litterst, and E Baggio-Saitovitch. Shape resonances and the t_c dependence on film thickness of Bi/Ni systems. *Superconductor Science and Technology*, 35(1):015012, 2021.

[55] Bidyadhar Das, Madhusmita Sahoo, Abhilash Patra, Ashok K Yadav, SN Jha, Prasanjit Samal, Kartik Senapati, and Pratap K Sahoo. Phase evolution in thermally annealed Ni/Bi multilayers studied by x-ray absorption spectroscopy. *Physical Chemistry Chemical Physics*, 24(7):4415–4424, 2022.

[56] Bidyadhar Das, Tapas Ranjan Senapati, Ashok Kumar Yadav, GR Umapathy, Sambhu Nath Jha, Kartik Senapati, and Pratap Kumar Sahoo. Reaction-diffusion-driven stoichiometric gradient in coevaporated superconducting $NiBi_3$ thin films. *Crystal Growth & Design*, 2023.

[57] Patrick LeClair, JS Moodera, John Philip, and D Heiman. Coexistence of ferromagnetism and superconductivity in Ni/Bi bilayers. *Physical review letters*, 94(3):037006, 2005.

[58] Esmeralda Lizet Martinez Piñeiro, Brenda Lizette Ruiz Herrera, Roberto Escudero, and Lauro Bucio. Possible coexistence of superconductivity and magnetism in intermetallic $NiBi_3$. *Solid State Communications*, 151(6):425–429, 2011.

[59] Numan Şarlı and Mustafa Keskin. Coexistence of ferromagnetism and superconductivity in NiBi – binary alloy. *Chinese Journal of Physics*, 60:502–509, 2019.

[60] Peter Fulde and Richard A Ferrell. Superconductivity in a strong spin-exchange field. *Physical Review*, 135(3A):A550, 1964.

[61] AI Larkin and Yu N Ovchinnikov. Nonuniform state of superconductors. *Soviet Physics-JETP*, 20(3):762–762, 1965.

[62] Dai Aoki, Andrew Huxley, Eric Ressouche, Daniel Braithwaite, Jacques Flouquet, Jean-Pascal Brison, Elsa Lhotel, and Carley Paulsen. Coexistence of superconductivity and ferromagnetism in URhGe. *Nature*, 413(6856):613–616, 2001.

[63] Roberto Casalbuoni and Giuseppe Nardulli. Inhomogeneous superconductivity in condensed matter and qcd. *Reviews of Modern Physics*, 76(1):263, 2004.

[64] Vladimir Z Kresin, Yurii N Ovchinnikov, and Stuart A Wolf. Inhomogeneous superconductivity and the "pseudogap" state of novel superconductors. *Physics Reports*, 431(5):231–259, 2006.

[65] Sangmoon Park, Kyongha Kang, Weiqiang Han, and Thomas Vogt. Synthesis and characterization ofBi nanorods and superconducting nibi particles. *Journal of alloys and compounds*, 400(1-2):88–91, 2005.

[66] Teyeb Ould-Ely, John H Thurston, Arvind Kumar, Marc Respaud, Wenhua Guo, Claudia Weidenthaler, and Kenton H Whitmire. Wet-chemistry synthesis of nickel- bismuth bimetallic nanoparticles and nanowires. *Chemistry of materials*, 17(18):4750–4754, 2005.

[67] H Yoshida, T Shima, T Takahashi, T Kaneko, T Suzuki, HM Kimura, K Asami, and A Inoue. Magnetic properties of NiBi. *Journal of magnetism and magnetic materials*, 239(1-3):5–7, 2002.

[68] William D Pyrz, Sangmoon Park, Tom Vogt, and Douglas J Buttrey. Electron beam-induced fragmentation and dispersion of bi- ni nanoparticles. *The Journal of Physical Chemistry C*, 111(29):10824–10828, 2007.

[69] William D Pyrz, Sangmoon Park, Douglas A Blom, Douglas J Buttrey, and Tom Vogt. High-angle annular dark-field scanning transmission electron microscopy investigations of bimetallic nickel bismuth nanomaterials created by electron-beam-induced fragmentation. *The Journal of Physical Chemistry C*, 114(6):2538–2543, 2010.

[70] Matthew Vaughan, Nathan Satchell, Mannan Ali, Christian J Kinane, Gavin BG Stenning, Sean Langridge, and Gavin Burnell. Origin of superconductivity at nickel-bismuth interfaces. *Physical Review Research*, 2(1):013270, 2020.

[71] VI Dybkov and OV Duchenko. Growth kinetics of compound layers at the nickel-bismuth interface. *Journal of alloys and compounds*, 234(2):295–300, 1996.

[72] Ulrich Schwarz, Sophie Tencé, Oleg Janson, Cevriye Koz, Cornelius Krellner, Ulrich Burkhardt, Helge Rosner, Frank Steglich, and Yuri Grin. $CoBi_3$: A binary cobalt–bismuth compound and superconductor. *Angewandte Chemie International Edition*, 52(37):9853–9857, 2013.

[73] Xiao-Ping Wei, You-He Zhou, and Ya-Ling Zhang. First-principles study the electronic and thermodynamic properties for $CoBi_3$ superconductor. *Journal of Superconductivity and Novel Magnetism*, 29:1203–1211, 2016.

[74] Christopher Mtshali, Charles Thethwayo, Carlos Pineda-Vargas, and Muzi Ndwandwe. The effect of deposition rate and thermal annealing on morphology and microstructural evolution of nickel-bismuth thin film. *Thin Solid Films*, 645:312–319, 2018.

[75] Mirtat Bouroushian, Tatjana Kosanovic, et al. Characterization of thin films by low incidence x-ray diffraction. *Cryst. Struct. Theory Appl*, 1(3):35–39, 2012.

[76] Areef Billah. *Investigation of multiferroic and photocatalytic properties of Li doped $BiFeO_3$ nanoparticles prepared by ultrasonication*. PhD thesis, 05 2016.

[77] Pabitra Das. *Optical Properties of Low Dimensional Structures Using Cathodoluminescence in a High Resolution Scanning Electron Microscope*. PhD thesis, 09 2014.

[78] Ray F Egerton et al. *Physical principles of electron microscopy*, volume 56. Springer, 2005.

[79] F Iacopi, PM Vereecken, M Schaekers, M Caymax, Nele Moelans, Bart Blanpain, O Richard, Christophe Detavernier, and H Griffiths. Plasma-enhanced chemical vapour deposition growth of Si nanowires with low melting point metal catalysts: an effective alternative to Au-mediated growth. *Nanotechnology*, 18(50):505307, 2007.

[80] Chuanbo Li, Hiroshi Mizuta, and Shunri Oda. *Growth and characterisation of Ge Nanowires by chemical vapour deposition*. InTech, 2011.

[81] Kristin Persson. Materials data on Bi (sg:166) by materials project, 2 2016. An optional note.

[82] Koichi Momma and Fujio Izumi. Vesta 3 for three-dimensional visualization of crystal, volumetric and morphology data. *Journal of applied crystallography*, 44(6):1272–1276, 2011.

[83] F Aousgi, W Dimassi, B Bessais, and M Kanzari. Effect of substrate temperature on the structural, morphological, and optical properties of Sb_2S_3 thin films. *Applied Surface Science*, 350:19–24, 2015.

[84] K Hiruma, M Yazawa, T Katsuyama, K Ogawa, K Haraguchi, M Koguchi, and H_ Kakibayashi. Growth and optical properties of nanometer-scale gaas and InAs whiskers. *Journal of Applied Physics*, 77(2):447–462, 1995.

[85] A RS Wagner and S WC Ellis. Vapor-liquid-solid mechanism of single crystal growth. *Applied physics letters*, 4(5):89–90, 1964.

[86] Bing Wang, Yuhua Yang, Ningsheng Xu, and Guowei Yang. Mechanisms of size-dependent shape evolution of one-dimensional nanostructure growth. *Physical Review B*, 74(23):235305, 2006.

[87] Venkataramana Bonu, Binaya Kumar Sahu, Arindam Das, Sankarakumar Amirthapandian, Sandip Dhara, and Harish C Barshilia. Sub-wavelength waveguide properties of 1d and surface-functionalized SnO_2 nanostructures of various morphologies. *Beilstein journal of nanotechnology*, 10(1):379–388, 2019.

[88] Yong Su, Xuemei Liang, Sen Li, Yiqing Chen, Qingtao Zhou, Song Yin, Xia Meng, and Mingguang Kong. Self-catalytic vls growth and optical properties of single-crystalline GeO_2 nanowire arrays. *Materials Letters*, 62(6-7):1010–1013, 2008.

[89] JP Boulanger and RR Lapierre. Patterned gold-assisted growth of gap nanowires on si. *Semiconductor Science and Technology*, 27(3):035002, 2012.

[90] H Cui, Y Sun, and CX Wang. Unusual growth direction and controllable wettability of w-catalyzed AlN nanowires. *CrystEngComm*, 15(26):5376–5381, 2013.

[91] Kazuya Hatano, Keita Kobayashi, Takashi Hiraiwa, Takatsugu Yoshida, Hidehiro Yasuda, and Fumio Kokai. Germanium catalyzed vapor–liquid–solid growth and characterization of amorphous silicon oxide nanotubes: comparison to the growth of its nanowires. *SN Applied Sciences*, 1:1–13, 2019.

[92] A JB Hannon, S Kodambaka, FM Ross, and RM Tromp. The influence of the surface migration of gold on the growth of silicon nanowires. *nature*, 440(7080):69–71, 2006.

[93] Hadi Hijazi, Frédéric Leroy, Guillaume Monier, Gabin Grégoire, Evelyne Gil, Agnès Trassoudaine, Vladimir G Dubrovskii, Dominique Castelluci, Nebile Isik Goktas, Ray R LaPierre, et al. Dynamics of gold droplet formation on SiO_2/Si (111) surface. *The Journal of Physical Chemistry C*, 124(22):11946–11951, 2020.

[94] JE Mooij and Yu V Nazarov. Superconducting nanowires as quantum phase-slip junctions. *Nature Physics*, 2(3):169–172, 2006.

[95] Chun Ning Lau, N Markovic, M Bockrath, A Bezryadin, and M Tinkham. Quantum phase slips in superconducting nanowires. *Physical review letters*, 87(21):217003, 2001.

[96] IG Gonzalez-Martinez, A Bachmatiuk, V Bezugly, J Kunstmann, T Gemming, Z Liu, G Cuniberti, and MH Rümmeli. Electron-beam induced synthesis of nanostructures: a review. *Nanoscale*, 8(22):11340–11362, 2016.

[97] RF Egerton, P Li, and M Malac. Radiation damage in the tem and sem. *Micron*, 35(6):399–409, 2004.

[98] V Yu Kolosov, AA Yushkov, and LM Veretennikov. Recrystallization and investigation of bismuth thin films by means of electron beam in transmission electron microscope. In *Journal of Physics: Conference Series*, volume 1115, page 032087. IOP Publishing, 2018.

[99] Jon Dobson. Magnetic nanoparticles for drug delivery. *Drug development research*, 67(1):55–60, 2006.

[100] Asahi Tomitaka, Hamed Arami, Andrea Raymond, Adriana Yndart, Ajeet Kaushik, Rahul Dev Jayant, Yasushi Takemura, Yong Cai, Michal Toborek, and Madhavan Nair. Development of magneto-plasmonic nanoparticles for multimodal image-guided therapy to the brain. *Nanoscale*, 9(2):764–773, 2017.

[101] AE Berkowitz, RH Kodama, Salah A Makhlouf, FT Parker, FE Spada, EJ McNiff Jr, and S Foner. Anomalous properties of magnetic nanoparticles. *Journal of magnetism and magnetic materials*, 196:591–594, 1999.

[102] Steen Mørup, Daniel E Madsen, Cathrine Frandsen, Christian RH Bahl, and Mikkel F Hansen. Experimental and theoretical studies of nanoparticles of antiferromagnetic materials. *Journal of Physics: Condensed Matter*, 19(21):213202, 2007.

[103] Rajwali Khan, Sattam Al Otaibi, Abdulrahman J Babqi, Nasir Rahman, Mohammad Sohail, Rabbim Mixlievich Yusupov, Sherzod Shukhratovich Abdullaev, Alamzeb Khan, Shahid Iqbal, Tommaso Del Rosso, et al. Structural, dielectric, and magnetic responses in doped ZnO magnetic nanoparticles for spintronics. *Journal of Materials Science: Materials in Electronics*, 34(3):169, 2023.

[104] FS Bergeret, AF Volkov, and KB Efetov. Enhancement of the josephson current by an exchange field in superconductor-ferromagnet structures. *Physical review letters*, 86(14):3140, 2001.

[105] FS Bergeret, Anatoly F Volkov, and KB Efetov. Induced ferromagnetism due to superconductivity in superconductor-ferromagnet structures. *Physical Review B*, 69(17):174504, 2004.

[106] A.I. Buzdin. *Reviews of Modern Physics*, 77:935–976, 2005.

[107] F. S. Bergeret, A. F. Volkov, and K. B. Efetov. *Reviews of Modern Physics*, 77:1321–1372, 2005.

[108] Eugene A Demler, GB Arnold, and MR Beasley. Superconducting proximity effects in magnetic metals. *Physical Review B*, 55(22):15174, 1997.

[109] A. I. Buzdin, M. Fauré, and M. Houzet. Superconductor-ferromagnet heterostructures. In Rudolf Gross, Anatolie Sidorenko, and Lenar Tagirov, editors, *Nanoscale Devices - Fundamentals and Applications*, pages 197–224, Dordrecht, 2006. Springer Netherlands.

[110] FS Bergeret, AF Volkov, and KB Efetov. Long-range proximity effects in superconductor-ferromagnet structures. *Physical review letters*, 86(18):4096, 2001.

[111] R. S. Keizer, S. T. B. Goennenwein, T. M. Klapwijk, G. Miao, G. Xiao, and A. Gupta. *Nature*, 439:825–827, 2006.

[112] JS Jiang, D Davidović, Daniel H Reich, and CL Chien. Oscillatory superconducting transition temperature in nb/gd multilayers. *Physical review letters*, 74(2):314, 1995.

[113] S Mironov, AS Mel'nikov, and A Buzdin. Electromagnetic proximity effect in planar superconductor-ferromagnet structures. *Applied Physics Letters*, 113(2):022601, 2018.

[114] Chien-Kang Hsu, Daniel Hsu, Chun-Ming Wu, Chi-Yen Li, Chi-Hang Hung, Chi-Hung Lee, and Wen-Hsien Li. Coexistence of ferromagnetism and superconductivity in Pb/PbO core/shell nanoparticles. *Journal of Applied Physics*, 109(7), 2011.

[115] Xiao-Liang Wang, Mikhail Feygenson, Meigan C Aronson, and Wei-Qiang Han. Sn/SnO_x core- shell nanospheres: synthesis, anode performance in li ion batteries, and superconductivity. *The Journal of Physical Chemistry C*, 114(35):14697–14703, 2010.

[116] Erik J Luber, Brian C Olsen, Colin Ophus, and David Mitlin. Solid-state dewetting mechanisms of ultrathin Ni films revealed by combining in situ time resolved differential reflectometry monitoring and atomic force microscopy. *Physical Review B*, 82(8):085407, 2010.

[117] Puspanjali Sahu and Bhagavatula LV Prasad. Time and temperature effects on the digestive ripening of gold nanoparticles: is there a crossover from digestive ripening to ostwald ripening? *Langmuir*, 30(34):10143–10150, 2014.

[118] P Zhang, F Zuo, FK Urban III, A Khabari, P Griffiths, and A Hosseini-Tehrani. Irreversible magnetization in nickel nanoparticles. *Journal of magnetism and magnetic materials*, 225(3):337–345, 2001.

[119] Jeotikanta Mohapatra and Jia Ping Liu. Rare-earth-free permanent magnets: the past and future. *Handbook of magnetic materials*, 27:1–57, 2018.

[120] Ram Mohan. Green bismuth. *Nature chemistry*, 2(4):336–336, 2010.

[121] SI Popkov, AA Krasikov, AA Dubrovskiy, MN Volochaev, VL Kirillov, ON Martyanov, and DA Balaev. Size effects in the formation of an uncompensated ferromagnetic moment in NiO nanoparticles. *Journal of Applied Physics*, 126(10), 2019.

[122] Xiufang Qin, Caiyun Sui, and Lanxin Di. Influence of substrate temperature on the morphology and structure of bismuth thin films deposited by magnetron sputtering. *Vacuum*, 166:316–322, 2019.

[123] Remi Lazzari, Frederic Leroy, and Gilles Renaud. Grazing-incidence small-angle x-ray scattering from dense packing of islands on surfaces: Development of distorted wave born approximation and correlation between particle sizes and spacing. *Physical Review B*, 76(12):125411, 2007.

[124] Wenjie Huang, Meng Sun, Wen Wen, Junfeng Yang, Zhuoming Xie, Rui Liu, Xianping Wang, Xuebang Wu, Qianfeng Fang, and Changsong Liu. Strain profile in the subsurface of he-ion-irradiated tungsten accessed by s-gixrd. *Crystals*, 12(5):691, 2022.

[125] Yoshihiro Kubozono, Hiroki Mitamura, Xuesong Lee, Xuexia He, Yusuke Yamanari, Yosuke Takahashi, Yuta Suzuki, Yumiko Kaji, Ritsuko Eguchi, Koki Akaike, et al. Metal-intercalated aromatic hydrocarbons: a new class of carbon-based superconductors. *Physical Chemistry Chemical Physics*, 13(37):16476–16493, 2011.

[126] Michael Tinkham. *Introduction to superconductivity*. Courier Corporation, 2004.

[127] N Giordano. Evidence for macroscopic quantum tunneling in one-dimensional superconductors. *Physical review letters*, 61(18):2137, 1988.

[128] Alexey Bezryadin, CN Lau, and M Tinkham. Quantum suppression of superconductivity in ultrathin nanowires. *Nature*, 404(6781):971–974, 2000.

[129] AG Sivakov, AM Glukhov, AN Omelyanchouk, Y Koval, P Müller, and AV Ustinov. Josephson behavior of phase-slip lines in wide superconducting strips. *Physical review letters*, 91(26):267001, 2003.

[130] AK Elmurodov, FM Peeters, DY Vodolazov, Sébastien Michotte, Sébastien Adam, F de Menten de Horne, Luc Piraux, D Lucot, and D Mailly. Phase-slip phenomena in nbn superconducting nanowires with leads. *Physical Review B*, 78(21):214519, 2008.

[131] VM Dmitriev, IV Zolochevskii, TV Salenkova, and EV Khristenko. Critical currents, phase slip centers, and phase slip lines in superconducting films in the absence of external magnetic field. *Low temperature physics*, 31(2):127–136, 2005.

[132] A Andronov, I Gordion, V Kurin, I Nefedov, and I Shereshevsky. Kinematic vortices and phase slip lines in the dynamics of the resistive state of narrow superconductive thin film channels. *Physica C: Superconductivity and its Applications*, 213(1-2):193–199, 1993.

[133] Cécile Delacour, Bernard Pannetier, Jean-Claude Villegier, and Vincent Bouchiat. Quantum and thermal phase slips in superconducting niobium nitride (NbN) ultrathin crystalline nanowire: Application to single photon detection. *Nano letters*, 12(7):3501–3506, 2012.

[134] W. Chen, A.V. Rylyakov, V. Patel, J.E. Lukens, and K.K. Likharev. Rapid single flux quantum t-flip flop operating up to 770 ghz. *IEEE Transactions on Applied Superconductivity*, 9(2):3212–3215, 1999.

[135] Konstantin K Likharev. *Dynamics of Josephson junctions and circuits*. Routledge, 2022.

[136] Robert H Hadfield. Single-photon detectors for optical quantum information applications. *Nature photonics*, 3(12):696–705, 2009.

[137] B Abeles. Effect of charging energy on superconductivity in granular metal films. *Physical Review B*, 15(5):2828, 1977.

[138] BL Altshuler and BZ Spivak. Mesoscopic fluctations in a superconductor–normal metal–superconductor junction. *Zh. Eksp. Teor. Fiz.*, 92(2):607–615, 1987.

[139] VV Ryazanov, VA Oboznov, A Yu Rusanov, AV Veretennikov, Alexandre Avraamovitch Golubov, and J Aarts. Coupling of two superconductors through a ferromagnet: Evidence for a π junction. *Physical review letters*, 86(11):2427, 2001.

[140] BI Ivlev and Nikolai Borisovich Kopnin. Theory of current states in narrow superconducting channels. *Soviet Physics Uspekhi*, 27(3):206, 1984.

[141] N Giordano and ER Schuler. Macroscopic quantum tunneling and related effects in a one-dimensional superconductor. *Physical review letters*, 63(21):2417, 1989.

[142] Amir O Caldeira and Anthony J Leggett. Influence of dissipation on quantum tunneling in macroscopic systems. *Physical Review Letters*, 46(4):211, 1981.

[143] James S Langer and Vinay Ambegaokar. Intrinsic resistive transition in narrow superconducting channels. *Physical Review*, 164(2):498, 1967.

[144] DE McCumber and BI Halperin. Time scale of intrinsic resistive fluctuations in thin superconducting wires. *Physical Review B*, 1(3):1054, 1970.

[145] N Giordano. Superconductivity and dissipation in small-diameter Pb – In wires. *Physical Review B*, 43(1):160, 1991.

[146] N Giordano. Dissipation in a one-dimensional superconductor: Evidence for macroscopic quantum tunneling. *Physical Review B*, 41(10):6350, 1990.

[147] N Giodano. Superconducting fluctuations in one dimension. *Physica B: Condensed Matter*, 203(3-4):460–466, 1994.

[148] Weiwei Zhao, Xin Liu, and Moses Hung-Wai Chan. Quantum phase slips in 6 mm long niobium nanowire. *Nano letters*, 16(2):1173–1178, 2016.

[149] Alexey Bezryadin. Quantum suppression of superconductivity in nanowires. *Journal of Physics: Condensed Matter*, 20(4):043202, 2008.

[150] GR Berdiyorov, MV Milošević, and FM Peeters. Kinematic vortex-antivortex lines in strongly driven superconducting stripes. *Physical Review B*, 79(18):184506, 2009.

[151] G Berdiyorov, K Harrabi, F Oktasendra, K Gasmi, AI Mansour, JP Maneval, and FM Peeters. Dynamics of current-driven phase-slip centers in superconducting strips. *Physical Review B*, 90(5):054506, 2014.

[152] SA Kivelson and BZ Spivak. Aharonov-bohm oscillations with period hc/4e and negative magnetoresistance in dirty superconductors. *Physical Review B*, 45(18):10490, 1992.

[153] P Xiong, AV Herzog, and RC Dynes. Negative magnetoresistance in homogeneous amorphous superconducting Pb wires. *Physical review letters*, 78(5):927, 1997.

[154] Albert Schmid and Gerd Schön. Linearized kinetic equations and relaxation processes of a superconductor near t_c. *Journal of Low Temperature Physics*, 20:207–227, 1975.

[155] D Yu Vodolazov. Negative magnetoresistance and phase slip process in superconducting nanowires. *Physical Review B*, 75(18):184517, 2007.

[156] Kohei Masuda, Satoshi Moriyama, Yoshifumi Morita, Katsuyoshi Komatsu, Tasuku Takagi, Takayuki Hashimoto, Norihisa Miki, Takasumi Tanabe, and Hideyuki Maki. Thermal and quantum phase slips in niobium-nitride nanowires based on suspended carbon nanotubes. *Applied Physics Letters*, 108(22), 05 2016. 222601.

[157] Lior Shani, Philip Tinnefeld, Yafit Fleger, Amos Sharoni, Boris Ya Shapiro, Avner Shaulov, Oleg Gang, and Yosef Yeshurun. Dna origami based superconducting nanowires. *AIP Advances*, 11(1):015130, 2021.

[158] Sreemanta Mitra, Girish C Tewari, Diana Mahalu, and Dan Shahar. Negative magnetoresistance in amorphous indium oxide wires. *Scientific Reports*, 6(1):37687, 2016.

[159] A Rogachev, T-C Wei, D Pekker, AT Bollinger, Paul M Goldbart, and A Bezryadin. Magnetic-field enhancement of superconductivity in ultranarrow wires. *Physical review letters*, 97(13):137001, 2006.

[160] Mingliang Tian, Nitesh Kumar, Shengyong Xu, Jinguo Wang, James S Kurtz, and MHW Chan. Suppression of superconductivity in zinc nanowires by bulk superconductors. *Physical review letters*, 95(7):076802, 2005.

[161] Henry C Fu, Alexander Seidel, John Clarke, and Dung-Hai Lee. Stabilizing superconductivity in nanowires by coupling to dissipative environments. *Physical review letters*, 96(15):157005, 2006.

[162] XH Chen, T Wu, G Wu, RH Liu, H Chen, and DF Fang. Superconductivity at 43 k in $SmFeAsO_{1-x}F_x$. *nature*, 453(7196):761–762, 2008.

[163] Alexandre I Buzdin. Proximity effects in superconductor-ferromagnet heterostructures. *Reviews of modern physics*, 77(3):935, 2005.

[164] JWA Robinson, S Piano, G Burnell, C Bell, and MG Blamire. Zero to π transition in superconductor-ferromagnet-superconductor junctions. *Physical Review B*, 76(9):094522, 2007.

[165] SH Brongersma, E Verweij, NJ Koeman, DG De Groot, R Griessen, and BI Ivlev. Series of maxima in the field dependent magnetic moment of layered superconductors. *Physical review letters*, 71(14):2319, 1993.

[166] C Hünnekes, HG Bohn, W Schilling, and H Schulz. Flux line matching effects in $YBa_2Cu_3O_{7-x}$ thin films. *Physical review letters*, 72(14):2271, 1994.

[167] J-Y Lin, M Gurvitch, SK Tolpygo, A Bourdillon, SY Hou, and Julia M Phillips. Flux pinning in $YaBa_2Cu_3O_{7-\delta}$ thin films with ordered arrays of columnar defects. *Physical Review B*, 54(18):R12717, 1996.

[168] I Swiecicki, C Ulysse, T Wolf, R Bernard, N Bergeal, J Briatico, G Faini, J Lesueur, and Javier E Villegas. Strong field-matching effects in superconducting $YBa_2Cu_3O_{7-\delta}$ films with vortex energy landscapes engineered via masked ion irradiation. *Physical Review B*, 85(22):224502, 2012.

[169] A Gurevich, E Kadyrov, and DC Larbalestier. Dynamic matching of vortex lattice in superconducting multilayers. *Physical review letters*, 77(19):4078, 1996.

[170] U Patel, ZL Xiao, A Gurevich, SEVDA Avci, J Hua, R Divan, U Welp, and WK Kwok. Magnetoresistance oscillations in superconducting granular niobium nitride nanowires. *Physical Review B*, 80(1):012504, 2009.

[171] AV Herzog, P Xiong, and RC Dynes. Magnetoresistance oscillations in granular sn wires near the superconductor-insulator transition. *Physical Review B*, 58(21):14199, 1998.

[172] A Johansson, G Sambandamurthy, Dan Shahar, N Jacobson, and Reshef Tenne. Nanowire acting as a superconducting quantum interference device. *Physical review letters*, 95(11):116805, 2005.

[173] Alexandre Avraamovitch Golubov, M Yu Kupriyanov, and E Il'Ichev. The current-phase relation in josephson junctions. *Reviews of modern physics*, 76(2):411, 2004.

[174] Konstantin K Likharev and Vasilii K Semenov. Rsfq logic/memory family: A new josephson-junction technology for sub-terahertz-clock-frequency digital systems. *IEEE Transactions on Applied Superconductivity*, 1(1):3–28, 1991.

[175] Juergen Niemeyer, JH Hinken, and Richard L Kautz. Microwave-induced constant-voltage steps at one volt from a series array of josephson junctions. *Applied physics letters*, 45(4):478–480, 1984.

[176] Clark A Hamilton. Josephson voltage standards. *Review of scientific instruments*, 71(10):3611–3623, 2000.

[177] Johannes Kohlmann, Ralf Behr, and Torsten Funck. Josephson voltage standards. *Measurement science and Technology*, 14(8):1216, 2003.

[178] Kartik Senapati, Mark G Blamire, and Zoe H Barber. Phase periodic conductance oscillations at subgap andreev resonances in Nb$--$Al$--$AlO$_x$$--Al--$Nb tunnel junctions. *Applied Physics Letters*, 97(16), 2010.

[179] Ronald H Ono, James A Beall, MW Cromar, Todd E Harvey, ME Johansson, Carl D Reintsema, and David A Rudman. High-t$_c$ superconductor-normal metal-superconductor josephson microbridges with high-resistance normal metal links. *Applied physics letters*, 59(9):1126–1128, 1991.

[180] Yonuk Chong, PD Dresselhaus, and SP Benz. Thermal transport in stacked superconductor–normal metal–superconductor josephson junctions. *Applied physics letters*, 83(9):1794–1796, 2003.

[181] James F Ziegler and Jochen P Biersack. The stopping and range of ions in matter. In *Treatise on Heavy-Ion Science: Volume 6: Astrophysics, Chemistry, and Condensed Matter*, pages 93–129. Springer, 1985.

[182] Ambika Bawa, Rajveer Jha, and Sangeeta Sahoo. Tailoring phase slip events through magnetic doping in superconductor-ferromagnet composite films. *Scientific Reports*, 5(1):13459, 2015.

[183] P Seidel, F Schmidl, A Pfuch, H Schneidewind, and E Heinz. Investigations on high-thin film intrinsic stacked josephson junctions. *Superconductor Science and Technology*, 9(4A):A9, 1996.

[184] Tapas Senapati, Ashwin Kumar, and Kartik Senapati. Phase biasing of a josephson junction using rashba-edelstein effect. *arXiv preprint arXiv:2304.11457*, 2023.

[185] OV Duchenko and VI Dybkov. Determination of NiBi$_3$ reaction-diffusion constants in ni-bi couples. *Journal of materials science letters*, 14(24):1725–1727, 1995.

[186] F Leroy, F Cheynis, Y Almadori, S Curiotto, M Trautmann, JC Barbé, Pierre Müller, et al. How to control solid state dewetting: A short review. *Surface Science Reports*, 71(2):391–409, 2016.

[187] R Prozorov, Y Yeshurun, T Prozorov, and A Gedanken. Magnetic irreversibility and relaxation in assembly of ferromagnetic nanoparticles. *Physical Review B*, 59(10):6956, 1999.

[188] Bivas Rana and Anjan Barman. Ultrafast magnetization dynamics of chemically synthesized Ni nanoparticles. *The Journal of Physical Chemistry C*, 119(30):17444–17449, 2015.

[189] Chanho Park, Jae Won Choi, No-Won Park, Gil-Sung Kim, Takashi Kikkawa, Eiji Saitoh, and Sang-Kwon Lee. Role of two-dimensional monolayer MoS_2 interlayer in the temperature-dependent longitudinal spin seebeck effect in Pt/YIG bilayer structures. *Journal of Materials Chemistry A*, 11(22):11831–11839, 2023.